5-2014

Understanding Polymers in Thin Films to Improve Photovoltaic Properties and Surface Bound Polymerization

Lesley Danielle Thompson
University of Tennessee - Knoxville, lthomp29@utk.edu

To the Graduate Council:

I am submitting herewith a dissertation written by Lesley Danielle Thompson entitled "Understanding Polymers in Thin Films to Improve Photovoltaic Properties and Surface Bound Polymerization." I have examined the final electronic copy of this dissertation for form and content and recommend that it be accepted in partial fulfillment of the requirements for the degree of Doctor of Philosophy, with a major in Chemistry.

Mark D. Dadmun, Major Professor

We have read this dissertation and recommend its acceptance:

Frank Vogt, Jimmy Mays, Bin Hu

Accepted for the Council:

Carolyn R. Hodges

Vice Provost and Dean of the Graduate School

(Original signatures are on file with official student records.)

Understanding Polymers in Thin Films to Improve Photovoltaic Properties and Surface Bound Polymerization

A Dissertation Presented for the
Doctor of Philosophy
Degree
The University of Tennessee, Knoxville

Lesley Danielle Thompson
May 2014

Abstract

Organic photovoltaics offer the long-term potential as an economically viable alternative for large-scale power generation. Most organic photovoltaics are based on blends of semiconducting polymers such as poly(3-hexylthiophene-2,5-diyl)(P3HT) with fullerene derivatives such a [6,6]-phenyl-C_{61}-butyric-acid-methyl-ester (PCBM). These bulk heterojunction systems take advantage of phase segregation between P3HT and PCBM to facilitate charge separation and transport. Raman spectroscopy and thermal analysis are used to monitor the ordering and aggregation state of P3HT in P3HT/PCBM thin films as a function of composition and thermal history. Comparison of Raman and X-ray data lead to the conclusion that the "aggregated" species observed in Raman spectroscopy are not crystalline domains as surmised in the literature, but actually correspond to P3HT segments with an intermediate amount of order that are connected to the surface of the P3HT crystal. PCBM is also shown to behave as a plasticizer for the P3HT as it mixes with the amorphous phase, and can dissolve small P3HT crystals. Examination of bilayer systems demonstrates that P3HT domains formed by crystallizing P3HT prior to PCBM deposition creates crystals that are impervious to PCBM. The information supplied from these results provides guidelines to rationally design improved organic photovoltaic active layers.

Further studies were completed to improve the polymerization process of ethyl cyanoacrylate when developing latent fingerprints by the cyanoacrylate fuming method (CFM). During forensic investigations, recovery and identification of latent fingerprints is vital in recreating a crime scene. As a fingerprint ages, however, changes to the chemical nature of the print residue results in a decrease in the quality of the impression obtained using CFM. Attempts to re-hydrate aged prints by exposing prints to water vapor hindered the fuming process, exhibiting a deteriorated print quality after fuming. The water vapor appears to degrade the print, washing away part of the residue. Further experiments demonstrate that fuming at lower temperatures improves the growth of poly(ethyl cyanoacrylate) during the fuming process. An optimum temperature of ~ 10 °C is found, as this temperature balances looser ion pairs and sufficient energy to allow the reaction of monomer to the propagating chain end.

Table of Contents

List of Figures

Chapter 1

The Importance of Understanding Polymers at Surfaces and Interfaces

1.1 Introduction

Polymer thin films are critical in many technological and industrial applications, such as electronic packaging, dielectric coatings, resist layers for lithography, sensor films, adhesion and lubrication.[1] The conflicting goals of reducing film thickness while improving film properties, e.g. uniformity, stability and adhesion to surfaces, require a quantitative insight into the factors that govern the structure and properties of thin films.[2] For this reason, new developments in the field of polymer surfaces, interfaces, and thin films are crucial in the pursuit to rationally develop new materials [1].

A versatile method to rationally design new advanced materials is to combine different substances [3]. Often, at least one of these substances is a polymer. Specific examples are fiber-reinforced polymer composites, stabilization of colloids by thin film polymer layers, or protective coatings in microelectronics [1]. The key idea behind blending a polymer and another material is that the resulting mixture exhibits a combination of the properties of the constituent materials, where the polymer may optimize the physico-chemical properties of the resulting product that are associated with polymers (i.e. transmission of stress or friction, permeability to gases or liquids, chemical resistance against a corrosive environment, etc.), while retaining the properties of the additive. The extent to which this property improvement can be achieved is determined by the mixing characteristics of the

blend, where the interfacial properties are most important in a phase-separated system. Therefore a deeper understanding of this interface is certainly desirable to design and realize specifically tailored materials [4].

While a majority of research and development efforts to date have centered on optimizing bulk properties, recent focus is shifting toward the development of polymer systems with controlled surface and interfacial properties [5]. The surface/interfacial region in a polymer blend is almost invariably different in composition from that of the bulk of the material. Two reasons for this are the enhanced surface chemical reactivity due to accessibility of a surface to reactants and a thermodynamic driving force to minimize interfacial energy [6]. Interfaces are the media through which the different phases in a multicomponent polymer system interact, whether they are the interfaces between the microphases in pure block copolymers [4], between different phases in more complex, often undefined, blends, composites, or nanocomposites, or between sophisticated organizations of molecules in the inter-cellular domain of biological tissues [7].

In this dissertation, it is hoped to attain a better understanding of the interfaces in organic photovoltaic devices and on the surfaces that dominate the superglue fuming of latent fingerprints. In solar cell devices, for example, the interface between the electron acceptor and electron donor are critical in determining the device's efficiency. Similarly, when developing latent fingerprints with superglue fuming, the interface where the print interacts with the vaporized monomer is key to the success of the fuming process.

1.1.2 History and Progress of Solar Cells

Solar energy conversion is a broad and rapidly expanding research field [1]. The increasing global demand for energy, in combination with concerns over the use of fossil fuels, encourages the demand for renewable sources of energy. The umbrella of 'solar energy conversion' encompasses solar thermal, solar fuels, solar-to-electricity (photovoltaic, PV) technology and the great many subcategories below those [3]. This multidisciplinary research area brings together fundamental and applied aspects of material science, synthetic inorganic and organic chemistry, photochemistry, electrochemistry, semiconductor physics and engineering, amongst others [8]. The entry of polymers into energy conversion technologies was first realized in the 1970's by Peter Wright and Michel Armand with the discovery of polymer electrolytes (ionically conducting polymers). This finding introduced the first new class of solid-state ionic conductors since Michael Faraday first identified the phenomenon of solid-state ionic conductivity in the 1800's [9].

In 2009, the average global primary energy consumption reached 14.9 TW. This value is set to increase, according to predictions, doubling by 2050 and tripling by the end of the century[9]. To meet this demand alone, additional sources of fuel will be required if inflated fuel prices and political conflicts are to be prevented, since most of the current demand is met by fossil fuels, which are finite and are located in only a few locations in the world. In addition, pressure is being put on governments to reduce the amount of CO_2 and other greenhouse gases emitted in an effort to prevent climate change. Sunlight is clean, abundant [more energy from sunlight strikes the Earth in 1h (4.3×10^{20} J) than all the energy consumed on the planet[10]]

readily available, secure from a geopolitical standpoint as it is available throughout the globe, and, in use, poses no threat to our environment or to our climate through pollution or greenhouse gases.

Solar cell technologies can be divided into three generations. The first generation is the established crystalline silicon (c-Si) technology. The second generation includes emerging thin-film technologies that have just entered the market, while the third generation covers future technologies, which are on the brink of being commercialized.

The first generation comprises established commercial technologies. Silicon-based systems make up approximately 90% of the current PV market and most are manufactured in Europe and Asia. The raw materials (silicon wafers) are expensive, where shortages have a tremendous impact on price. Additionally, high purity of the silicon is required, therefore over half the cost is that of the silicon wafers. Although silicon is the second most abundant element on the Earth's surface, the high purity and the energy intensive processing that is required translate into a high cost for the silicon feedstock. Fortunately, solar grade silicon is supplied at a reasonable cost because it is a by-product of the high-tech electronics industry [8]. However, the PV industry has now out-grown its role as a by-product of the electronic industry and the demand for silicon is greater than the supply of rejected material from the electronics industry.

Figure 1.1 shows a log-log historical plot of modules. For the period 1979-2005 this plot is a straight line, the slope of which is the experience

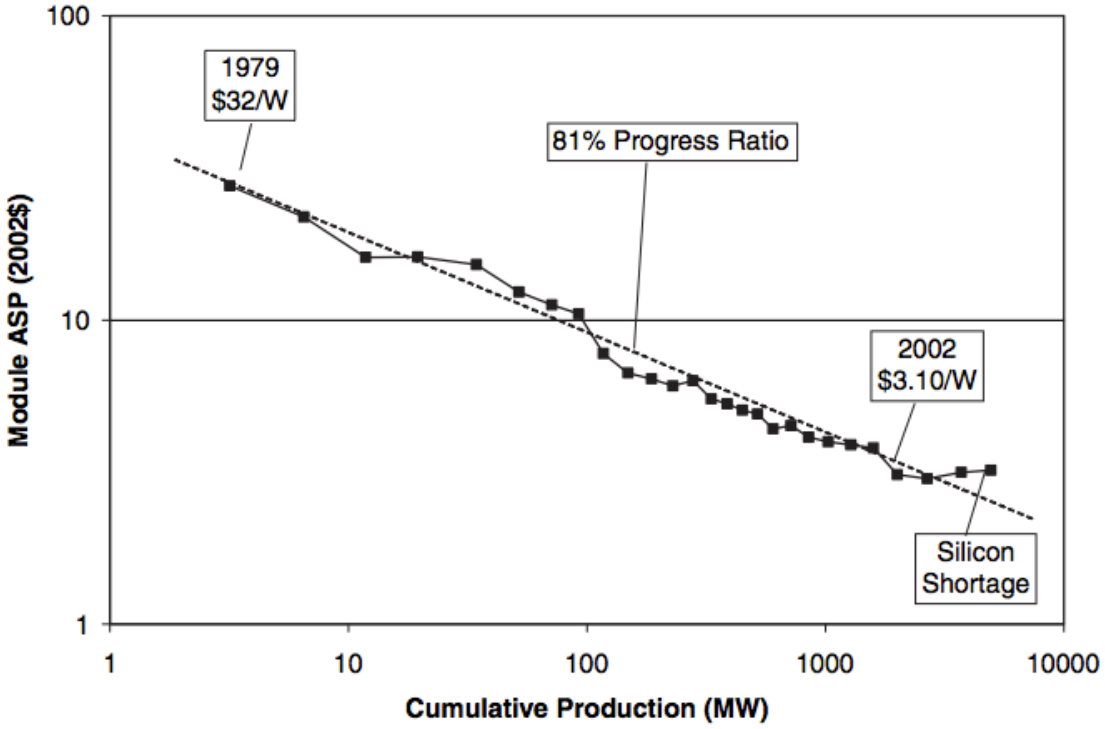

Figure 1.1 Historical plot of module price showing classic experience curve behavior [9].

factor. In the case of PVs the experience factor is 80%, meaning that module prices reduce 20% when doubling of the cumulative volume. A number of forecasts have been made using this learning curve, along with the annual growth rate of the industry, to predict when PV technologies will become competitive with fossil fuels. These forecasts range from optimistic assumptions that the market growth will continue at a rate of 30% a year to less optimistic growth rates of 10-15 % per year. While the exact values vary, the general agreement is that, following the 20% learning curve, module prices will not fall below the \$1 W_p^{-1} threshold until the early 2020s, corresponding to a cumulative production capacity of about 120 GW_p. If solar energy is to fill the 'energy gap' between current and future usage, or indeed replace current nonrenewable fuels, a substantial reduction in cost and vast improvement in efficiency are required much faster than the present experience curve. To change the slope of this trend drastically, and escape the dependency on silicon supply, new technologies that improve the cost-to-efficiency ratio are needed [11].

The second generation of PVs saw the rise of thin-film technologies. Thin-films are becoming a competitive class of PVs, doubling in production from 2006 to 2007. The majority is produced in the USA where investment in alternative thin-film technologies is highest, but China should soon overtake the USA in terms of production capacity. The market share of thin-film technologies increased from only a few percent in 2000, to 16% in 2009, compared with 37% for monocrystalline Si. It is expected that the growth in these alternative technologies should exceed that of c-Si in the coming years. The advantages of thin-film solar cells include the ease of

manufacturing large areas at lower cost, a wider range of applications including straightforward building integration, higher kilowatt hour/kilowatt under Standard Test Conditions (kWh/kW_{STC}) output, higher battery charging current, attractive appearance and a range of possible deposition techniques resulting in the ability to assemble devices using flexible substrates. Materials that are suitable for thin-film PVs must have direct band gaps (high extinction coefficients) and maintain good electronic properties in polycrystalline form (i.e. exhibit a minimum of recombination at grain boundaries). Second generation PVs saw the development of PVs that met these criteria using amorphous silicon (a-Si), cadmium telluride (CdTe), and copper indium (gallium) diselenide (CIGS) as the active layer [4]. In many of these devices, the raw materials are expensive and rare, necessitating the optimization of equipment to reduce waste and requiring additional recycling steps [8].

While it has been demonstrated that thin-film PV modules can be produced at a reasonable cost, a primary limitation of the technology comes from the availability of the materials. While a-Si-based devices are not reliant on the rate of production of the raw materials, CdTe PVs are severely limited by the abundance and rate of mining of Te [4]. Similarly CIGS technology is limited by the rate of production of In, Se, and Ga. The scarcity and toxicity of many of the components means that careful disposal or, more likely, recycling of the materials is required. [4] Since manufacturing costs are so dependent on scale, reductions in the amount of material required, as well as very high efficiencies, are essential for second generation PVs to become cost competitive and meet the energy demand [8].

Despite improvements in efficiency and increase in demand for renewable sources of electricity, solar power currently supplies only 0.1% of the primary energy demand [9]. This can be attributed to the high installation cost of PV systems, 50% of which is the cost of the module. Solar electricity tariffs cost around three to five times that of conventional residential electricity tariffs, yet grid-connected systems are the highest growing applications. [12] To compete with c-Si in this market, the next generation of solar cells must perform close to maximum efficiency over a range of light conditions and temperatures, have good long-term stability and, in order to lower installation costs, need to be durable, flexible and attractive so that they can be applied as building integrated PVs e.g. on flexible steel and architectural glass. [1] To be able to supply electricity to potential markets in the developing world, the installation costs must be lowered considerably. For solar electricity to penetrate the electricity market in the developing world, installed solar system costs need to drop from around $8-10 per Watt to $3 per Watt (corresponding to $0.15 kWh^{-1}) [9]. For these reasons, third generation solar cells are being designed to significantly reduce the manufacturing costs of PV systems (Figure 1.2) [3]. The third generation approaches being developed include dye-sensitized titania solar cells, organic PVs, tandem cells, 'hot electron' utilization and materials that generate multiple electron-hole pairs [3].

1.1.3 Why Are Organic Solar Cells the Next Step?

Organic materials comprise most of the chemically identifiable materials on the earth. Despite this fact, inorganic materials have occupied the traditional role as electronic materials in the modern age. As the density of electronic components

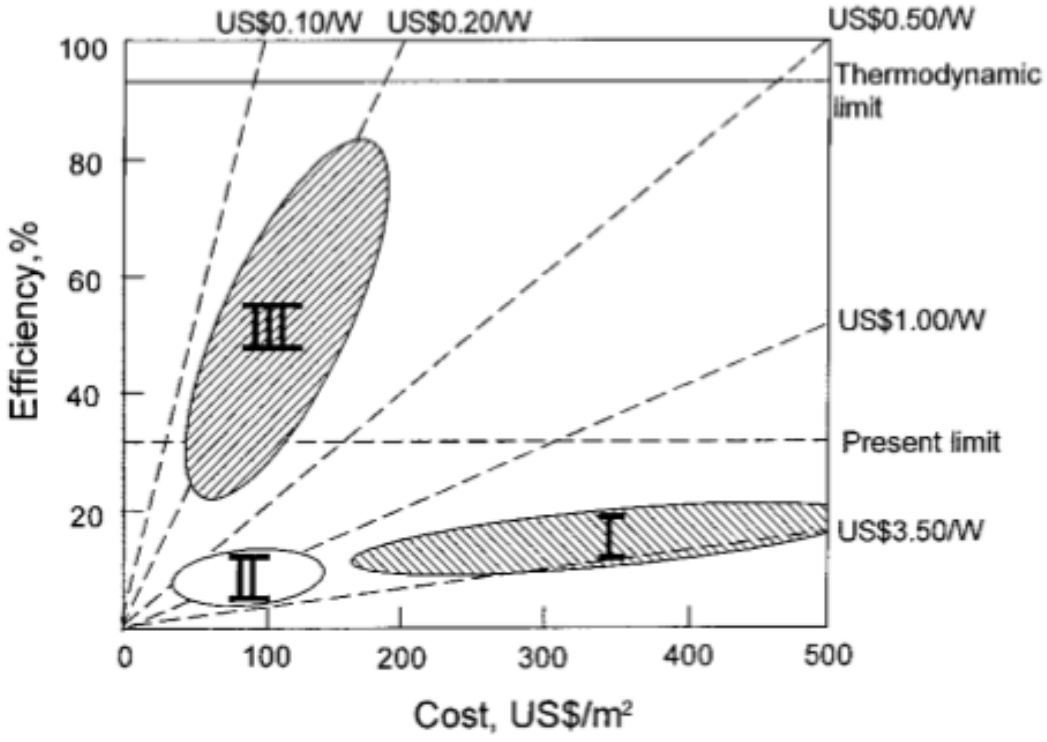

Figure 1.2: Efficiency and cost projections for first, second, and third generation photovoltaic technology [8].

continues to increase, the characteristic size of the individual electronic elements (e.g. transistors) are rapidly approaching the molecular scale, ~10 Å. It is expected, however, that bulk-effect solid-state physic devices will 'mature' at dimensions on the order of 400 atoms (i.e., around 50 to 60 nm), at which point quantum-physics devices and molecular-based elements will come into play. Either individual organic molecules or molecular aggregates become attractive candidates for active elements on these length scales [13].

The interest in organic solar cells has risen strongly in recent years, due to their attractive properties in terms of light trapping and photocurrent generation; combined with the prospect of high throughput and low-cost processing [9]. Many organic semiconductors exhibit very high absorption coefficients, making them promising compounds for PV devices. They differ from silicon solar cells, which are mostly in the single crystal and polycrystalline form, in that organic semiconductors which are of interest for PV applications are usually amorphous or polycrystalline, although single crystals do exist as well [14].

An advantage of allowing a higher degree of disorder is that processing becomes easier and cheaper in terms of cost as well as energy. Organic semiconductors can be thermally evaporated at low temperatures whereas inorganic crystals require higher temperatures, often exceeding 1000 °C. [8] Organic semiconductors can also be processed by printing or coating at room temperature from solution [14]. Although organic materials are limited by lower solar cell efficiencies, their cost structure as well as energy balance can be very favorable. Unfortunately, other properties such as charge transport are more limited; crystals

allow charges to move much more freely, whereas the lack of long-range order in disordered matter leads to charge hopping from one localized state to the next, slowing their transport. Nevertheless, it is understood that the resulting low charge carrier mobility is not a major limiting factor for organic solar cells; other properties are more critical but can often be overcome [8].

The basis for organic solar cells was the observation of dark conductivity in halogen doped organic compounds in 1954, although many of these compounds were not stable [15]. In the following years, systematic research examined the charge transport properties of these small molecules. In the late seventies, the conductivity of the polymer polyacetylene, when doped with halogens, was discovered, for which its three main contributors Shirakawa, Heeger, and MacDiarmid were awarded the Nobel Prize in Chemistry in 2000 [16].

This conductivity in carbon-based semiconductors is due to conjugation in the molecule, the alternation of single and double bonds between the carbon atoms. The ground state of a carbon atom is in the $1s^2 2s^2 2p^2$ configuration. In organic semiconductors, the *s* and *p* orbitals form 3 sp^2 orbitals, the σ bonds. The fourth orbital, p_z, is perpendicular to the plane spanned by the sp^2 orbitals. The overlap of the p_z electron wave functions leads to delocalization of the charges, which is the origin of the conductivity in these organic compounds. Due to Peierls instability, two delocalized energy bands are formed, the bonding and antibonding π and π* orbitals, also called the highest occupied molecular orbital (HOMO) and lowest unoccupied molecular orbital (LUMO), respectively. The HOMO and LUMO are separated by a bandgap typically on the order of one to three electron volts, making

such an organic compound a semiconductor. The transition between these two levels can occur by exciting an electron with light in the visible spectrum. These semiconducting and light absorbing properties make conjugated organics a very interesting choice for PVs.

The first organic solar cells were based on an active layer made of a single material, sandwiched between two electrodes of different work functions [17]. By the absorption of light, strongly bound electron-hole pairs are created, so-call singlet excitons. As their binding energy in organic semiconductors is usually between 0.5 and 1 eV[14], the excitons have to be separated to finally generate a photocurrent. In order to overcome the exciton binding energy, one must either rely on the thermal energy, or dissociate the exciton at a donor-acceptor interface. Unfortunately, both processes have a rather low efficiency: under the operating conditions of solar cells, the temperature is not high enough, and the sample thickness is much thicker than the exciton diffusion length, so that an interface is not found before exciton recombination. The consequence is that many excitons are not dissociated, but photoluminescence occurs as a result of radiative recombination.

The introduction of a second organic semiconductor layer dramatically improved power conversion efficiency, though still produced a relatively low efficiency. The first organic bilayer solar cells were presented by C. W. Tang in the mid eighties [17]. The typical device configuration is shown in Figure 1.3**(**a), where the light is absorbed in the donor material, a hole conducting small molecule such as copper phthalocyanine. In such a bilayer device, the photogenerated singlet excitons

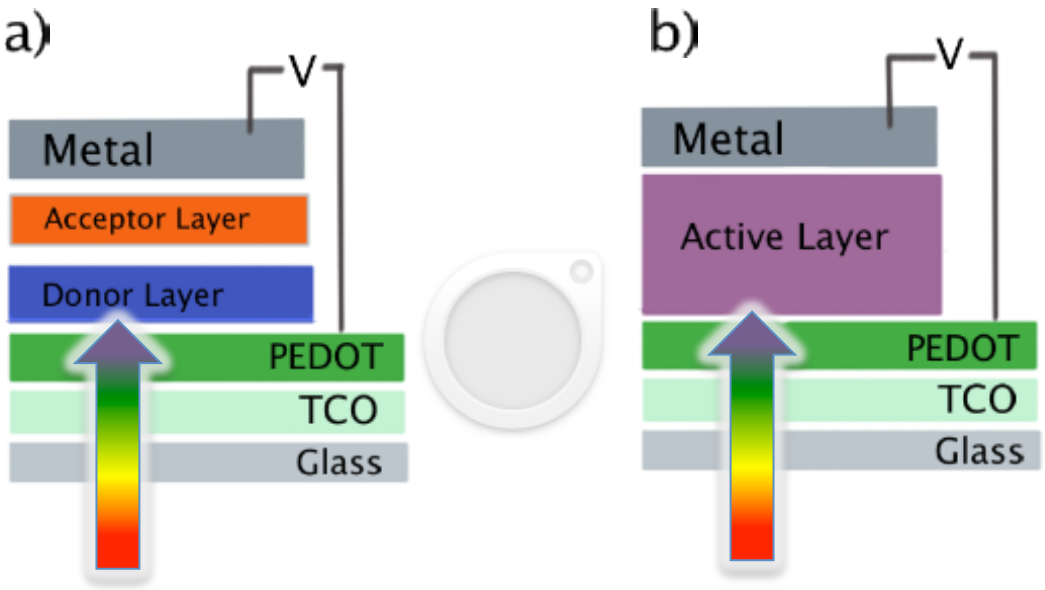

Figure 1.3: Typical device configurations of organic solar cells: (a) bilayer device with planar heterojunction, (b) bulk heterojunction device consisting of a blend of conjugated polymer with a fullerene derivative. On top of the glass substrate, a transparent conductive oxide (TCO) such as indium tin oxide acts as anode, a poly(3,4-ethylendioxythiophen):polystyrolsulfonate (PEDOT) interlayer helps to avoid local shunts. The active layer consists of either the bilayer or the blend of organic semiconductors. On top, a metallic electrode acts as cathode [12].

diffuse within the donor layer towards the planar interface to the second material, the acceptor, which is usually chosen to be strongly electronegative. The acceptor material provides the energy needed for the singlet exciton to be separated [18], as the electron can go to a state of much lower energy within the acceptor. This charge transfer dissociates the exciton, with the electron moving to the acceptor material and the hole remaining in the donor.

The difference between the electron energy in the donor and its energy in the corresponding acceptor level must be larger than the exciton binding energy in order to initiate a charge transfer from donor to acceptor material [9]. If the exciton reaches this donor-acceptor heterojunction by diffusion, it is energetically favorable for the electron to be transferred to the acceptor molecule. This charge transfer, or electron transfer, is reported to be very fast. Indeed, this process has been found to be faster than 100 fs in polymer-fullerene systems, and very efficient, as the alternative loss mechanisms are much slower[17]. Thus, if the exciton can find a donor-acceptor interface before recombination, the exciton is dissociated and the resulting charge carriers are spatially separated.

Even though the electron and the hole now reside on two separate materials, they are still Coulomb bound due to the weak screening of the electric field in organic semiconductors. Therefore, a further step is needed for the dissociation of the final charge pair, for instance a process initiated by an electric field or the energetic disorder of the organic semiconductors. If this is realized, the mutual Coulomb attraction is overcome. Only if this charge carrier separation is successful,

can electrons and holes hop towards their respective electrodes, in order to generate a photocurrent.

The organic bilayer solar cells invented by C. W. Tang were made of two conjugated small molecules, and achieved a power conversion efficiency of about 1% [17]. The limiting factor in this concept is that to fully absorb the incident light, a layer thickness of the absorbing material must be on the order of the absorption length, approximately 100 nm. This is much more than the diffusion length of the excitons, which is about 10 nm in disordered and semicrystalline polymers and small molecules. [18] Therefore, for a 100 nm bilayer active layer, 100% of the incoming photons within the absorption band can be absorbed, but only 10% of these can reach the donor-acceptor interface and be dissociated to charge carrier pairs [17].

In the last thirty years organic solar cells have undergone a gradual evolution that has led to energy conversion efficiencies exceeding 7%. Two main approaches have been explored in the effort to develop viable devices: the donor-acceptor bilayer, commonly achieved by vacuum deposition of molecular components, and the so-called bulk heterojunction (BHJ), which is represented in the ideal case as a bicontinuous composite of donor and acceptor phases, thereby maximizing the all-important interfacial area between the donors and acceptors [9,17-19].

Polymer-based PV systems which can be processed from solution, and which generally take the form of BHJ devices, most closely conform to the ultimate vision of organic solar cells as low-cost, lightweight, and flexible devices. The real advantage of these devices, is the ability to process the composite active layer from

solution in a single step, rather than vacuum deposition, allowing the use of a variety of techniques that range from inkjet printing to spin coating and roll-to-roll casting. However, regardless of the method of preparation, one feature that extends across all classes of organic solar cells is the almost ubiquitous use of fullerenes as the electron-accepting component [19]. The high electron affinity and superior charge transport make fullerenes the best acceptor component currently available for these devices [17].

1.1.4 Harnessing the Interfacial Interactions in Organic Solar Cells

The model system in the field of organic PVs is currently represented by BHJ solar cells based on poly(3-hexylthiophene) (P3HT) and the fullerene derivative [6,6]-phenyl-C_{61}-butyric acid methyl ester (PCBM) [12]. To attain efficiencies approaching 10% in such organic solar cells, much effort is required to understand the fundamental electronic interactions between the polymeric donors and the fullerene acceptors as well as the complex interplay of device architecture, morphology, processing, and the fundamental electronic processes.

Efforts to optimize the performance of organic solar cells rely on understanding their fundamental mechanisms of operation. Scheme 1.1 illustrates the mechanism by which light energy is converted into electrical energy in BHJ devices. It is commonly accepted that the energy conversion process in BHJ devices has four fundamental steps: 1) Absorption of light, which generates excitons, 2) diffusion of the excitons to the donor-acceptor interface, 3) dissociation of the excitons to generate individual charges, and 4) charge transport to and collection at

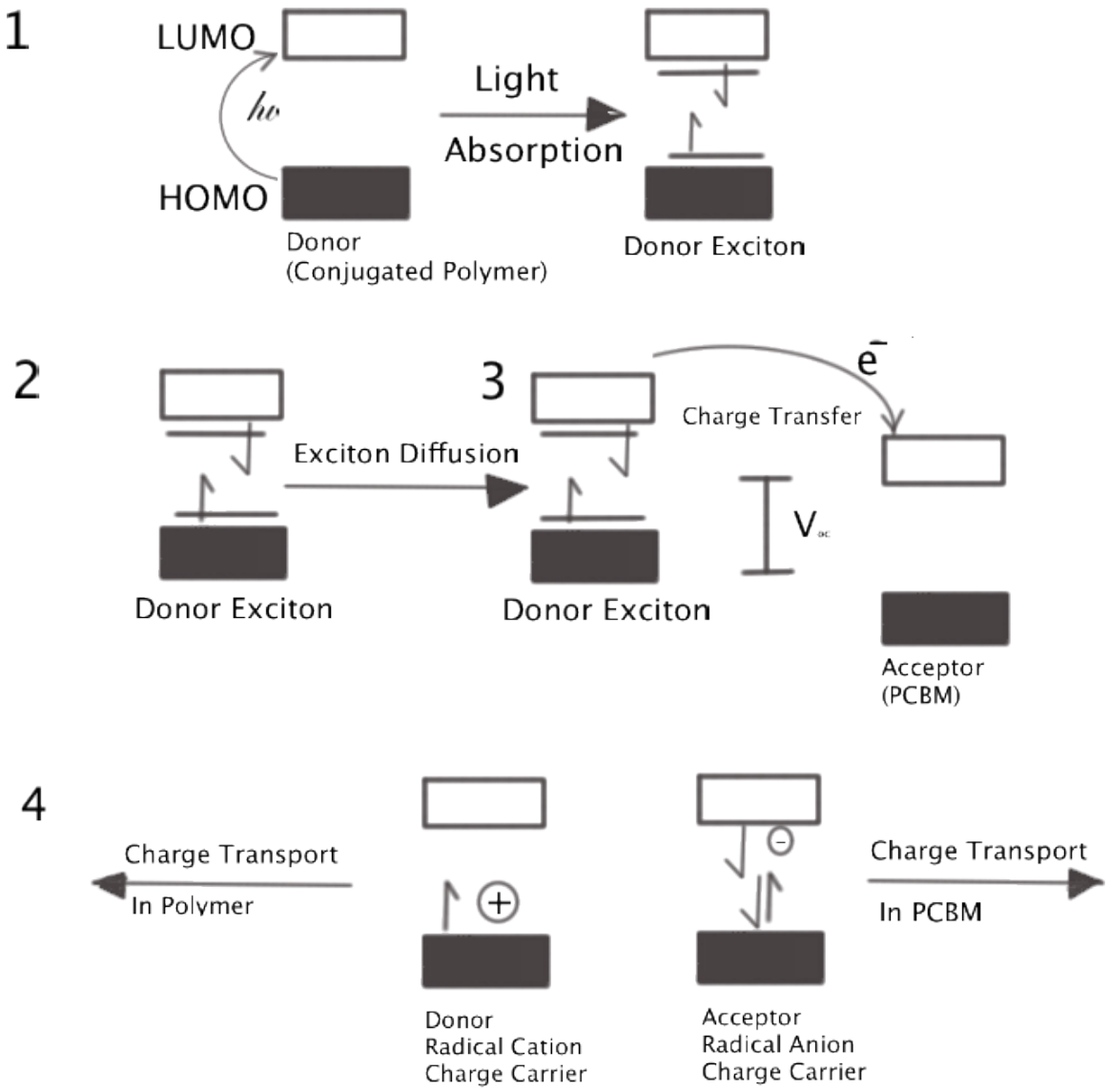

Scheme 1.1: General mechanism for photoenergy conversion in excitonic solar cells.

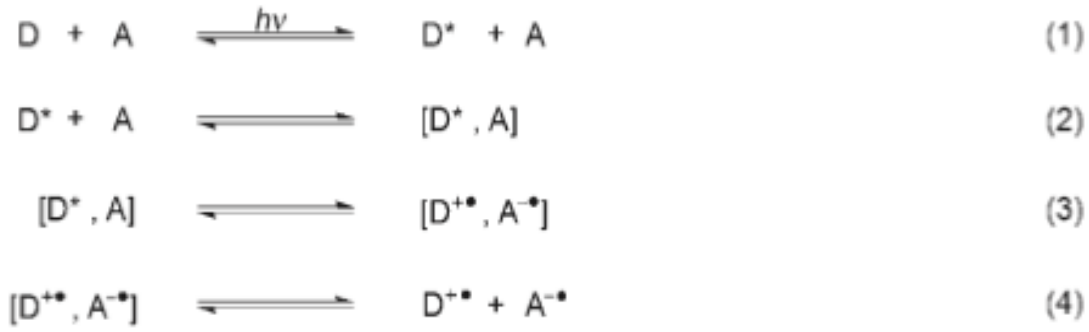

Scheme 1.2: Elementary steps in the process of photoinduced charge separation for a donor (D) and an acceptor (A): 1) Photoexcitation of thedonor;2)diffusion of the exciton and formation of an encounter pair; 3) electron transfer within the encounter pair to form a geminate pair; 4) charge separation.

the electrodes. The elementary steps involved in the pathway from photo-excitation to the generation of free charges are shown in Scheme 1.2. A key point is that electron transfer is not as simple as depicted in Scheme 1. The process must be energetically favorable to form the geminate pair in step 3 of Scheme 1.2 and an energetic driving force must exist to separate this Coulombically bound electron-hole pair.

It is apparent that the active layer donor-acceptor composite interface governs the majority of aspects of the mechanism, with the exception of charge collection, which is based on the electronic interface between the active layer composite and the respective electrode. Besides the fundamental mechanistic steps, the open circuit voltage (V_{oc}) is also governed by the energetic relationship between the donor and the acceptor (Scheme 1.1) rather than the work functions of the cathode and anode, as would be expected from a simplistic view of these diode devices [12]. Specifically, the energy difference between the HOMO of the donor and the LUMO of the acceptor is found to most closely correlate with the V_{oc} of a device [20]. It is therefore apparent that the choice of the components in the active layer, as well as its morphology, governs the physical interaction between the donor and acceptor, and fundamentally affects device performance.

In principle, the optimization of polymer-fullerene solar cells is based on fine-tuning the electronic properties and interactions of the donor and acceptor components so as to absorb the most light, generate the greatest number of free charges, with minimal concomitant loss of energy, and transport the charges to the respective electrodes at a maximum rate and with a minimum of recombination [19].

Such an approach, which focuses solely on the electronic characteristics of the individual components (absorption coefficient, charge carrier mobility, etc.), ignores morphological issues, which are also of critical importance in these devices. However, it is necessary to initially consider the ideal electronic characteristics of each component to optimize the design of the next generation, high-efficiency PV systems.

The two components required to optimize these devices are a soluble fullerene (generally a C_{60} derivative such as PCBM) acceptor and a polymeric donor that can be processed in solution. Fullerenes are currently considered to be the ideal acceptors for organic solar cells for several reasons. First, they have an energetically deeply-lying LUMO, which endows the molecule with very high electron affinity relative to the numerous potential organic donors [19]. The triply degenerate LUMO of C_{60} also allows the molecule to be reversibly reduced, thus illustrating its ability to stabilize negative charges [21]. Importantly, a number of conjugated polymer-fullerene blends are known to exhibit ultrafast photo-induced charge transfer[17]. Furthermore, C_{60} has been shown to have a very high electron mobility of up to 1 $cm^2V^{-1}s^{-1}$ in field-effect transistors (FETs) [9]. It is these fundamental properties, coupled with the ability of soluble fullerene derivatives to pack effectively in crystalline structures conducive to charge transport, that have made fullerenes the most important acceptor materials for BHJ solar cells [19].

In Figures 1.4 (i) and (ii), the processes of exciton diffusion to the exciton dissociating donor-acceptor interface and the subsequent charge transfer of the

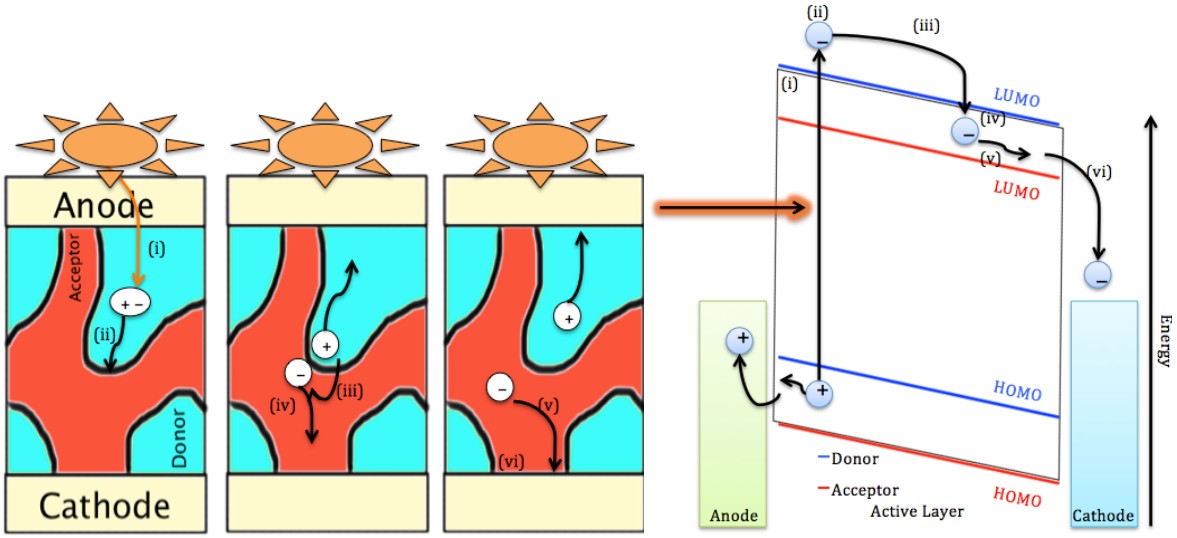

Figure 1.4: From light absorption to photocurrent in a bulk heterojunction solar cell. Left: from a kinetic point of view, right: simplified energy diagram (binding energies for excitons and polaron pairs are not shown). (i) singlet exciton generation from an absorbed photon in the donor material. (ii) exciton diffusion to the acceptor interface. (iii) exciton dissociation by electron transfer to the electronegative acceptor molecules. (iv) separation of the still Coulomb bound electron–hole pair due to electric field and material disorder. (v) charge transport of electron resp. hole by hopping between localized states. At this state, nongeminate recombination between independently generated electrons and holes can occur. (vi) extraction of the charges: photocurrent.

electron from donor to acceptor material are depicted. Indeed, before singlet exciton dissociation at the donor-acceptor interface can take place, the neutral exciton must diffuse to this interface. In bilayer solar cells, the small exciton diffusion length limits the thickness of the absorbing donor layer. Excitons that are generated farther than the ~10 nm exciton diffusion length to the acceptor are lost by recombination. Consequently, the dimensions of the donor layer must ideally be chosen accordingly. The BHJ concept featuring a distributed donor-acceptor interface over the whole active layer puts this guideline into practice. In principle, to accommodate the distance requirements of exciton dissociation, the phase separation in a BHJ should be as small as possible. However, the subsequent steps of electron-hole pair dissociation and charge transport to the electrodes in the solar cell both require phase separations as coarse as possible. The optimum dimensions are therefore a trade-off between these two opposing requirements. Thus, for a given material, the best achievable phase separation for an organic solar cell will usually exploit the full exciton diffusion length, thus losing no excitons to radiative recombination, in the hope that the resulting charge separation and transport properties will be sufficient to extract charges [17].

Even if the donor and acceptor have an ideal electronic relationship, the performance of BHJ solar cells still depends on the physical interaction of the donor and acceptor components, which is manifested in the composite morphology. The ideal BHJ solar cell is often defined as a bicontinuous composite of donor and acceptor with a maximum interfacial area for exciton dissociation and a mean domain size commensurate with the exciton diffusion length (5-10nm). According to

this model, the two components should phase segregate on a suitable length scale to allow maximum ordering within each phase and thus allow effective charge transport in continuous pathways to the electrodes so as to minimize the recombination of free charges. The composite should also be formed from solution and self-assemble into the most favorable morphology with the minimal application of external treatments, as well as having long term stability. Such requirements necessitate that the proper balance between the mixing and demixing of the two components can be achieved.

The morphology of the active layer depends on the interplay between a number of intrinsic and extrinsic variables. The intrinsic properties are those that are inherent to the polymer and the fullerene, as well as the fundamental interaction parameters between the two components. These include the crystallinity of the two materials as well as their relative miscibility. The extrinsic factors include all the external influences associated with device fabrication, such as solvent choice, overall concentration of the blend components, deposition technique (spin coating, ink-jet printing, roller casting, etc.), solvent evaporation rate, as well as thermal and/or solvent annealing. It is clear that the number of factors affecting morphology of the active layer is immense and specific to the polymer-fullerene pair used [19].

Poly(3-alkyl) thiophenes (P3ATs) are particularly suitable for OPV cells and organic transistors due to their substantial hole mobilities. The highest mobilities occur in films cast from regio-regular P3ATS, which sustain greater long-range order relative to their regio-random counterparts [9]. Long-range order in the form of two-dimensional lamellar structures, results in the prevalence of crystal-like

domains and/or aggregates, where the role of the interpolymer interactions, such as interchain coupling, in electronic and photophysical properties dominates [22]. Inter-chain interactions impact charge delocalization and transport as well as neutral excitation transport through the formation of delocalized excitons. [20,23]

The structure and properties of these crystals and aggregates can be revealed by the use of Raman spectroscopy [24]. Information about morphology in conjugated polymers has often been derived by methods such as absorption or Raman spectroscopy, which have shown to be sensitive to changes in their local order or conformational properties [25]. Because Raman bands are excited on resonance with π-π* transitions; only Franck-Condon active vibrational modes are selectively visualized. This feature makes spectra quite simple, and the relative intensities of Raman bands are highly sensitive to local fluctuations in composition and morphology that can be exploited to study these parameters in conjugated polymers. [26] This work can be expanded to also monitor the effect of a second component, such as fullerenes, on these parameters.

The morphology that results from blending conjugated polymers and fullerenes are critical for device performance, therefore, significant research effort has focused on studying the phase separation mechanism and optimum morphological conditions to permit efficient splitting of excitons into charge carriers and charge transport. Methods to control the delicate balance between forming an interpenetrating network and excessive phase segregation, that can cause charge carrier traps, is needed.

In order to be able to develop methods to direct the morphology of conjugated polymers and fullerenes to create more efficient OPV performance, the affect of PCBM on the order of P3HT domains must also be understood more thoroughly. This problem will be addressed by studying samples in which the organization of the PCBM and P3HT are independently controlled, with the goal of elucidating the impact of the ordering of each component on the OPV performance, as well as the interdependence of the presence of one component on the ordering of the other.

Figure 1.5 demonstrates the rational control of the sample preparation conditions and monitoring of the impact the method of introduction of PCBM into the sample has on P3HT ordering. First neat P3HT thin films will be investigated to establish a primary understanding of the ordering of the pure polymer. Using this information, PCBM will be introduced into the system via mixed thin films or bilayer thin films, in an effort to determine the effect of the presence of PCBM molecules on the morphology and ordering of the P3HT molecules.

OPV materials and devices are not the only technology where polymeric interfaces dominate the performance. Superglue fuming of latent fingerprints is an important technology where the interactions between initiators in the print interface and the monomer vapor is critical to the development of the print. The role of the interface interaction is not fully understood, thus further research is needed.

1.1.5 Forensic Investigation of Developed Fingerprints

In many forensic investigations, the recovery and identification of latent fingerprints are vital in recreating a crime scene. A latent fingerprint is considered

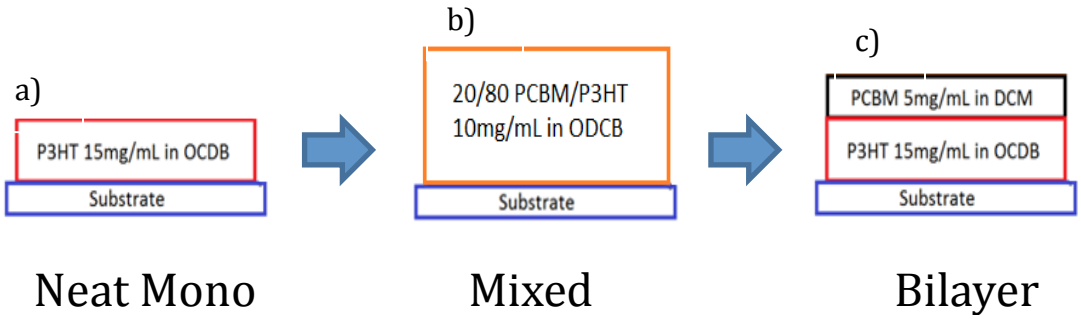

Figure 1.5 To understand the role of PCBM on P3HT in a PCBM/P3HT active layer different conditions were studied. a) a P3HT mono layer, b) a PCBM/P3HT miscible mixed layer, and c) a PCBM rich and P3HT rich layer (bilayer) formation.

the transparent residue, deposited from a fingertip onto a substrate, leaving an image of the unique identifiable pattern of an individual's fingerprint ridges [27]. Latent fingerprints are often invisible and must be enhanced in some way before they can be visually detected [28] Numerous methods have been developed to visualize fingerprints; some of the most common are vacuum metal deposition (VMD), powder method, and cyanoacrylate (superglue) fuming method (CFM) [29]. Each technique comes with its advantages and disadvantages, but CFM is one of the more versatile techniques.

1.1.6 Vacuum Metal Deposition

Vacuum metal deposition has been used since the late 1970's in operational forensic science labs to develop latent prints on non-porous surfaces [30]. This process involves the evaporation and deposition of gold and then zinc onto the print surface under a vacuum, where the gold layer is deposited across the whole surface, including where the prints are present followed by the zinc layer depositing only on the fingerprint residue. It is believed that, where the latent print residue is present, the gold is buried within the residue and the zinc cannot bind to these areas. Therefore, VMD development usually results in transparent print ridges covered with metallic zinc, known as "normal development" [31]. Because this method is not nearly as straight forward as other methods such as CFM, there are several resultant types of development besides the ideal "normal development". In the case where zinc deposits on to the print ridges and not the valleys or background you can get a "reverse development" [32]. If zinc deposits onto the general background but not the print ridges or valleys, while the print area is well defined, no print detail can be

seen thus producing an “empty development”. Lastly an “over development” can be seen when zinc deposits onto the print ridges as well as the background, destroying any print detail.

The first stage of VMD where the gold layer is deposited is critical in determining the type of development observed [29]. The gold layer tends to be thin and discontinuous causing the gold atoms to form into clusters, as the bonding between gold atoms is stronger than that between gold and the substrate. The thickness and structure of the gold film (size, shape, or density of gold clusters) is thought to determine the binding of zinc to the surface and so the type of development observed [31]. Difficulties are often encountered with VMD, leading to inconsistent and unpredictable developments, resulting in the loss of valuable fingerprint evidence [33].

1.1.7 Powder Method of Development

A second commonly used method is the powder method, which involves the application of finely divided material and the subsequent removal of the excess powder by brushing, blowing, or tapping. This has been the universal method of intensifying fingerprints on non-absorbent surfaces since the early days of fingerprint technology [34]. This technique relies on the mechanical adherence of fingerprint powder to the moisture and oily components of the skin ridge deposits. As the age of the fingerprint residue increase, the moisture and oily components tend to evaporate, especially in warmer climates. Thus aged prints in tropical climates are relatively difficult to develop by the powder technique [35]. One major disadvantage of the powder technique is that the powder is applied with a light-

brushing action, which can cause smudging of the imprint. It is estimated that about 10% of latent fingerprints developed at crime scenes using conventional powder dusting procedures are difficult to identify [36]. Even potentially more disadvantageous is the fact that powders are totally inadequate to develop latent prints on fired cartridge cases. Ridges and valleys are indistinguishable, because of the mechanism that is responsible for powder attachment [37].

1.1.8 Cyanoacrylate Fuming Method

Fortunately, CFM is a versatile and effective development technique on virtually all nonporous surfaces, including glass, metal, coated papers, and all forms of plastics. This method is particularly effective on rough surfaces where physical contact with a fingerprint brush tends to develop the texture of the material along with the latent fingerprints. Superglue vapors are extremely sensitive to fingerprint residue, adaptable to many different crime scene and laboratory situations, and are relatively inexpensive to employ [38].

Investigators are sometimes confronted with evidence of fingerprints in combination with biological material [39]. Unlike other methods, polymerized cyanoacrylate fixes all other biological traces on the carrier that could be of interest for subsequent genetic analysis. Cyanoacrylate treated samples have also shown the simultaneous fixation and increase in visibility of saliva stains that can often be hard to detect [40]. DNA profiles have been extracted from fumed fingerprints on sheets of paper in fraud or blackmail cases or even from epithelial cells left from excessively pressured fingerprints applied during strangulation [41].

The cyanoacrylate polymerization that occurs during the development of latent prints is best explained as a three-stage process to produce polymer growth, thus enabling latent print visualization. The first stage occurs when fumes of cyanoacrylate ester monomers are introduced to the latent fingerprint and quickly interact with initiators in the residue. In the second stage, the monomer bound to this initiator on the fingerprint residue reacts with another cyanoacrylate monomer in the vapor phase to form a dimer on the print. This reacts with yet another monomer, and another, eventually forming a polymer, a long chain of cyanoacrylate molecules. The final process is when the polymer chain reaction is terminated, as seen in Scheme 1.3 [38]. As a latent fingerprint ages, however, changes to the chemical nature of the print residue results in a decrease in the quality of the impression obtained using CFM. The nature of this change in the fingerprint residue and how it affects the polymerization of ethylcyanoacrylate (ECA) is not well understood. The residue that is deposited by an individual leaving a fingerprint is composed primarily of sweat, which is secreted through pores in the hand [42]. The composition of the sweat that is deposited when the ridges of the skin make contact with a surface is a complex mixture. Recent studies have identified hundreds of compounds present in human sweat [36,40,43].

A considerable number of studies to determine the composition of sweat have been performed by both the dermatology and forensic science communities [44]. In particular, a number of studies have investigated how the chemical composition of these residues changes with time, which is a critical problem for the fingerprint examiner and the examination of print development methods[42]. Although

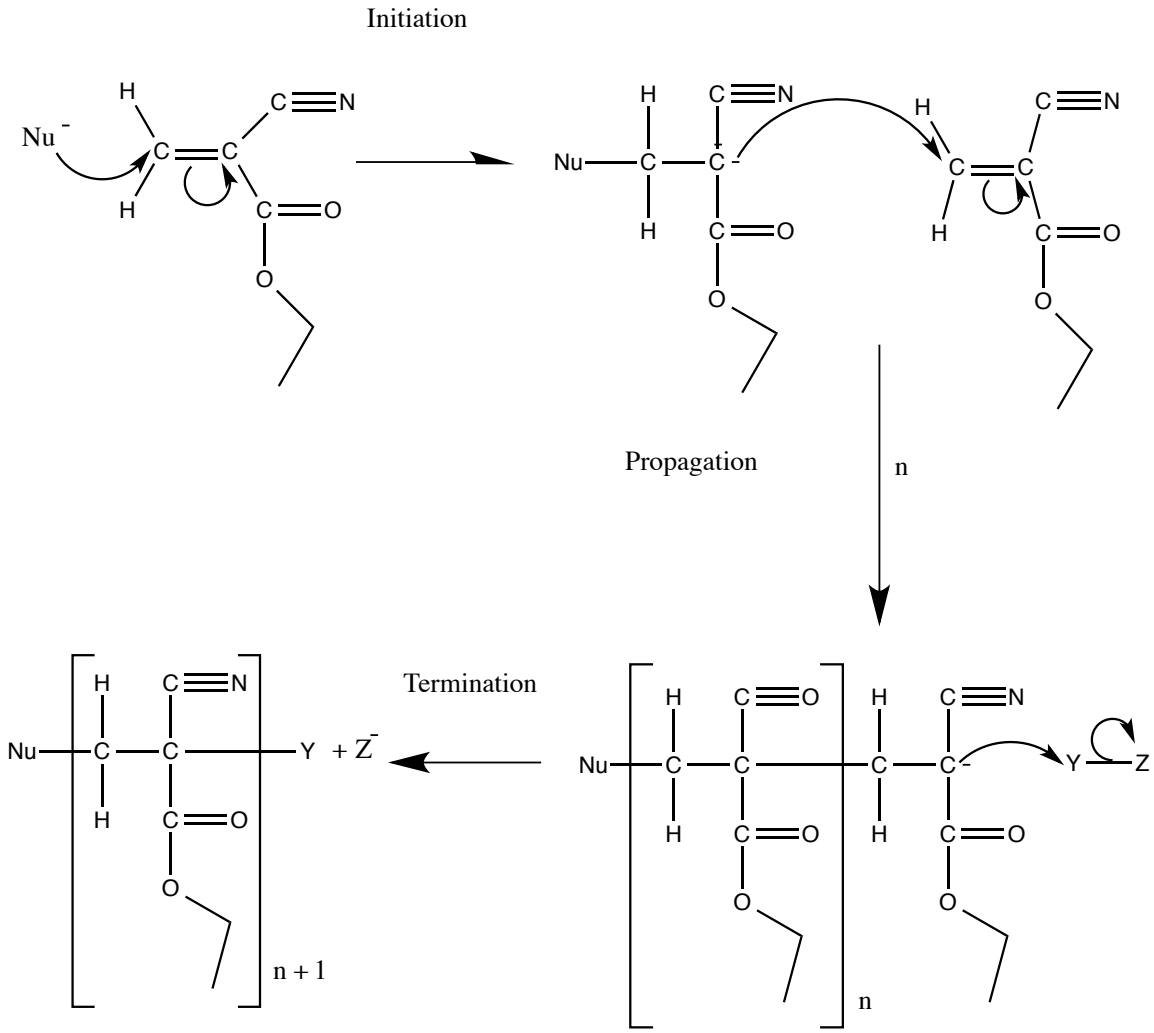

Scheme 1.3: Anionic polymerization mechanism of ethyl-2-cyanoacrylate.

knowledge of the composition of sweat produced in the various glands throughout the body is of interest and provides a baseline for comparison purposes, this information does not usually accurately represent what is actually present in the deposited print at a crime scene.

Three primary glands contribute to the production of sweat. These are the sudoriferous glands (eccrine and apocrine) and the sebaceous glands. Each gland contributes a unique mixture of chemical compounds to the sweat. These compounds either exude from pores onto the friction ridges or are transferred to the friction ridges through touching an area of the body (e.g., the forehead, underarm, etc.). The eccrine gland is one of two types of sudoriferous (or "sweat") glands present in the body [30]. Several million of these glands are distributed throughout the body, most commonly on the palms of the hands and soles of the feet and less numerous on the neck and back. A latent print is a mixture of some or all of the secretions from the three types of glands.

The amount of material contained in a latent print deposit is rather small, typically less than 10μg, and has an average thickness of about 0.1μm. The latent print secretion is a complex emulsification of these numerous and varying compounds. When deposited on a surface, nearly 99% of the print is composed of water [38]. As this water begins to evaporate rapidly from the deposit, the print begins to dry out [30]. This process begins to alter the ability of each process to visualize the print. Fingerprint powder, for example, will not work as well on a dried-out or aged latent print [38].

As a latent fingerprint ages, changes to the chemical composition of the print residue results in a decrease in the quality of the impression obtained using CFM. The nature of this change in the fingerprint residue and how it affects the polymerization of ECA is not well understood. Since the residue that is deposited by an individual on a fingerprint is comprised primarily of eccrine sweat, further examination of this mixture and its affect on the polymerization of ECA is needed. As shown in Table 1.1 [45], eccrine sweat comprises a water-based mixture containing a variety of salts but consists predominantly of NaCl, sodium lactate, urea, and amino acids. The volatile components of the fingerprint residue, primarily water, are known to evaporate out of the fingerprint residue during the aging process. However, it is unclear exactly how the loss of water from the print residue affects its ability to polymerize ECA vapor. Experiments in lab have shown that simple re-hydration of aged prints with water vapor has been unsuccessful in regenerating prints. However, the previously reported eccrine based salts are nonvolatile and should remain during the aging process [42]**.** Do these eccrine based salts play a role in the initiation of the polymerization of ECA? And can they be re-constituted to aid in the polymerization of the ethyl cyanoacrylate in aged prints?

While ECA does polymerize anionically, its unique chemical structure makes the synthesis of poly(ethyl cyanoacrylate) unlike conventional anionic polymerizations. The chemical environment created by the presence of both the cyano and the acrylate group adjacent to the vinyl group allows for the formation of a very stable anion when attacked by a Lewis base. Thus, almost any Lewis base will

Table 1.1. The solute composition of eccrine sweat, the sweat secreted from the palms of an individual's hands [28].

Components of Eccrine Sweat	Abundance (wt%)
NaCl	43.835
Lactic Acid	29.22%
Urea	11.69%
Amino Acids	7.79%
Others	4.97%
NaH_2PO_4	1.75%
Glucose	0.44%
K_2PO_4	0.31%

initiate the anionic polymerization of the cyanoacrylates. In fact, even water has been shown to initiate the solution polymerization of ECA. One of the few anions that are not capable of initiating polymerization is the chloride ion [42]. Thus, NaCl can be removed from the list of suspected initiators.

A recent study by our group confirmed that two of the most abundant components of eccrine sweat, the lactate ion and amino acids, have the ability to initiate the polymerization process [45]. The data suggests that the carboxylic and amine functionalities can initiate the polymerization of ECA. The study also reported that the process could be either enhanced or suppressed by changing the pH of the initiators. Perhaps most importantly, the study also showed initiation by water alone does not produce polymer with molecular weight consistent with that found from developed fingerprints [45].

Can controlling other parameters, such as the temperature at which the polymerization occurs, increase the amount of polymer and thus the quality of the developed print? It is well known that the stability of the propagating anion plays a large role in the ability to achieve high yields in anionic polymerization. This is especially true in the case of acrylates due to the ease with which the hydrogen atoms adjacent to the ester groups can be pulled off by the propagating anion [45], resulting in side reactions and branched polymers. These side reactions and branched products result in early termination, causing lower yields and molecular weights. Lowering the temperature of the reaction will result in a more stable propagating anion, which improves the efficiency of the polymerization of the monomer, thus producing higher yield and molecular weight [46].

1.2 Conclusion

In this thesis, the results of a research program will be discussed to provide insight into the influence of surfaces and interfaces on the structural development of important thin film systems and provide fundamental information that can be used to rationally improve the performance of these systems.

First, establishing an understanding of how the morphology of P3HT in OPV thin films can be tuned using various fabrication processes will be examined, paying particular attention to the role of miscible PCBM on the development of the ordering and morphology of the P3HT of OPV thin films. The role of PCBM in the morphological development of the P3HT/PCBM thin film for several samples fabrication pathways is monitored by multiple experimental techniques (photoluminescence, Raman spectroscopy, GIXRD, neutron reflectivity, and NEXAFS) that allow for the elucidation of changes in morphology and structure on the nanoscale, in hopes of providing pathways towards developing efficient OPV devices.

Lastly, the focus is transitioned from the role of interfaces in energy conversion to the importance of interfaces in latent fingerprint development. In this work, the polymerization processes that occur during the superglue fuming of latent fingerprint development is examined, focusing on developing information and protocols that may help lab technicians to speed up the superglue fuming process and improve the quality of the latent fingerprint in these development processes. Since there is currently minimal understanding of the polymerization process, this dissertation will investigate methods to improve this process, such as surface

rehydration or control of surface temperature during polymerization. The growth of the polymer during the superglue fuming will be monitored by mass balance and quartz crystal microbalance (QCM). Gel permeation chromatography (GPC) tracks the molecular weight of the polymer chains that are grown off of the print. Mass balance and FT-IR provide information that can be interpreted to understand a possible "hardening" effect with time and to follow the reactions that occur during the fuming process. The goal of this dissertation is to achieve an understanding of the polymerization process of superglue during the fuming process at the fingerprint surface and the resultant quality of print by studying various fuming conditions that should affect the rate of polymerization, such as colder temperature and water vapor exposure.

Chapter 2

Experimental Procedures

2.1 Assembly of Organic Solar Cells and Active Layers

Initial photoluminescence and Raman spectroscopy experiments were completed on samples that contained [6,6]-Phenyl C_{61} butyric acid methyl ester (PCBM) and Poly(3-hexyl thiophene) (P3HT) that was received from Sigma-Aldrich with a regioregularity ≥ 90%, molecular weight of 20-30k, and a PDI of 1.5, as reported by the manufacturer. The solvents, ortho-dichlorobenzene (ODCB) and dichloromethane (DCM) were purchased from Sigma-Aldrich and used as received. To fabricate the mixed thin films, PCBM and P3HT were co-dissolved in ODCB at a concentration of 10mg/mL. The initial samples were prepared on glass cover slides. However, after starting the project the resulting effect of the slightest impurities in P3HT on the packing ability of the layer were realized, therefore P3HT was then switched to a better quality from Rieke Metals and PCBM from Nano-C. The Rieke Metal P3HT had a regioregularity ≥ 95%, a molecular weight of 20-30k, and a PDI = 2.0. Also after realizing a more detailed analysis would be needed, the substrate was switched to Silicon (Si) wafers and the samples of most importance were re-tested.

Prior to casting, the solutions were allowed to dissolve for approximately 12 hours, then heated to 55 °C for several hours before spin coating in order to achieve complete dispersion. The samples were spin coated at 1000rpm for 90 seconds for the mixed thin films, the P3HT monolayer, and the P3HT layer of the bilayer thin films. In the fabrication of the bilayer thin films, after the initial coating of the P3HT

onto Si wafer, the layer was allowed to dry for at least 20 minutes in a N_2 atmosphere.

The fabrication process of the bilayers allowed for PCBM and P3HT to be dissolved separately in DCM and ODCB, respectively, which allowed separate casting of the layers. Therefore in some samples, the initial P3HT layers were allowed to crystallize at 150 °C in a vacuum oven at times ranging from 0 minutes to 60 minutes. After this annealing procedure, the solution of PCBM in DCM was spun on top of the P3HT layer at 4000 rpm for 10 seconds. Samples were then analyzed by Raman spectroscopy and GIXRD and labeled as the as-cast (AC) samples. The same samples were then annealed for 15 minutes at 150 °C in a vacuum oven and re-analyzed. The samples where both layers were exposed to heat simultaneously are referred to as the annealed (AN) bilayer samples.

The bilayer samples that were analyzed by Raman, GIXRD, and NEXAFS were fabricated on smaller (2.5 x 2.5 cm) thin wafers. The concentrations of P3HT in ODCB and PCBM in DCM were varied to control the thickness of each layer and therefore the ratio of P3HT/PCBM. The correlation of the solution concentration to final film thickness for the initial spin rate was obtained from literature and used to guide the precise conditions for film fabrication [47], as shown in Table 2.1.

For neutron reflectivity experiments, larger 2-inch wafers were used. These samples required a slower spin rate of 400 rpm for 4 minutes for P3HT and 1000 rpm for 20 seconds for PCBM to maintain the targeted thicknesses and consistency of the layers. To maintain the ratios of P3HT/PCBM, a calibration chart (Table 2.1) was developed to allow for the prediction of the film thickness from solution

Table 2.1 Concentrations of solutions and spin rates used to acquire the desired thickness ratios for bilayer samples.

P3HT in ODCB				PCBM in DCM			
1000 rpm (90 sec)		400 rpm (4 mins)		4000 rpm (10 sec)		1000 rpm (20 sec)	
10 mg/mL	50 nm	4 mg/ml	34 nm	5 mg/mL	22 nm	5 mg/mL	17 nm
15 mg/mL	80 nm	8 mg/mL	52 nm	10 mg/mL	34 nm	8 mg/mL	25 nm
20 mg/mL	115 nm	12 mg/mL	81 nm			12 mg/mL	43 nm
22.5 mg/mL	125 nm					15 mg/mL	57 nm
25 mg/mL	140 nm						
27.5 mg/mL	155 nm						

concentration for these spin speeds.

2.2 Photoluminescence

Absorbance and photoluminescence (PL) spectra were obtained from thin films on glass cover slides and solutions in a quartz cell (Starna). The absorbance spectra were obtained using a Varian Cary 5000 spectrophotometer operating between 200 and 1800 nm. Photoluminescence of the samples was measured with a Fluorolog-3 FL3-222 (JY Horiba), using excitation wavelengths between 250 and 450 nm.

2.3 Raman Spectroscopy

The Raman experiments were completed with a Ti:sapphire laser (Spectra-Physics, Tsunami) that is pumped with a 532 nm Nd:YAG laser (Spectra-Physics, Millenium XV). The wavelength range of the Ti:sapphire is 690 – 1050 nm that generates a 5 ps pulse (as measured with an autocorrelator at 940nm) at a rate of 81 MHz. The laser was tuned to a wavelength of 942.5 nm, as measured by a NIR/VIS spectrometer (Ocean Optics, USB4000). The output of the laser is 1.2 Watts that is polarized using a Glan polarizer (Thorlabs). The vertical polarization of the laser is sent to a frequency doubler (Spectra-Physics), which produces the wavelength (471.25 nm) that is used as the excitation source. Before entering the microscope, the light passes through a beam expander, which allows for tighter focusing of the beam by the objective. In the inverted microscope (Nikon, Ti-U), an 80/20 beamsplitter (Semrock) reflects the excitation beam through an objective (Nikon, 20x, NA=0.5), which is focused on the sample. The objective collects the

back-scattered light, transmitting it through the beamsplitter, and then to either the eyepiece or a spectrometer (Acton, Princeton Instruments) with a back-lit CCD LN-cooled detector (Princeton Instruments, PIXIS 100). The Raman spectrum of liquid cyclohexane was used to calibrate the spectrometer. Rastering of the sample stage allowed for an average sample spectrum to be taken.

Error for the analysis of Raman peaks was calculated from the error of each peak fit using Equations 2.1-2.5, where A_{peak} is the area measured from the Lorentzian fit and e_{peak} is the error associated with each peak. All error calculations were ~10^{-4} and thus smaller than the symbols in the figures.

$$\frac{A_{Peak\ 1}}{A_{peak\ 1} + A_{peak\ 2}} \times 100 = \%\ Agg \tag{2.1}$$

$$e_{new} = \sqrt{e_{peak\ 1}^2 + e_{peak\ 2}^2} \tag{2.2}$$

$$\frac{e_{peak\ 1}}{Peak\ 1} x\ 100\% = \%e_{peak1} \tag{2.3}$$

$$\%e_{new} = \frac{e_{new}}{A_{peak\ 1} + A_{peak\ 2}} \tag{2.4}$$

$$\%e_{Final} = \sqrt{\left(\%e_{peak1}\right)^2 + (\%e_{new})^2} \tag{2.5}$$

2.4 Grazing Incidence x-ray Diffraction

X-ray diffraction from thin films was completed with a Phillips X'pert-Pro diffractometer in grazing-incidence geometry. The angle of incidence between the X-ray and the thin film surface (Ω) was 0.3° for all samples. All spectra were normalized to high q, as the intensity of the spectra in this regime is proportional to the amount of sample, but is not dependent on the specific structure. The size of the

$$CrystalSize = \frac{0.9\lambda}{\beta \cos\theta} \qquad (2.6)$$

polymer crystallites were calculated using Scherrer's equation (Equation 2.6) [48,49], where the full width half maximum, β, and the scattering angle, θ, of the crystalline peak were extracted from the resultant diffraction pattern, and λ is the wavelength of the X-ray, 1.54 Å. The area under the crystalline peak is also used to characterize the amount of crystalline P3HT in each sample. To maintain consistent analysis of this peak area from sample to sample, Igor was used to integrate the (100) peak. In this fitting process, the same integration range was used for all samples and multiple fit integration ranges were tested to verify that there is no influence of the integration window on the observed trends. Also, during the Gaussian fitting, a linear baseline was applied to the peak in order to minimize the influence of intensity of the overall spectra on the area of the peak

2.5 Neutron Reflectivity

The Liquids Reflectometer available at the Spallation Neutron Source on Oak Ridge National Laboratory's campus was used for all reflectivity measurements. Sample measurements were collected for the q-range of 0.006–0.105 $Å^{-1}$ with a

neutron wavelength varying from 2.75–5.75 Å.

Layers and Motofit software were used to fit the reflectivity profiles and model scattering length density profiles in order to determine the distribution of components in the thin films.

Assuming Fickian diffusion, the time needed for a PCBM molecule to diffuse across the thickness of the film can be readily estimated. Using literature values for the diffusion coefficient of PCBM (2.5×10^{-14} m^2 s^{-1} at 140 °C) [50], the PCBM molecule will traverse a 1600 Å film (the thickest film studied) in less than a second. Thus, all samples measured had adequate time to readily reach equilibrium [51].

Unfortunately, it is not possible to directly extract structural information of the scattering sample from the measured reflectivity. To circumvent this limitation, the reflectivity of a model scattering length density (SLD) depth profile is calculated and compared to the experimentally measured reflectivity. The reflectivity of the model depth profile is iteratively refined until the calculated and experimental reflectivity profiles match. With foreknowledge of the sample scattering characteristics and suitable constraints imposed to maintain a physically realistic system, the fitting provides a result that accurately reflects the scattering structure of the sample. One constraint used in the fitting of these data includes a mass balance of the P3HT and PCBM in the sample. The depth profile of the spin-cast bilayers and subsequently annealed bilayers was modeled using 2–5 layers.

The SLD, thickness, and roughness of each layer were freely varied. A model

is assumed to accurately reflect the structure of the sample when the model reflectivity profile converges with the experimental profile, where the quality of fit is gauged using χ^2 statistics described by Equation 2.7, and the mass balance of the model system is within 5% of the mass balance of the sample.

$$\chi = \sum R_{(q)calc} - R_{(q)exp}/R^2_{(q)exp} \quad (2.7)$$

In Equation 2.7, R(q)calc and R(q)exp are the calculated and experimental reflectivities. The SLD profile is then analyzed to obtain the concentration depth profile of each component in the system.

$$\Phi_{(z)PCBM} = \frac{SLD_{(z)} - SLD_{(P3HT)}}{SLD_{(PCBM)} - SLD_{(P3HT)}} \quad (2.8)$$

For instance, the PCBM concentration depth profile is determined using Equation 2.8, where $\phi(z)_{PCBM}$ is the volume fraction of PCBM at depth z, $SLD_{(z)}$ is the experimental scattering length density at depth z, and SLD_{P3HT} and SLD_{PCBM} are the SLD of P3HT and PCBM, respectively. In order to quantitatively analyze the reflectivity curves, the accurate scattering length density (SLD) of each component is needed. The density of crystalline P3HT is taken as 1.12 g cm^{-3}, based on X-ray diffraction data [52] and the density of amorphous P3HT is estimated to be ~10% less than that of crystalline P3HT, 1.01 g cm^{-3}. Using these values, the scattering length densities of crystalline P3HT and amorphous P3HT are calculated to be 0.69 x 10^{-6} $Å^{-2}$ ($SLD_{P3HT,c}$) and 0.62 x 10^{-6} $Å^{-2}$ ($SLD_{P3HT,a}$) respectively. Since the exact amount of crystallinity isn't known in our samples, we can estimate the SLD of P3HT from

previous work in our lab. This recent work in our lab suggests that 20% crystallinity is a reasonable value, and thus a SLD of 0.64 x 10^{-6} Å $^{-2}$ is used for the P3HT phase in these bilayer samples. Given the proximity of $SLD_{P3HT,c}$ and $SLD_{P3HT,a}$, any error in this assumption will not significantly impact the results presented below. The density of crystalline PCBM is reported to be 1.67 g cm^{-3} for crystals formed from ODCB [53]. Following the assumption that amorphous PCBM is 10% less dense than crystalline PCBM, the SLD of amorphous PCBM is calculated from its density and composition to be 4.4 x 10^{-6} Å $^{-2}$ [54] which agrees with previous work and our fitting of the neutron reflectivity profile of a spin-cast PCBM monolayer [55].

2.6 Near Edge X-ray Absorption Fine-Structure Spectroscopy

Near edge X-ray absorption fine-structure spectroscopy (NEXAFS) was used to monitor the molecular orientation and surface composition of the polymer:fullerene mixture. Experiments were completed on beamline U7A at the National Synchrotron Light Source (NSLS) at Brookhaven National Laboratory in collaboration with Ronald A. Quinlan, Ph.D. research scientist at Naval Surface Warfare Center, Carderock Division. The partial electron yield (PEY) signal was collected using a channeltron electron multiplier with an adjustable entrance grid bias (EGB). A negative bias of 50 V was applied to prevent low-energy photoelectrons from reaching the detector. The different angles were collected by rotating the sample holder with respect to the incident beam in the plane of incidence. The angle reported is the angle of the incident beam with respect to the

substrate surface. The monochromator energy scale was calibrated using the C K-edge π* transition of graphite, located at 285.5 eV.

2.7 Cyanoacrylate Fuming

2.7.2 Fuming from Sodium Lactate solution

Materials: The chemicals l-sodium lactate (Fluka), ethyl-cyanoacrylate (Sirchie), sulfuric acid (Fischer), 30% hydrogen peroxide (Fischer), hydrochloric acid (Fischer), ACS grade tetrahydrofuran (THF) (Fischer), and ACS grade toluene (Fischer) were used as received. Nanopure water was obtained using a Milli-Pore water treatment system. The pH of each solution was controlled with 4, 7, and 10 pH buffer solutions (Fischer) along with a pH meter (Eutech Instruments) and electrode (Accumet) to measure the pH of each lactate solutions. Silicon wafers obtained from Wafer World were used as the substrates.

A 10mM sodium lactate solution was made by adding 0.0544g of sodium lactate to 100mL of nanopure water in a 100mL volumetric flask. The target pH of the 10mM sodium lactate solution was 4.73. The initial pH of the 10mM sodium lactate solution was taken using a pH meter and subsequent drops of either 1M HCl or 1M NaOH were added to obtain the desired pH of 4.73 for the 10mM sodium lactate solution. Solutions were then stored in a refrigerator until needed. The pH was altered for two reasons; to provide a method to control and adjust the mechanism by which ions are introduced into the systems, and because the pH has a direct effect on the electronic structure of the initiators. In the lactate system, the variation in pH dictates the counter ion at the carboxylate group, either a sodium or

hydrogen atom. In an alanine system, the carboxylate group is altered in much the same way as in the lactate system; however, pH adjustment also impacts the protonation of the amine as well as the zwitterionic nature of amino acids. Amino acids display zwitterionic behavior around their isoelectric point [56]. Secondly, the pH was altered to mimic the environment in the body [56].

Silicon wafers were cut into 1 inch by 1 inch pieces and cleaned via submersion into "piranha" solution for one hour. The piranha solution consisted of a three to one mixture of sulfuric acid to 30% hydrogen peroxide. After an hour, the wafers were taken out of the piranha solution and washed with nanopure water and dried under a stream of dry N_2 gas. The cleaned wafers were stored under vacuum until needed.

Sodium lactate droplets (3-6 drops ~50μL) were deposited onto a Si wafer via an autopipet. The silicon wafer was held in place during the fuming process by a 3-arm clamp attached to a ring stand at a distance of 2 inches above a hotplate containing an aluminum-weighing pan with approximately 2g of ethyl cyanoacrylate monomer. Once white fumes appeared, the Si wafer containing the droplets of initiator was turned upside down so that the Si wafer and droplets were in direct contact with the cyanoacrylate monomer vapors. A cardboard box was placed over the entire set up as a way to concentrate the fumes onto the initiator droplets. Droplets were then fumed for varying times of 30, 60, 90, 120, and 150 seconds.

2.7.3 Examination of Crosslinking Studies of Poly(Ethyl-Cyanoacrylate)

Materials used in these studies were ethyl-cyanoacrylate (Sirchie), standard microscope slides (Fischer), and ACS grade tetrahydrofuran (Fischer).

Clean glass slides were weighed on a Mettler Toledo MS105 Semi-micro balance with 0.015 mg repeatability. Four prints were applied to the slide via our standard fingerprint deposition method. Our standard fingerprint method is used in order to ensure the deposition of the most reproducible fingerprints; hands are washed rigorously for 5 min, followed by thorough rinsing. While air-drying at ambient conditions for 10 min, the hands are kept out of contact with any objects to avoid exposure to any chemical components that are not contained in the natural occurring eccrine sweat prints. Fingerprints are then placed on glass slides and reweighed to obtain the mass of the fingerprints [46]. A hotplate was heated to 150 °C and placed next to a three arm clamp, which holds the microscope slide 2 inches above the hotplate. An aluminum-weighing pan containing approximately 2g of ethyl-cyanoacrylate monomer was placed on the hotplate. Once white monomer vapors were visibly rising from the pan, the microscope slide was placed in the clamp, fingerprint side down, directly exposing the prints to the monomer vapors. The setup was then enclosed via a cardboard box and allowed to fume for 10 minutes. After fuming, the slides were then weighed again to obtain the mass of polymer on the print. Prints were then allowed to dry for varying time intervals ranging from 2-24 hours. During drying, the slides were covered from the top to prevent contamination but vented from the sides to allow for interaction with atmospheric conditions in the lab. After achieving the desired drying time, samples were then soaked in THF for 30 minutes to remove the “uncrosslinked” polymer from the print ridges. After soaking, the samples were allowed to dry and the mass of the remaining “crosslinked” polymer was measured.

2.7.4 Quartz Crystal Microbalance

Research quartz crystal microbalance from Maxtek, Inc was used to log real time changes in the mass of polymer during the cyanoacrylate fuming process. This balance has a mass resolution of <0.4ng/cm^2. Prints where laid on crystals using the standard fingerprint deposition method. The QCM crystal was then placed in the probe and clamped face down 3 inches above a hotplate containing an aluminum pan of approximately 2g of cyanoacrylate. Once fumes were visible from the pan, the sample was covered in the cardboard box and monitored for changes in mass as the print was exposed to cyanoacrylate fumes for ten minutes. QCM crystal were purchased from Maxtek, 5 MHz Ti/Au polished crystals.

2.7.5 Variant Temperature Exposure During the Fuming Process

The temperature at which the interaction between the fingerprint and monomer vapor occurs is controlled. A cooling block was used to control the surface temperature of the slide on which the latent prints were applied. The temperature of the block was maintained by flowing antifreeze through a Brinkman MGW Lauda RM6 intercooler. A temperature probe monitored the temperature of the block throughout the entire fuming process. Prints were then fumed with the standard procedure for ten minutes and then analyzed for mass and molecular weight changes via mass balance and size exclusion chromatography (SEC). SEC measurements were taken on a Polymer Labs GPC 20 equipped with two plgel 5 μm mixed C columns and a WellChrom K-2301 RI detector. HPLC-grade Toluene was used as the flow rate marker, and THF was used as the solvent in all SEC runs, which were calibrated using polystyrene standards. SEC solutions were made by

sonicating the fumed prints in THF for 15 minutes, and then concentrating the solution down in a Fisher brand 4 dram vial. This solution was then filtered with a PTFE 0.45 μm syringe filter and injected into the GPC using a gas-tight 2.5 mL Hamilton syringe. For sonication, a Branson 1510 40 KHz sonicator was used.

2.7.6 Water Vapor Exposure prior to the Fuming Process

Prints applied to glass slides and QCM crystals were exposed to water vapor for ten minutes and then fumed with cyanoacrylate. Boiling water and room temperature water were examined by clamping the fingerprints 3 inches above the beaker of water to allow exposure without getting the sample wet. QCM crystals were monitored for changes in mass in real time during fuming after water exposure. The latent prints on glass slides were analyzed for mass changes by a mass balance, while the molecular weight of the resultant polymer was determined by SEC. Prints were applied as clean prints using the standard fingerprint deposition method and then as oily prints by touching one's forehead immediately prior to print deposition.

2.7.7 Infrared Spectroscopy of Poly(Cyanoacrylate) Curing

For initial studies, a quartz apparatus was made by our glass shop, consisting of a Teflon cuvette confined between two quartz slides. Ethyl cyanoacrylate monomer was placed in the cuvette and an IR spectrum was taken every two hours for a 24 hour time period. Absorbance spectra were collected on a Varian 4100 FT-IR Excalibur Series instrument from wavenumbers 400-8000 at 128 scans with a

resolution of 0.5 cm^{-1}. A background of the empty quartz crystal apparatus was accounted for in the analysis.

For in-situ FT-IR, a Bruker Equinox 55 FTIR spectrometer equipped with an Axiom Analytical Diamond ATR probe (DMD-270) was used. FT-IR-ATR spectra were collected using a Nicolet Nexus spectrometer equipped with a Nicolet Smart Endurance single bounce diamond ATR accessory. Each spectrum consisted of 64 co-added scans obtained over the 4000 cm^{-1} to 525 cm^{-1} region at a resolution of 4 cm^{-1}. The spectra were collected every 5 seconds for extended times, up to ten hours. The polymerization of the neat cyanoacrylate monomer was monitored by dipping the probe tip into a cyanoacrylate monomer, allowing the monomer to polymerize on the probe. To monitor the reaction of the cyanoacrylate from the fumed cyanoacrylate vapor by the print, a clean latent print was applied to the diamond tip of the probe via the standard print deposition method. The print was then exposed to cyanoacrylate fumes for ten minutes using the fuming technique described above. After ten minutes of fuming, the hot plate was turned off and the further reactions that occurred in the print were monitored for up to ten hours. A background of the cyanoacrylate monomer vapor was subtracted out to insure the reaction being monitored was of the fingerprint and cyanoacrylate.

Chapter 3

Establishing a Fundamental Understanding of the Ordering of Neat P3HT and P3HT/PCBM Mixed Active Layer

3.1 Introduction

The ordering of molecules in semiconducting polymeric materials can have significant effects on their optoelectronic properties. For example, thin films of regio-regular P3HT (RR-P3HT) exhibits a high degree of molecular order (π- π stacking of the molecules) relative to the ordering in regio-random P3HT (RRa-P3HT) [26]. This increased molecular order can lead to an increase in absorption at longer wavelengths and a dramatic increase in charge carrier mobility as compared to its more disordered RRa-P3HT thin films or OPV devices [26,57].

3.1.2 Photoluminescence

The fate of an exciton that is formed by the absorption of a photon on a conjugated polymer must be known in order to optimize the performance of an OPV active layer. Photoluminescence (PL) is a photoemission that is the result of the recombination of an exciton, and thus denotes an event that is detrimental to OPV performance. Conversely, PL emission is quenched if the exciton dissociates, a desirable process in the performance of an OPV cell.

Therefore, PL is often used as an indicator of how efficiently excitons dissociate in an OPV cell, i.e. how well excitons can diffuse to a donor-acceptor interface where they can be split into free charges. Changes in the PL spectra can therefore be correlated to a change in the relative extent of exciton recombination

and dissociation. Exciton dissociation occurs when excitons on the polymer chain can reach the donor-acceptor interface before recombining[58]. Therefore, PL is a useful tool to monitor the final product of the exciton in P3HT/PCBM active layers. For instance, higher PL intensity could be the result of emission from different phases (amorphous and crystalline) of the P3HT molecules. In the case of crystalline P3HT, the polymer chains in the lamellae are aligned and closer to each other, so that contact points between any two adjacent chains are more extended. The extended contact points of the polymer chains in the lamellae lead to a more mobile exciton [59]. This also means that the exciton will be less mobile in a sample with more amorphous P3HT, which will lead to more recombination and higher PL intensity. Less PL "quenching" could also be a result of a decrease in mixing of the acceptor and donor molecules, resulting in more recombination of the excitons and therefore increase in the photoluminescence spectra.

Through the use of PL, this research seeks to determine the relative importance of exciton recombination and dissociation in the performance of OPV active layers fabricated by various methods, with the goal of quantitatively correlating the alteration of the order and mixing in these systems to the exciton dissociation or recombination, providing fundamental insight into the ability of these P3HT/PCBM thin films to perform as an OPV device.

3.1.3 Raman Spectroscopy

Raman spectroscopy provides insight into the local ordering of P3HT, and thus how varying processing conditions, which alters the order, mixing, and/or

miscibility of the P3HT and PCBM, modifies the molecular order of the P3HT in the P3HT/PCBM samples. Raman allows us to only monitor the orientation of the P3HT, since the excitation of PCBM occurs at very different wavelengths.

Raman spectroscopy is a simple, non-destructive, technique that monitors the vibrational modes of molecules. This technique, coupled with various theoretical principles, provides important insight into the conformational changes and interactions that occur in these OPV active layers.

Studies of semi-conducting polymeric materials with Raman spectroscopy are usually performed in non-resonant conditions (i.e., molecules are excited by an incident energy lower than their optical band gaps) to avoid direct electronic excitation, which can produce a strong fluorescence background and may overpower weak Raman signals [58]. Raman spectroscopy on resonant conditions (i.e., when Raman excitation wavelength is close to the absorption maximum of molecules), on the other hand, has the potential of providing deeper insight into the understanding of molecular structures, for example, by selectively exciting different phases in blend systems. [26].

Raman spectroscopy studies of RR-P3HT and its blend with PCBM have been reported for non-resonant excitation conditions [58]. Thermal and solvent annealing of RR-P3HT:PCBM thin films, which often increases the ordering of P3HT molecules, cause a reduction in the full-width-half-maximum (FWHM) of the P3HT symmetric C=C stretching mode (~1445 cm^{-1}) without any observable changes in peak position [58]. However, under resonant excitation conditions, annealing induces a significant shift of the peak position of the C=C mode to a lower wavenumber. However,

unannealed RR-P3HT:PCBM thin films exhibit a shift in the peak position of the C=C mode to a higher wavenumber with increasing excitation energy, as illustrated in Figure 3.1.

Figure 3.2 shows the Raman spectra of a RR-P3HT thin film excited off resonance at 633 nm, exhibiting the various Raman modes of P3HT from 600-1600 cm^{-1} [58]. The main in-plane ring skeleton modes at ~1445 cm^{-1} (symmetric C=C stretch mode) and ~1381 cm^{-1} (C-C intra-ring stretch mode), the inter-ring C-C stretch mode at ~1208 cm^{-1}, the C-H bending mode with the C-C inter-ring stretch mode ~1180 cm^{-1}, and the C-S-C deformation mode at 728 cm^{-1} can be seen in the full spectra [26,58,60]. Of these various Raman modes, focus is on the in-plane ring skeleton mode at ~1445 cm^{-1}, as it is sensitive to the π-electron delocalization (conjugation length) of the P3HT molecules.

The on-resonant and off-resonant spectra of RRa-P3HT and RR-P3HT are compared in Figures 3.3 a) and b) [60]. First, comparison of the off resonant spectra in Figure 3.3 a) shows that the Raman signal of the C=C mode of RR-P3HT films is much larger than that of the RRa-P3HT. This is a result of the fact that RR-P3HT film absorbs more strongly at 633nm, which induces a pre-resonant Raman effect leading to an increase in the intensity of the Raman peaks, whereas the RRa-P3HT film does not absorb much at 633nm.

However, a significantly noticeable difference between the two spectra is the change in FWHM, even though these two films have completely different π- π packing tendencies. The different π- π packing tendencies should result in different electronic states of the C=C bond, which should be represented by spectral shifts;

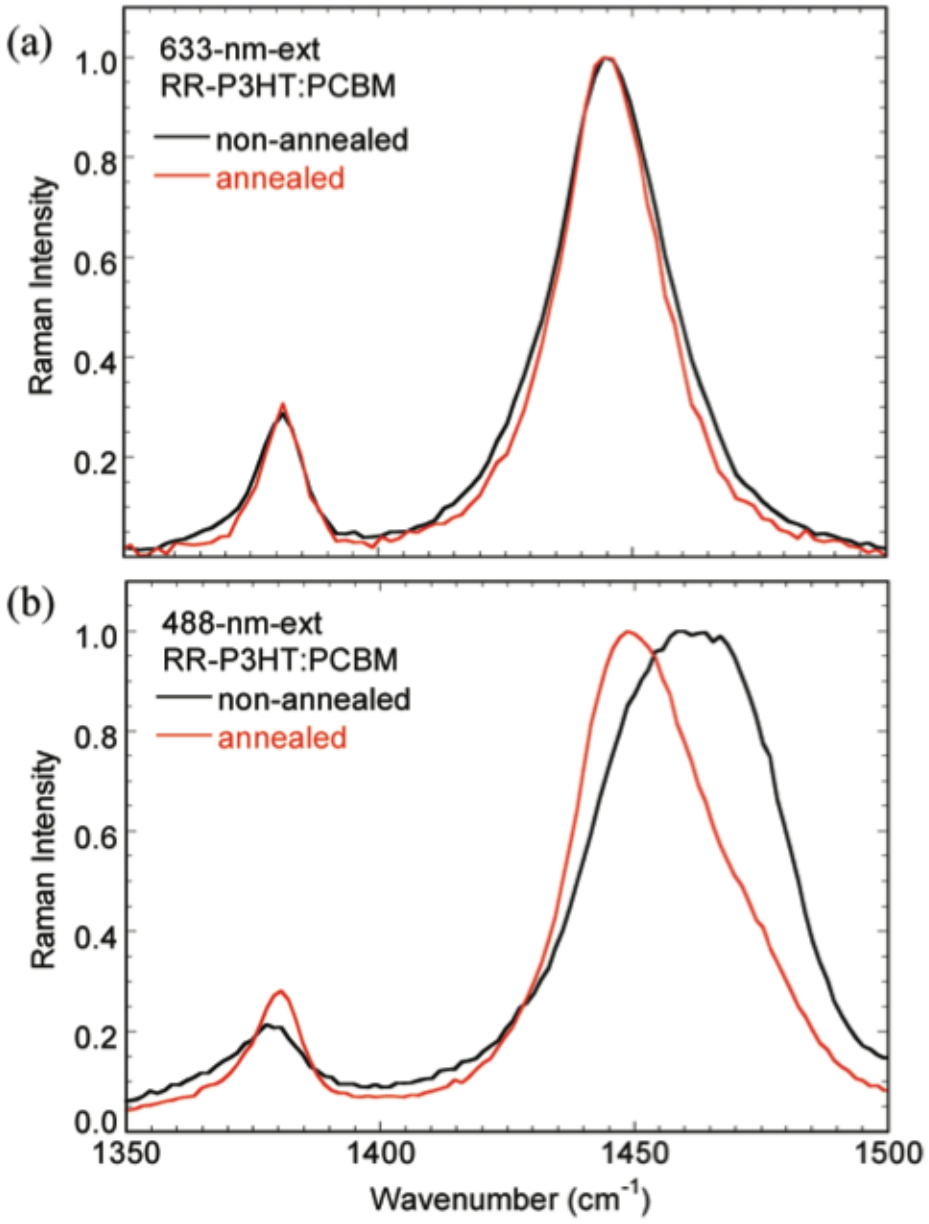

Figure 3.1. (a)Raman spectra (C=C and C-C modes) of unannealed and annealed RR-P3HT:PCBM thin films under 633 nm excitation. (b) Raman spectra (C=C and C-C modes) of unannealed and annealed RR-P3HT:PCBM thin films under 488 nm excitation.

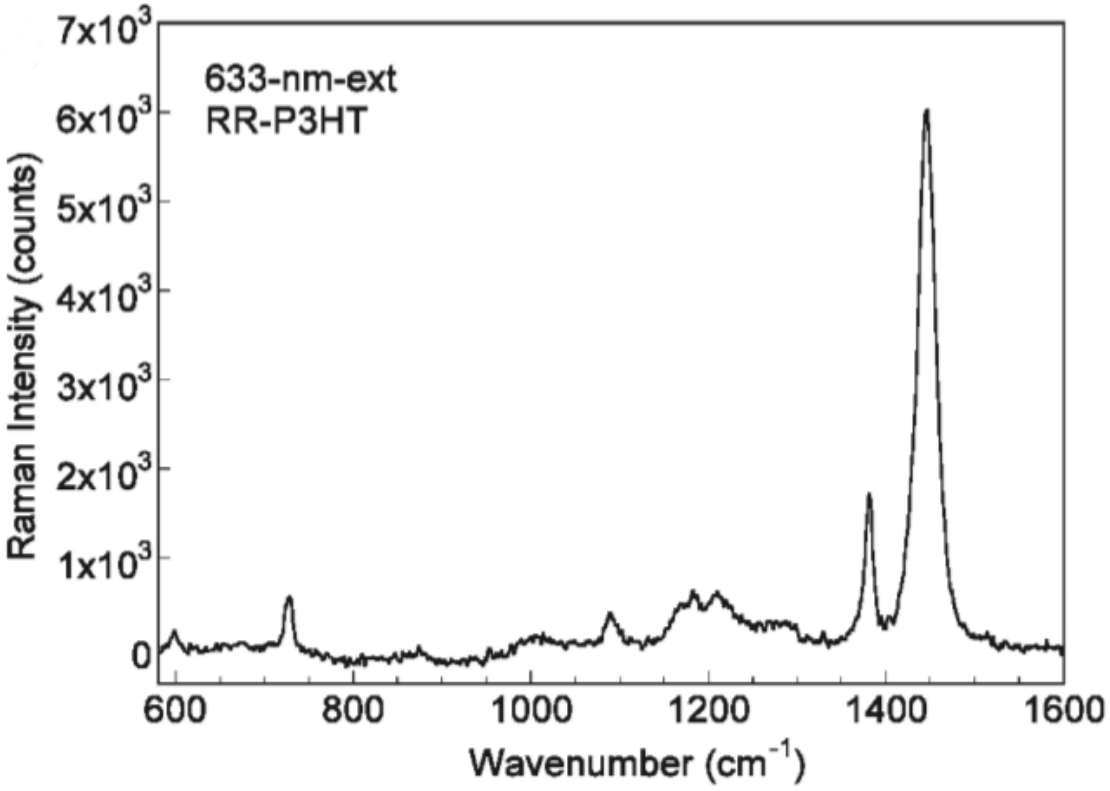

Figure 3.2. Raman spectrum of RR-P3HT thin film under 633 nm excitation.

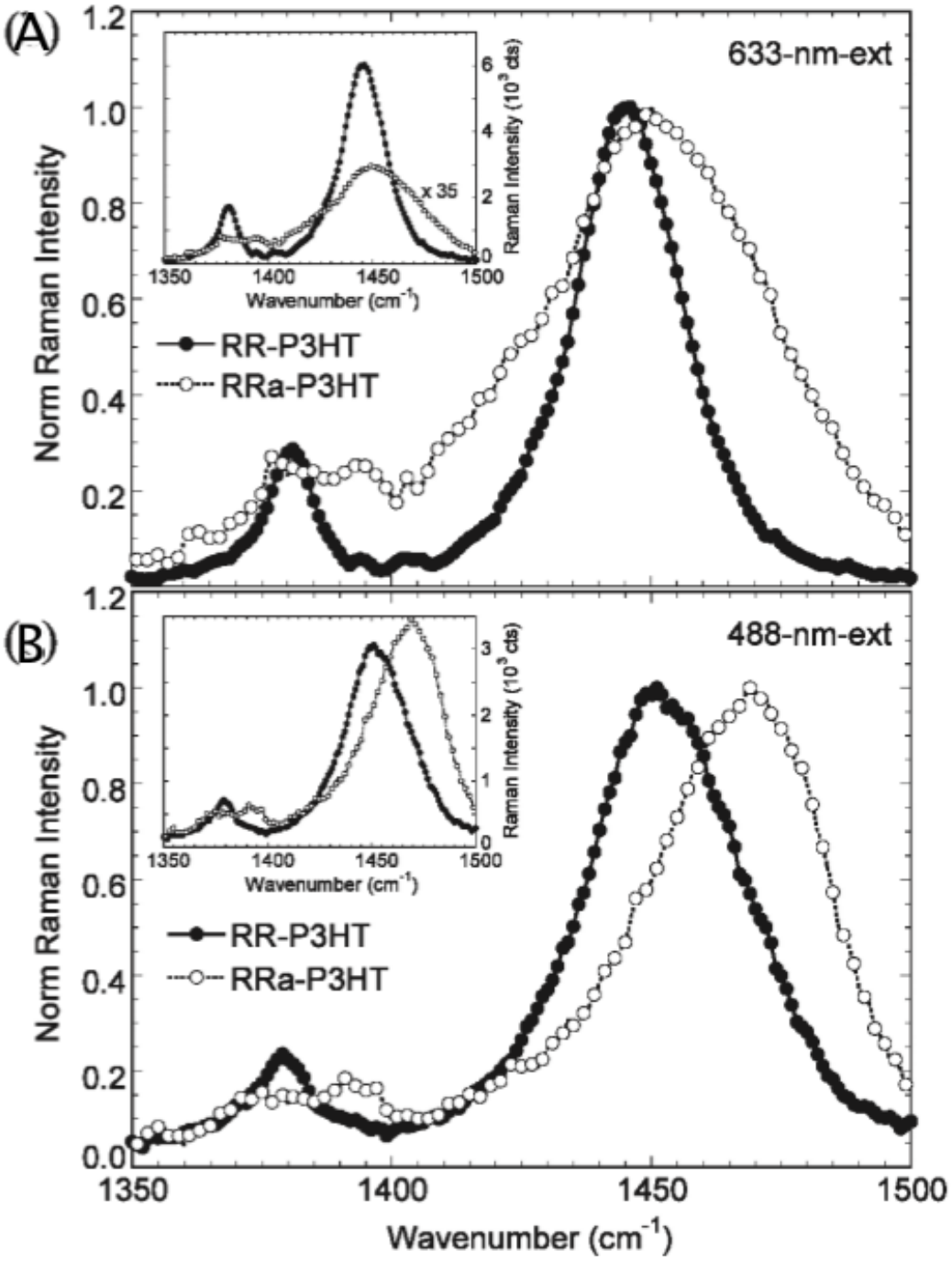

Figure 3.3. (A) Normalized Raman spectra (C=C and C-C modes) of RR-P3HT and RRa-P3HT thin films under 633 nm excitation. The raw spectra are shown in the inset. The intensity of the Raman spectrum of RRa-P3HT thin film is magnified by 35 times for better visualization. (B) Normalized Raman spectra (C=C and C-C modes) of RR-P3HT and RRa-P3HT thin films under 488 nm excitation. The raw spectra (not magnified) are shown in the inset [4].

the absence of these shifts leads to the need to probe deeper with on-resonant Raman. When examining the RR-P3HT and RRa-P3HT films under resonant conditions ((488nm), Figure 3.3 b), where both films show comparable absorption features, the Raman intensity of the C=C mode of the RRa-P3HT film is significantly enhanced and becomes similar to that of the RR-P3HT film. However, the C=C mode of the RRa-P3HT shows a large shift to a higher wavenumber in its maximum peak position (shifting from ~1450 to ~1470 cm^{-1}) and a much narrower FWHM as compared to the off resonant spectrum (633nm).

More importantly, when comparing the as-cast and annealed samples in Figure 3.4, significant changes in the ordering of the molecules are known to occur in the RR-P3HT films relative to that which occurs in the RRa-P3HT, which is reflected in the Raman spectra. That these changes in the spectra are a result of molecular ordering can be more clearly seen when comparing the Raman of blended films of P3HT and PCBM to that of the neat P3HT thin films, as shown in Figure 3.4. Because the C=C peak is sensitive to the degree of molecular order of the P3HT, the disorder created by the introduction of PCBM into the as-cast sample is readily observed in the significant spectral changes.

Under 633nm excitation, there is no significant changes in the peak position or FWHM of the C=C peak in RR=P3HT:PCBM as the sample is thermally annealed. On the other hand, under resonant conditions (488nm), the peak position of the C=C mode in the as-cast RR-P3HT:PCBM blend film lies between that of the RR-P3HT and the RRa-P3HT neat films. This observation indicates that the P3HT molecules in the as-cast RR-P3HT:PCBM blend film still contains more molecular

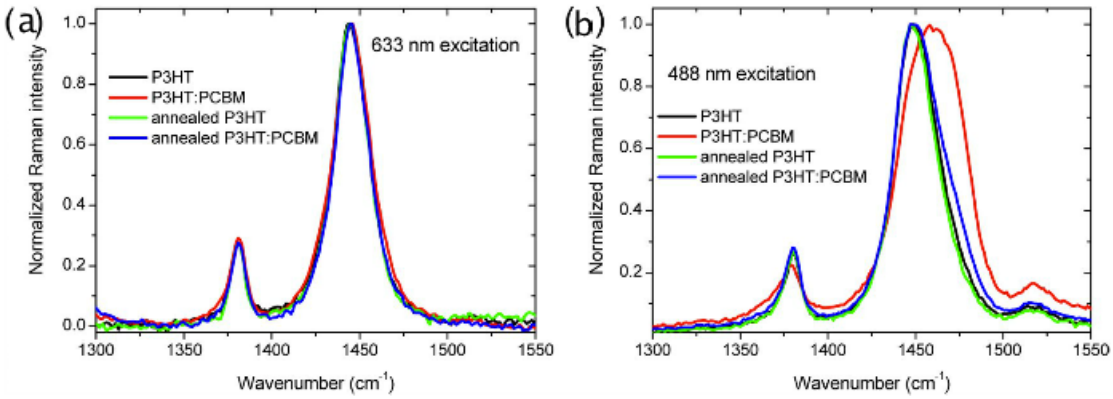

Figure 3.4. A) Raman spectra at off resonant conditions (633nm) B) Raman spectra at on resonant conditions (488nm) Note the peak shifts not visible with P3HT annealing in a) are more visible in b).

order than the largely disordered RRa-P3HT film, although it is less ordered than in the neat RR-P3HT film. The broader FWHM of the C=C peak also indicates the possibility of the existence of different electronic states of C=C as a result of conformational changes [60].

These significantly different characteristics of the Raman peaks that are observed in the ordered and disordered P3HT samples under resonant excitation provides a method to monitor the degree of molecular order of P3HT in thin films, and hopefully can be used to develop a better understanding of the effects of PCBM on the morphology and ordering of P3HT in these mixed thin films.

Upon closer inspection of the spectra in Figure 3.5, the C=C line shapes show significant deviation from an idealized Lorentzian line shape, i.e. they contain overlapping transitions or shoulders, again suggesting contributions from more than one component. Grey and coworkers demonstrated that the C=C Raman band of P3HT actually consists of two components, one centered at ~1450 cm^{-1} ($I_{C=C}^{agg}$) and the other at ~1470 cm^{-1} ($I_{C=C}^{unagg}$) [57], denoting aggregated and unaggregated populations of the P3HT chains, respectively. Moreover, a change in the relative intensities of these two peaks denotes changes in the concentrations of the components that contribute to these peaks; which can be readily monitored by analysis of the observed spectral shifts and overall line shape changes.

Due to alterations in the P3HT packing, interactions with PCBM, and order, changes in the absorption spectra can be broken down into two contributing species. The lower frequency component is assigned as an aggregated P3HT C=C species ($I_{C=C}^{agg}$) and the higher frequency component is assigned to the

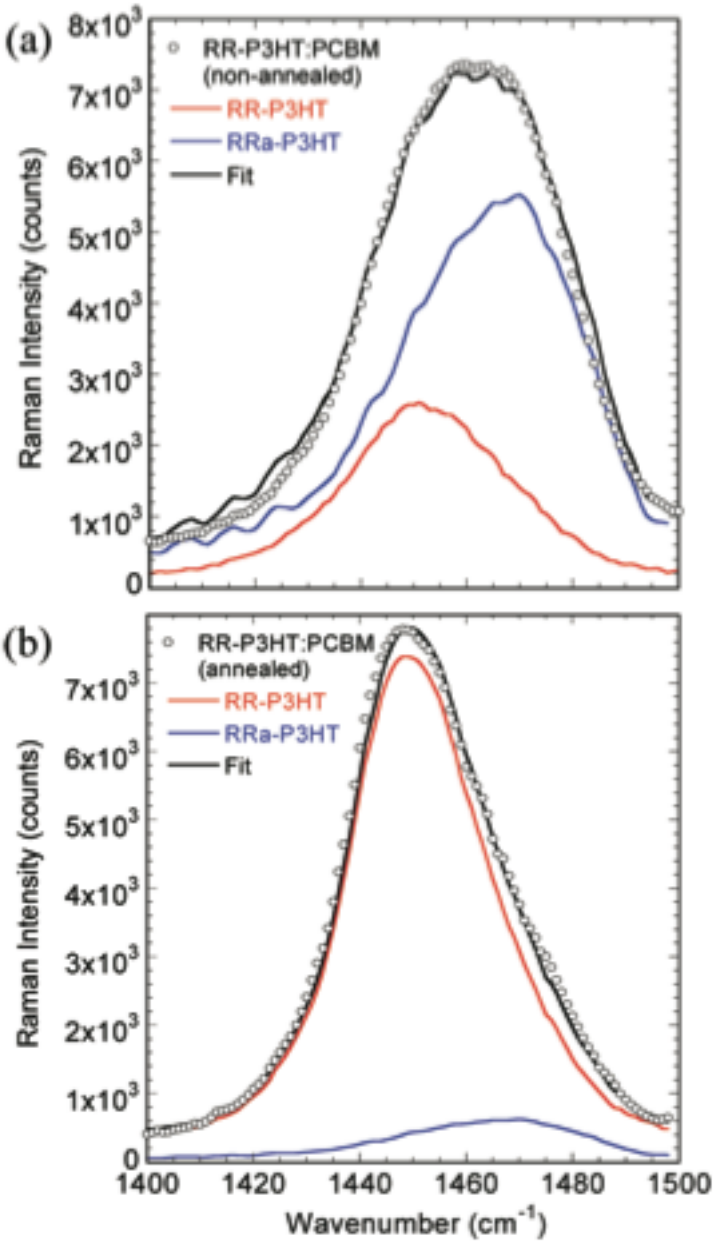

Figure 3.5. Raman spectra (C=C mode) of (a) nonannealed and (b) annealed RR-P3HT:PCBM films with the weighted Raman spectra of RR-P3HT and RRa-P3HT thin films used to fit the experimental spectra at 488 nm excitation.

unaggregated P3HT C=C species $I_{C=C}^{unagg}$). The terms aggregated and unaggregated are to be taken loosely, for these are really just representative of the conjugation lengths. Aggregated species represent P3HT chains with larger intra- and inter-chain order or behave H-aggregate-like with longer conjugation lengths, whereas the unaggregated species correspond to chains with lower intra- and inter-chain order and shorter conjugation lengths. These aggregated components are envisioned as a more planar, semi-ordered species with longer conjugation lengths and the unaggregated chains as disordered with twisted conformation and shorter conjugation lengths [26,57].

Extending the work of Gao and Grey [57], Raman spectroscopy can be used to determine the degree of aggregation in samples made by a variety of fabrication procedures and thus monitor the impact of the presence of PCBM on the ordering of P3HT. Assuming that the Raman scattering cross sections of both $I_{C=C}^{agg}$ and $I_{C=C}^{unagg}$ components do not change in the films, the ratio, R, of Raman intensities of both components is taken as a measure of the relative concentrations of aggregated and unaggregated species, (Equation 3.1).

$$R = {I_{C=C}^{agg}}\Big/{I_{C=C}^{unagg}} \qquad (3.1)$$

Later, a slightly modified interpretation of the amount of aggregated and unaggregated species present is used, which is more closely related to the percent aggregation (Equation 3.2). This parameter is calculated from the area of the aggregated and unaggregated peaks ($A_{C=C}^{agg}$ and $A_{C=C}^{unagg}$) based on the fit of the P3HT C=C peak to two Lorentzian peaks, as shown in Figure 3.6. This information

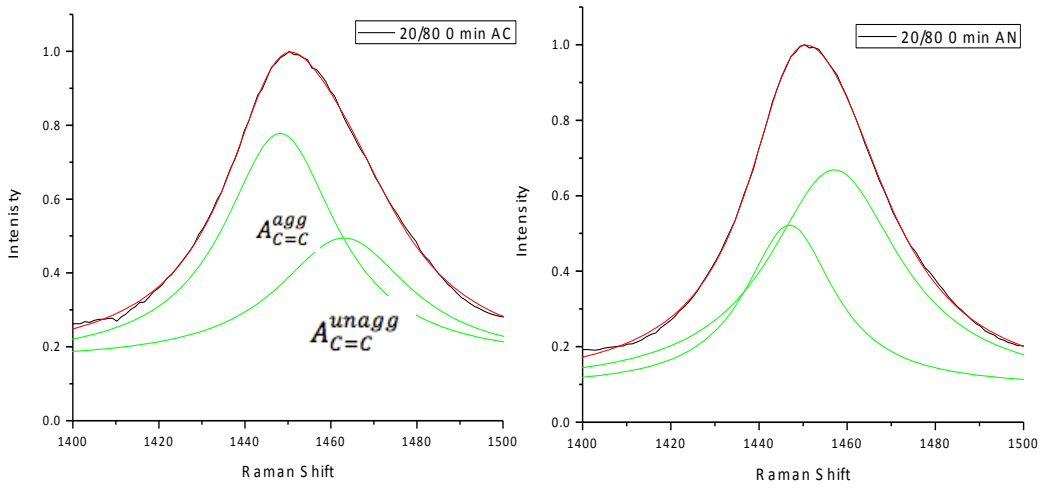

Figure 3.6. Lorentzian fitting of Raman spectra results in the area of the two different contributing species. ~1450 cm^{-1} for the longer conjugation length (aggregated) species and ~1470 cm^{-1} for the shorter conjugation length (unaggregated) species

allows us to estimate the percent aggregation of the thin film, a parameter that can be used to quantify the extent of local ordering of the P3HT chains in the P3HT neat films and P3HT:PCBM blend films [57].

$$Percent\,Aggregation = \frac{A_{C=C}^{agg}}{A_{C=C}^{agg} + A_{C=C}^{unagg}} \qquad (3.2)$$

3.2 Experimental

3.2.1 Photoluminescence

Absorbance and photoluminescence (PL) spectra were obtained from thin film samples on glass cover slides and from solutions in a quartz cell (Starna). The absorbance spectra were obtained using a Varian Cary 5000 spectrophotometer operating between 200 and 1800 nm. Photoluminescence of the samples was measured with a Fluorolog-3 FL3-222 (JY Horiba), using excitation wavelengths between 250 and 450 nm.

3.2.2 Raman Spectroscopy

The Raman experiments were completed with a Ti:sapphire laser (Spectra-Physics, Tsunami) that is pumped with a 532 nm Nd:YAG laser (Spectra-Physics, Millenium XV). The wavelength range of the Ti:sapphire is 690 – 1050 nm that generates a 5 ps pulse (as measured with an autocorrelator at 940nm) at a rate of 81 MHz. The laser was tuned to a wavelength of 942.5 nm, as measured by a NIR/VIS spectrometer (Ocean Optics, USB4000). The output of the laser is 1.2 Watts that is polarized using a Glan polarizer (Thorlabs). The vertical polarization of the laser is sent to a frequency doubler (Spectra-Physics), which produces the wavelength (471.25 nm) that is used as the excitation source. Before entering the

microscope, the light passes through a beam expander, which allows for tighter focusing of the beam by the objective. In the inverted microscope (Nikon, Ti-U), an 80/20 beamsplitter (Semrock) reflects the excitation beam through an objective (Nikon, 20x, NA=0.5), which is focused on the sample. The objective collects the back-scattered light, transmitting it through the beamsplitter, and then to either the eyepiece or a spectrometer (Acton, Princeton Instruments) with a back-lit CCD LN-cooled detector (Princeton Instruments , PIXIS 100). The Raman spectrum of liquid cyclohexane was used to calibrate the spectrometer. Rastering of the sample stage allowed for an average sample spectrum to be taken.

3.2.3 Grazing Incidence X-ray Diffraction

X-ray diffraction patterns of the thin films were obtained with a Phillips X'pert-Pro diffractometer in grazing-incidence geometry. The angle of incidence between the X-ray and the thin film surface (Ω) was 0.3° for all samples. All spectra were normalized to high q, to account for any variation in the volume of sample exposed to the beam. The size of the polymer crystallites is calculated using

$$CrystalSize = \frac{0.9\lambda}{\beta \cos\theta} \tag{3.3}$$

Scherrer's equation (Equation 3.3) [48,49], where the full width at half maximum, β, and the theta position of the crystalline peak, θ, were extracted from the resultant diffraction pattern. The area under the crystalline peak is proportional to the amount of crystalline P3HT. To maintain consistent results from sample to sample, Igor was used to fit the (100) peak, where first the same integration range was used for all samples. Multiple fit integration ranges were tested to verify that the

integration window does not alter the analysis. Also, during the Gaussian fitting, a linear baseline was applied to the peak in order to eliminate the influence of intensity of the overall spectra on the area of the peak. . The error associated with this analysis is ~0.04 which is smaller than the symbols in the figures and thus no error bars appear in the plots[61] .

3.2.4 Sample Preparation

Initial photoluminescence and Raman spectroscopy experiments were completed on samples that contained [6,6]-phenyl C_{61} butyric acid methyl ester (PCBM) and poly(3-hexyl thiophene) (P3HT) that was received from Sigma-Aldrich with a regio-regularity ≥ 90%, molecular weight of 20-30k, and a PDI of 1.5. The solvents, ortho-dichlorobenzene (ODCB) and dichloromethane (DCM) were purchased from Sigma-Aldrich and used as received. To fabricate the mixed thin films, PCBM and P3HT were co-dissolved in ODCB at a concentration of 10mg/mL. The initial PL and Raman samples were prepared on glass cover slides. However, after starting the project, it was realized that impurities in P3HT have a dramatic affect on the packing of P3HT in the layer [62], therefore better quality P3HT from Rieke Metals and PCBM from Nano-C were used in subsequent experiments. Also after realizing a more detailed analysis of the Raman spectra is required to accurately monitor the targeted parameters, the substrates were switched to silicon (Si) wafers.

Prior to casting, the solutions were allowed to dissolve for approximately 12 hours, then heated to 55 °C for several hours before spin coating, in order to achieve complete dispersion. The samples were spin coated at 1000rpm for 90 seconds. All

annealing took place in a vacuum oven at 150 ° C and time frames between sample preparation and analysis were kept constant.

3.3 Preliminary Examination of Neat P3HT and Mixed PCBM/P3HT Thin Films

For our first experiments, a wide range of sample processing procedures was chosen to be examined. There are multiple methods available to control the morphology and ordering of P3HT and P3HT/PCBM thin films. The most common of these is thermal annealing, where the miscibility of a conjugated polymer and fullerene can play a significant role in the ordering of the polymer and the ultimate morphology of the thin film. The interactions between components that exist in a miscible system will vary dramatically from those in phase-segregated systems, creating different packing environments for the conjugated polymer. It is known, based on previous work in our group, that the miscibility limit of PCBM in P3HT is about 22% [51] . Thus, with this knowledge, the research program was designed to first examine pure P3HT thin films, followed by integrating PCBM into the system where P3HT and PCBM are miscible to document the impact of the presence of PCBM on the ordering of the P3HT in the miscible regime, i.e. 80% P3HT/20% PCBM. Finally, the impact of the PCBM on the ordering of P3HT in a phase segregated system is examined, as this system more closely mimics those that are used as active layers in OPV devices.

3.3.2 Understanding Exciton Dissociation in P3HT and PCBM/P3HT Thin Films via Photoluminescence

Figure 3.7 shows the photoluminescence curves of the neat P3HT and PCBM/P3HT mixed samples that were examined as-cast, as well as after annealing

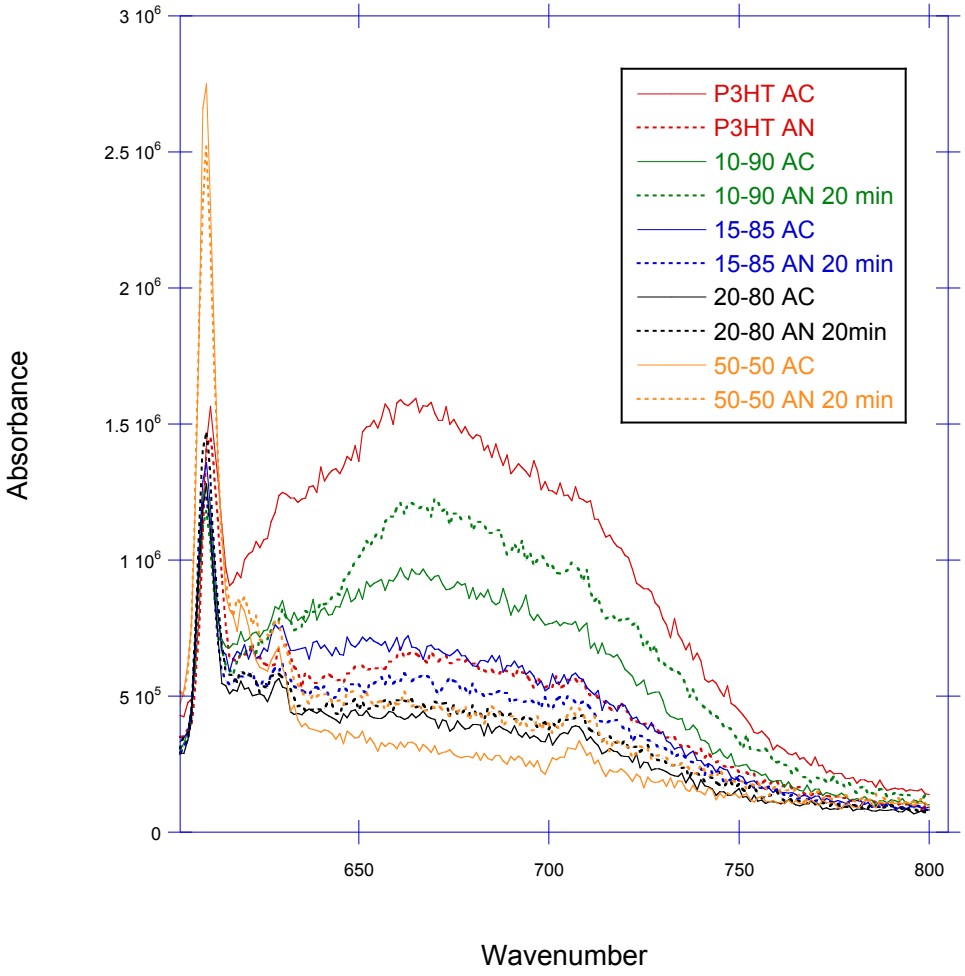

Figure 3.7. PL data of neat P3HT and mixed thin films for as cast (AC) and 20 minute annealed (AN) samples.

at 150 °C for 20 minutes. A decrease in the emission of the PL spectra, often termed 'quenching' the photoluminescence, indicates that the recombination of the exciton is decreased, which means that it must decay by other, non-radiative processes, such as dissociation at a donor:acceptor interface. Thus, an increase in quenching is beneficial for OPV performance because it means that the exciton has reached the interface between the acceptor-donor layers before recombining.

For P3HT neat thin films, a large amount of florescence or emission is observed from the as-cast sample. This high intensity of the PL is a result of emission due to recombination from the various phases (amorphous and crystalline) of P3HT that exist in these samples. As the sample is annealed, less emissive PL intensity is observed, which correlates to the formation of more ordered phases of P3HT molecules, implying that the presence of the more ordered phases improves exciton dissociation. Therefore, these PL results suggest that there exists an increase in the quenching of the PL within this P3HT layer with a small amount of thermal annealing. This is interpreted to indicate that thermal annealing of the sample allows for the polymers to pack into more ordered domains. Dissociation is more efficient in the annealed films since the polymer chains in the lamellae are longer and closer to each other, so that the contact points between any two adjacent chains are therefore more extended. These extended contact points for the polymer chains in the lamellae leads to more mobile excitons [59], and a decrease in recombination. However, with further annealing, the photoluminescence properties do not change any further.

The role of the introduction of PCBM on the ordering of P3HT molecules is of crucial importance, as this ordering is important for efficient charge transport. The presence of PCBM may disrupt the packing ability of the P3HT molecules as illustrated in Figure 3.8. Determining the degree to which this intrusion occurs in mixed P3HT/PCBM thin films, and the impact of the specific fabrication procedure on this disruption of chain ordering, is the target of these studies, as it provides crucial molecular level information that is required to develop fabrication processes that will result in more efficient devices.

Experiments were begun by introducing a small amount of PCBM into the P3HT to form a 10/90 PCBM/P3HT mixed thin film. All of the PCBM is miscible in the P3HT at this loading level. Inspection of Figure 3.7 shows that the 10/90 as-cast sample has a lower photoluminescence than the annealed 10/90 sample or the as-cast pure P3HT film, which translates to there being more exciton dissociation in this sample than the other two. The annealed sample shows less "quenching" or exciton dissociation because with annealing there is less amorphous P3HT present, which is the phase where the P3HT and PCBM are intimately mixed, limiting the extent of interaction between the PCBM and P3HT.

The 15/85 PCBM/P3HT mixed thin films exhibits a PL spectra that suggests the interaction of the PCBM and P3HT dominates the PL response more in this sample than in the 10/90 sample. In the 15/85 sample, the as-cast sample more efficiently dissociates excitons, which corresponds to a significantly lower PL emission. It appears that the good intermixing between PCBM and P3HT that occurs in this miscible sample creates ample heterojunctions for exciton dissociation.

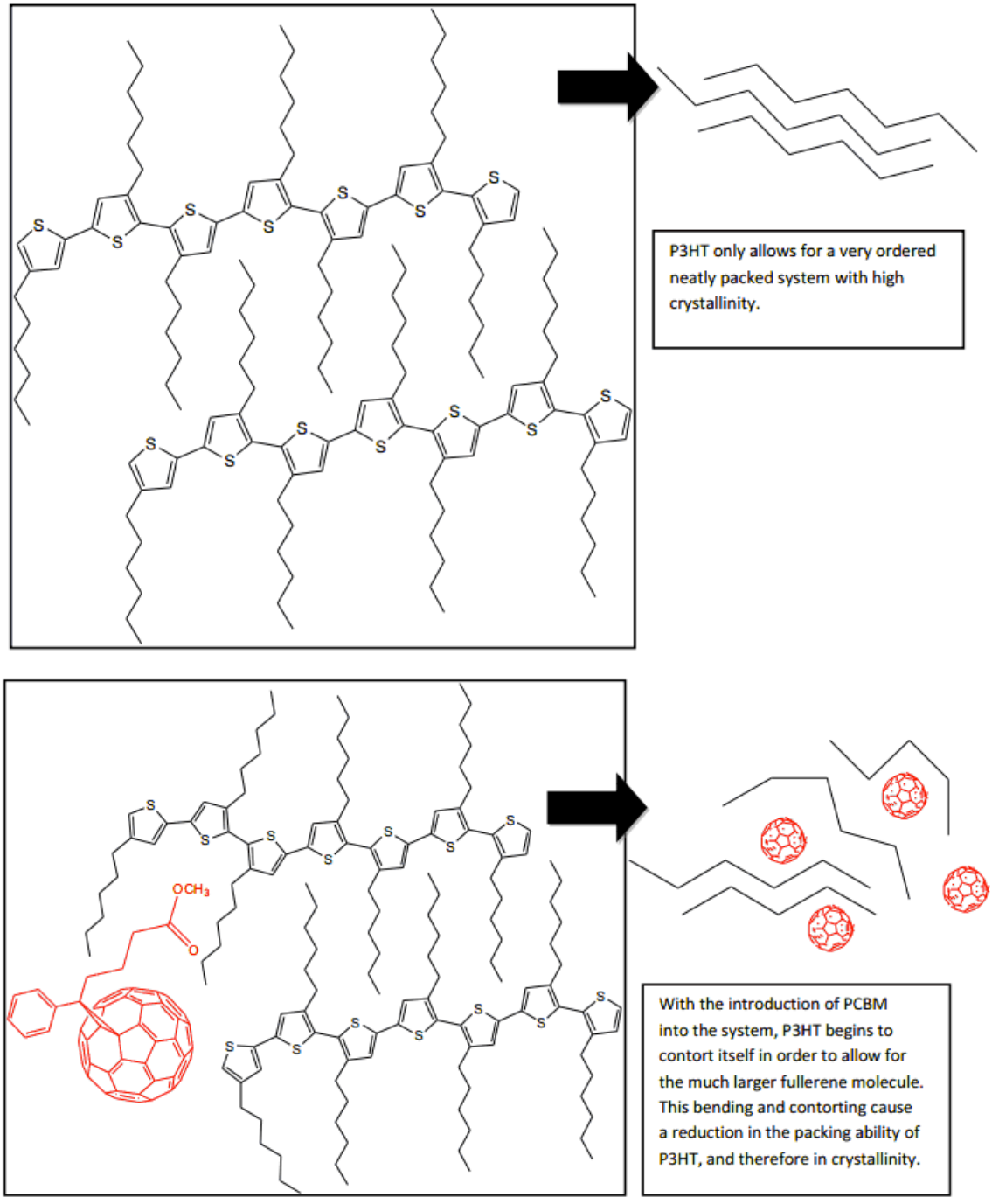

Figure 3.8. Schematic showing the ability of the large PCBM molecules to disrupt the alky chains and resultant order and packing ability of P3HT

However, unlike the 10/90 sample, where thermal annealing negatively impacted exciton dissociation, annealing appears to increase exciton dissociation in the 15/85 sample. As the P3HT domains become more ordered with annealing in this samples, however, there remains sufficient amorphous P3HT in the system to still provide adequate mixing of the P3HT and PCBM molecules for efficient exciton dissociation, evident with the increased "quenching" of the annealed sample.

As the miscibility limit of PCBM and P3HT is approached with the 20/80 samples, the PL results indicate that the PCBM remains significantly mixed with the P3HT. Both the as-cast and annealed sample show a very large amount of "quenching", which indicates an increase in the extent of exciton dissociation. There is a small, negligible increase in the PL spectra with annealing. Structurally this could correlate to an increase in the amount of amorphous P3HT, as a large amount of PCBM has been introduced into the system. This would account for the increased imtermixing of the PCBM and P3HT that allows for efficient exciton dissociation. The increase in the amount of amorphous P3HT may be the result of the disruption of the P3HT ordered domains by PCBM. Summarily, these PL results indicate that the amount of PCBM in the amorphous phase dominates the amount of exciton dissociation in these samples where there is extensive mixing between the P3HT and PCBM in the amorphous phase, which creates more interfacial area between P3HT and PCBM that efficiently dissociates excitons.

Finally, a 50/50 PCBM/P3HT phase segregated sample that contains a crystalline P3HT phase, a pure PCBM phase and a mixed amorphous phase that consist of P3HT and PCBM was examined. The as-cast 50/50 sample forms a

relatively homogeneous distribution of PCBM throughout the sample that is due to the rapid solvent evaporation during spin coating. This distribution of PCBM results in a sample with the most interfacial interaction between PCBM and P3HT, enabling efficient exciton dissociation. This morphology exhibits the most "quenching" of any of the samples tested. However, as the sample is annealed, the PL increases, which coincides with the phase separation of the mixture, and increase in P3HT ordering. This morphological change results in fewer PCBM/P3HT interfaces for exciton dissociation. It is interesting to note that the annealed 50/50 annealed sample has the same emission as the 20/80 samples, which suggests that the amorphous phase of the 50/50 samples phase segregates to a composition that approaches the 20% PCBM miscibility limit, and that the amount of PCBM thermodynamically mixed into the P3HT amorphous phase dominates (controls) the photoluminescence.

It is also interesting to note that the PL data indicates that as the PCBM concentration is increased from 10 to 15 to 20%, the photoluminescence decreases, but increasing the PCBM content up to 50% does not further decrease the photoluminescence. This implies that the amount of dissociation increases with PCBM loading until the miscibility limit of 20% PCBM is reached. It appears that the increased miscible PCBM in the system provides additional donor:acceptor interfaces, which allows dissociation to occur more efficiently. This leaves the role of ordered P3HT domains in the dissociation process uncertain. Therefore, these domains of P3HT need to be probed further to better understand their importance in the operation of an OPV active layer, as well as the affect of the presence of PCBM

on the packing and ordering of P3HT, as these parameters may dramatically impact the resultant potential performance of the solar cell device.

3.3.3 Use of Raman to Investigate the P3HT Ordering in Active Layers

After monitoring the effect of varying the amount of fullerene available in the P3HT domains on exciton dissociation, the need to delve deeper into the molecular order of P3HT in these layers was obvious. What structural affect does the PCBM have on the ordering of P3HT? Raman spectroscopy allows us to analyze the P3HT C=C peak to provide the relative amount of "aggregated" and "unaggregated" P3HT, and thus provides a method to track P3HT ordering. According to literature, these species correlate to differences in the conjugation lengths of the P3HT, an "aggregated" species has a longer conjugation length and more planar conformation, while the "unaggregated" species corresponds to a shorter conjugation length or more twisted, disordered conformation [26]. This leads to the question of how the presence of the aggregated and unaggregated species correlate to structural changes of these potential OPV active layers and how various processing procedures impact these structural changes.

Examination of the Raman spectra of PCBM/P3HT mixed films shows the presence of a shoulder in the spectra, verifying the existence of the two contributing species. Figure 3.9, demonstrates the shift in peak position and line shape that is induced with annealing and changes in PCBM concentration. Figure 3.10 illustrates the fitting of the experimental spectra to two Lorentzian peaks, which allows for the quantification of the changes in peak positions and area of each contributing species. Also, Table 3.1 shows the details of this fitting procedure, showing the

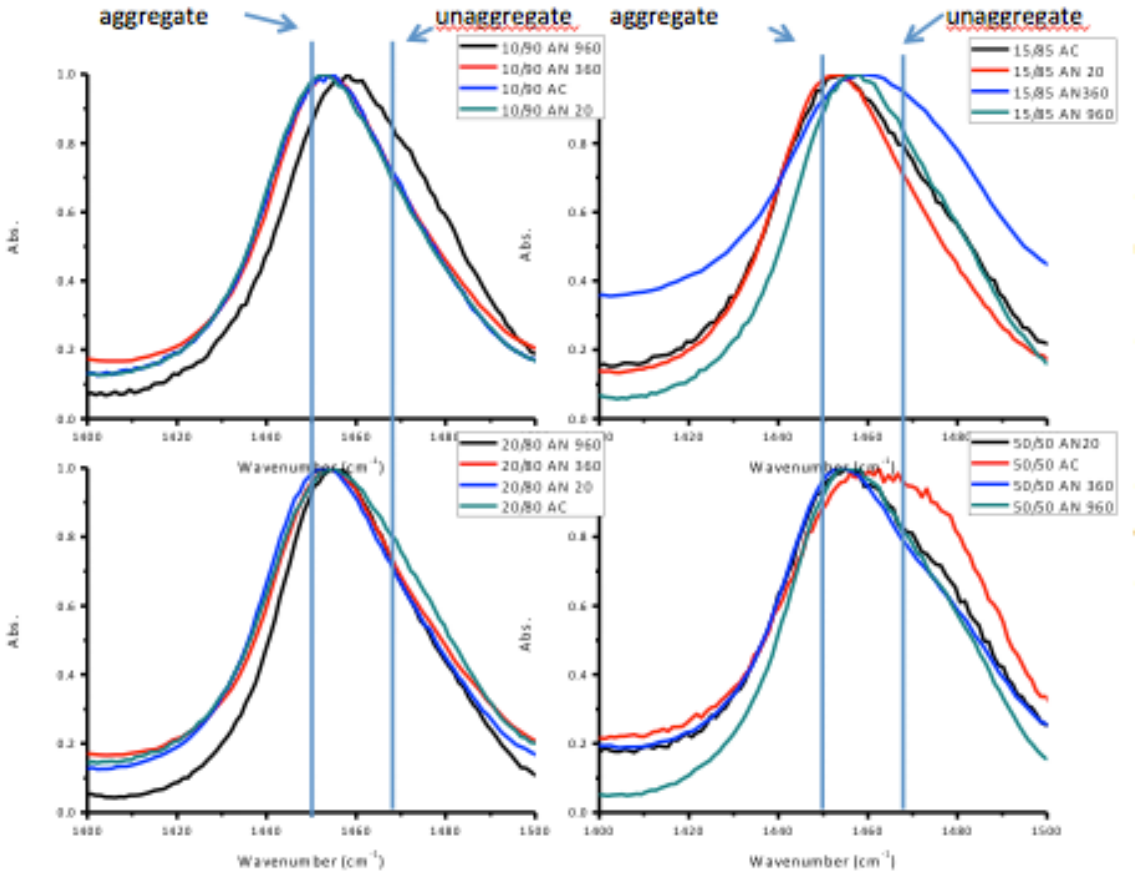

Figure 3.9. Raman spectra of 10/90, 15/85, 20/80, and 50/50 PCBM/P3HT mixed thin films. Shown are the peak shifts with thermal annealing.

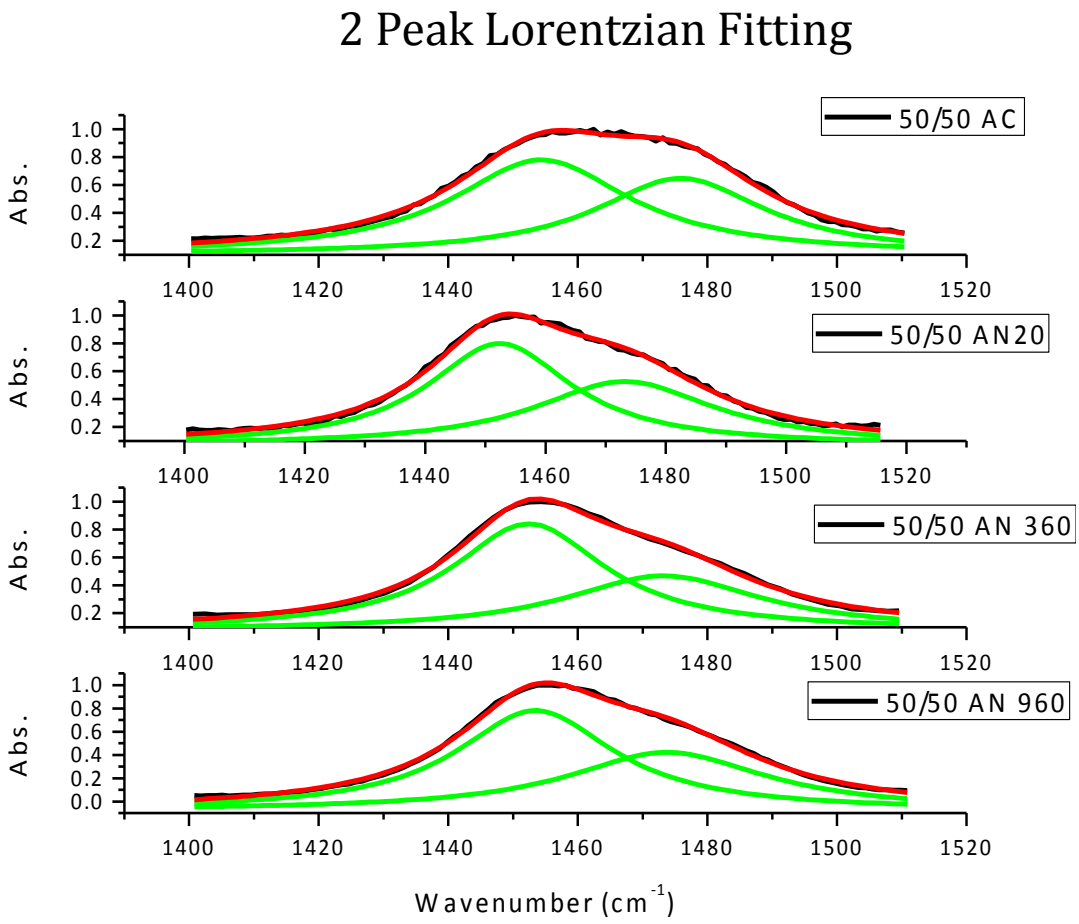

Figure 3.10. Lorentzian fitting of 50/50 PCBM/P3HT mixed thin films. Red line is the fit, Two green lines represent the "aggregated" and "unaggregated" species peaks.

Table 3.1. The area of the "aggregate" and "unaggregated" species, along with the peak height and position obtained from the two peak Lorentzian fitting of the C=C peak in the Raman spectra.

	Area	Height	Wave number	r^2
50/50 AC	35.5659	0.8489	1454.36	0.99713
	27.3266	0.6836	1475.86	
50/50 AN 20	33.4879	0.9157	1452.38	0.99638
	26.4959	0.5748	1473.17	
50/50 AN 360	34.4397	0.9572	1452.42	0.99743
	22.6364	0.4889	1473.21	
50/50 AN 960	39.8947	1.0759	1453.44	0.99818
	29.2434	0.6241	1473.79	

quality of the peak fit. The classical Hamiltonian origins of the Lorentzian fitting allow for better accountability and interpretation of the asymmetric peak broadening and disorder that is observed in P3HT and PCBM/P3HT spectroscopic emissions. The non-resonant second-order dispersion forces also cause the aggregate phase transition to be more like that of a gas-to-crystal response and Lorentzian profiles have been shown to provide better fitting for gases or liquid like systems, whereas Gaussian profiles work well for solid samples, powders, gels, or resins.

As indicated by the "aggregate" and "unaggregated" peak position lines at ~ 1450 and 1470 cm^{-1}, the overall peak position of the C=C peaks change, and in general, shifts after annealing to a position where the "aggregated" component dominates. This is better demonstrated in Figure 3.11, where the area of each Lorentzian peak, corresponding to the amount of each contributing species, is plotted as a function of annealing time. All three of the miscible systems (10, 15, and 20%) show an initial increase in the "unaggregated" species followed by a dramatic drop with annealing at 150 °C. More notable is the absence of an increase in "aggregated" species with annealing. This spikes our interest because a common conclusion in the literature is that the "aggregated" species is equivalent to the crystalline P3HT [47], and it has been shown that with thermal annealing at 150 °C, there is usually an increase in P3HT crystallinity [63].

Gao and Grey reported their examination of the ordering of P3HT by Raman spectroscopy in terms of the degree of aggregation or R. where $R = I_{C=C}^{agg}/I_{C=C}^{unagg}$. In this equation, $I_{C=C}^{agg}$ is the intensity of the peak associated with the P3HT chains

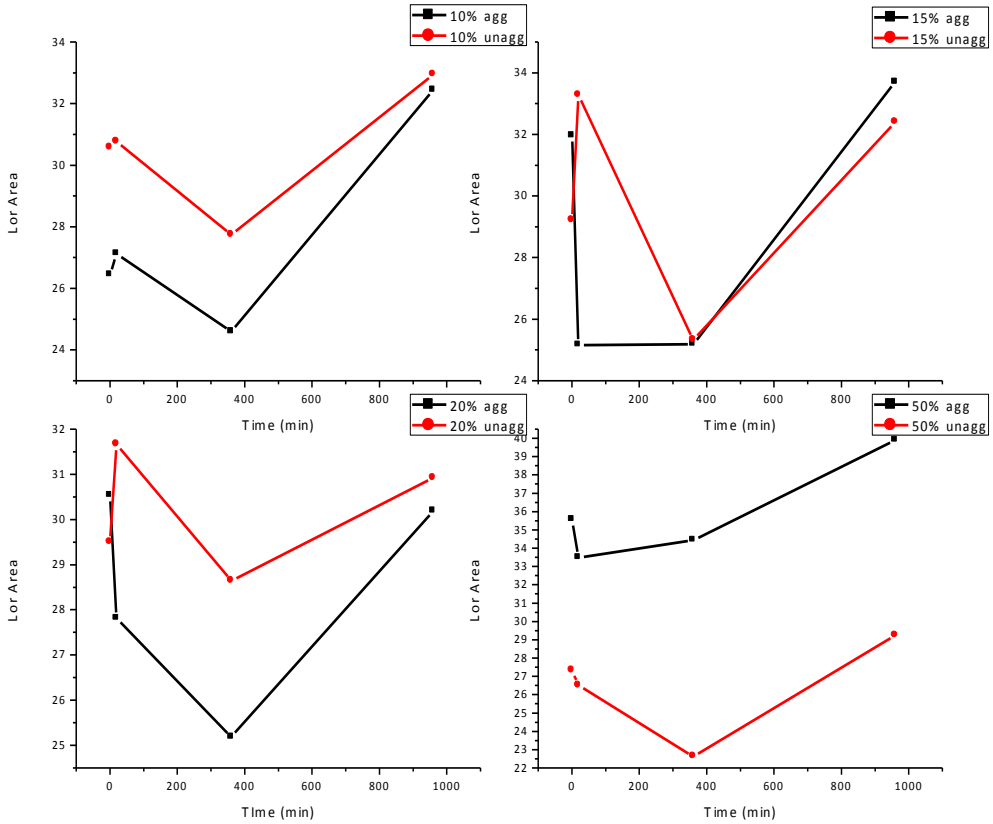

Figure 3.11. Lorentzian area of "aggregated" and "unaggregates" species for mixed thin films versus annealing time.

with larger intra- and interchain order and longer conjugation lengths, whereas $I_{C=C}^{unagg}$ is the intensity of the peak associated with the P3HT chains with lower intra- and interchain order or shorter conjugation lengths.

If the oft-assumed relationship between extent of aggregation and P3HT crystallinity is correct, one might expect a decrease in the degree of aggregation, R, with increased PCBM loading if PCBM disrupts the packing of P3HT. However, after an initial decrease in the extent of aggregation is observed with thermal annealing, as shown in Figure 3.12, the extent of aggregation increases with further annealing for the 10,15, and 20% PCBM sample, i.e. those in the miscible regime, but changes very little with PCBM loading.

Further inspection of Figure 3.12 shows that the 50/50 PCBM/P3HT mixed layers exhibits the highest degree of aggregation, where this increases further with annealing. It is interesting that the degree of aggregation increases with annealing in the 50/50 samples, yet the amount of amorphous P3HT available in the layer should decrease with phase segregation. However, in this system the highest degree of aggregation is observed, yet PL data suggest that intermixing decreases.

Introducing a small amount of PCBM into our system, the 10/90 PCBM/P3HT mixed thin film is examined first. The effect of the presence of PCBM on this system was notable in the PL data, with a promotion of intermixing that increases dissociation, lowering photoluminescence. Further ordering occurs with annealing, which hinders PCBM intermixing and therefore dissociation. Yet, the Raman data

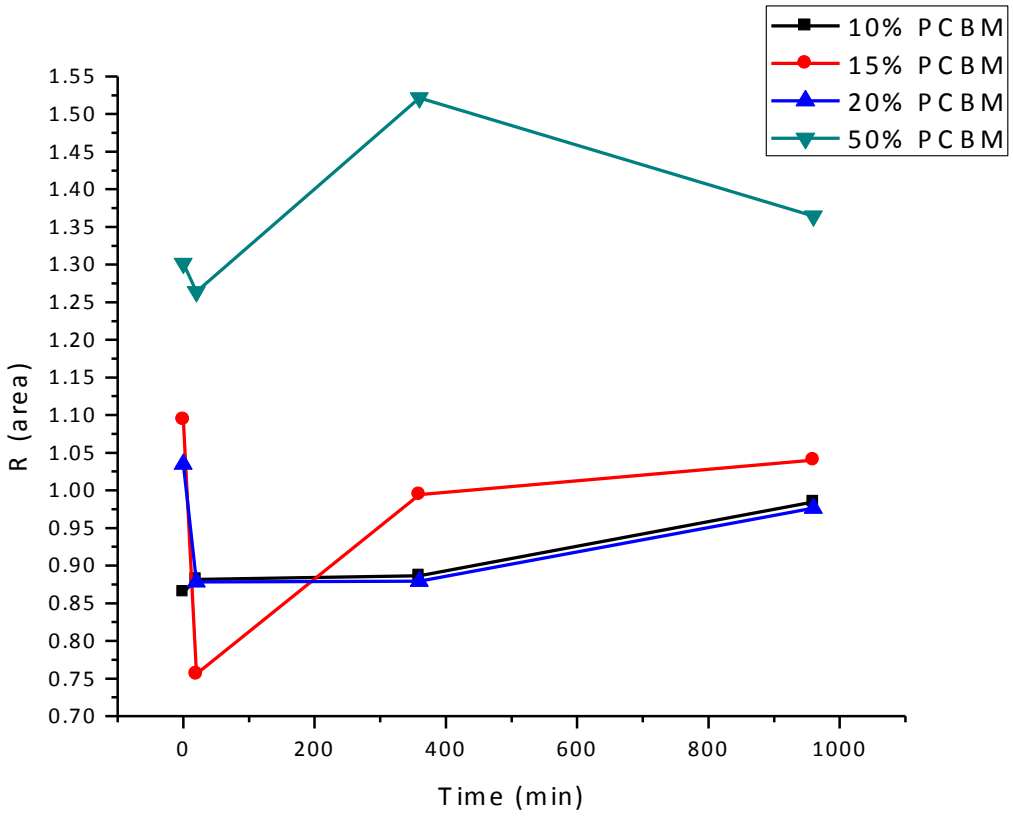

Figure 3.12. R, the degree of aggregation for mixed thin films plotted against annealing time.

indicates that there is a trivial change in the degree of aggregation. It may be that this small amount of PCBM may not be sufficient to disrupt the established P3HT ordered domains, but clearly it is sufficient to induce changes in the exciton dissociation.

The impact of further increasing the amount of PCBM in the active layer on the morphology and P3HT ordering in the film can be realized by examining the 15/85 PCBM/P3HT mixed film. In this sample, a dramatic effect of the presence of the PCBM in the as-cast sample is seen. The as-cast sample quenches the photoluminescence more than the 10/90 system, which can be ascribed to the presence of more PCBM mixed with P3HT in the amorphous phase. This PL data is suggestive of more amorphous P3HT domains, yet there is a high degree of aggregation in this sample, the most of the miscible systems. However with twenty minutes of annealing at 150 °C, a dramatic change is observed in the ordering of this system. The degree of aggregation drops significantly with initial annealing, which corresponds to a decrease in photoluminescence, suggesting more dissociation. Yet with longer annealing times, the degree of aggregation begins to modestly increase. Again literature suggests that the PCBM disrupts and inhibit the packing and ordering of P3HT domains [64], yet there is a significant increase in exciton dissociation at short annealing times.

Increasing the PCBM content further but remaining within miscibility regime, 20/80 PCBM/P3HT mixed films are examined. The degree of aggregation of the 20/80 sample is similar to that of the 10/90 samples, except in the initial as cast sample. Yet, the PL data of the two differ significantly. The 20/80 as-cast sample

dissociate excitons much more readily, indicating better mixing and more intimate interactions between the PCBM and P3HT. Interestingly, this sample has a higher degree of aggregation than the 10/90 as-cast sample. While the Raman results indicate a major structure change by the decrease in R value with annealing, the PL data suggest only a negligible change in photoluminescence. The Raman results indicate that the degree of aggregation initially drops with short annealing times, but levels off with longer annealing times. Still, Raman alone doesn't provide a clear picture of how a change in "aggregated" species corresponds to the amount of amorphous P3HT needed for good intermixing between the two molecules.

Lastly, the examination of the phase-segregated 50/50 PCBM/P3HT film mimics those that are used in OPV devices. A dramatic decrease in the PL data indicates efficient intermixing of P3HT and PCBM, resulting in very proficient dissociation of the excitons that approaches that of the system that is near the PCBM miscibility limit (20%) with annealing. The Raman data shows that this system shows the highest degree of P3HT aggregation, significantly more than the rest of our samples, including the 20% PCBM sample. This high degree of aggregation suggests that a large amount of order exists in this system, where there are more segments with longer conjugation lengths ("aggregated" species) and fewer shorter twisted conjugation length segments ("unaggregated"). The incongruity of the amount of P3HT ordering that is monitored by Raman and the extent of P3HT and PCBM mixing that is monitored by photoluminescence clearly indicates that these two structural parameters are largely decoupled in this phase segregated sample.

3.3.4 Does "Aggregated" Species Equate to Crystallinity?

A common structural interpretation in the literature of the Raman spectra of P3HT is that "aggregation" in P3HT as measured by Raman spectroscopy

$$\%Crystalline = \frac{\Delta H_m}{\Delta H_o} \tag{3.4}$$

$$\Delta H_m = \frac{Area}{MassP3HT} = \frac{Area}{(MassSample)x(\%P3HT)} \tag{3.5}$$

corresponds to P3HT crystallinity [65]. To critically test this assumption, the crystallinities of the P3HT in samples with the same thermal history of those that were studied by Raman spectroscopy were monitored using differential scanning calorimetry. Samples examined by differential scanning calorimetry (DSC) were prepared by solvent casting for direct comparison with the Raman Spectroscopy results. The DSC curve of each sample was obtained from 20 °C to 300°C at 10°C/min. The area of the melting peak determines the melting enthalpy for the sample (ΔH_m), which is proportional to the percent crystallinity of the sample. The percent crystallinity of the P3HT can be estimated if ΔH_0 is assumed to be 99 J/g [66], a commonly used value for ΔH_0. Figure 3.13 shows the comparison between the percent crystallinity calculated from DSC and percent aggregation from Raman. Since there is some discrepancy in literature about the correct value of ΔH_0, the trends in the change in crystallinity and aggregation with % PCBM is analyzed, rather than the absolute amounts. Surprisingly, the extent of aggregation as monitored by Raman and extent of crystallinity as measured by DSC have completely opposite trends, where aggregation increases with PCBM loading, while crystallinity decreases. Perhaps, this suggests that these two parameters monitor

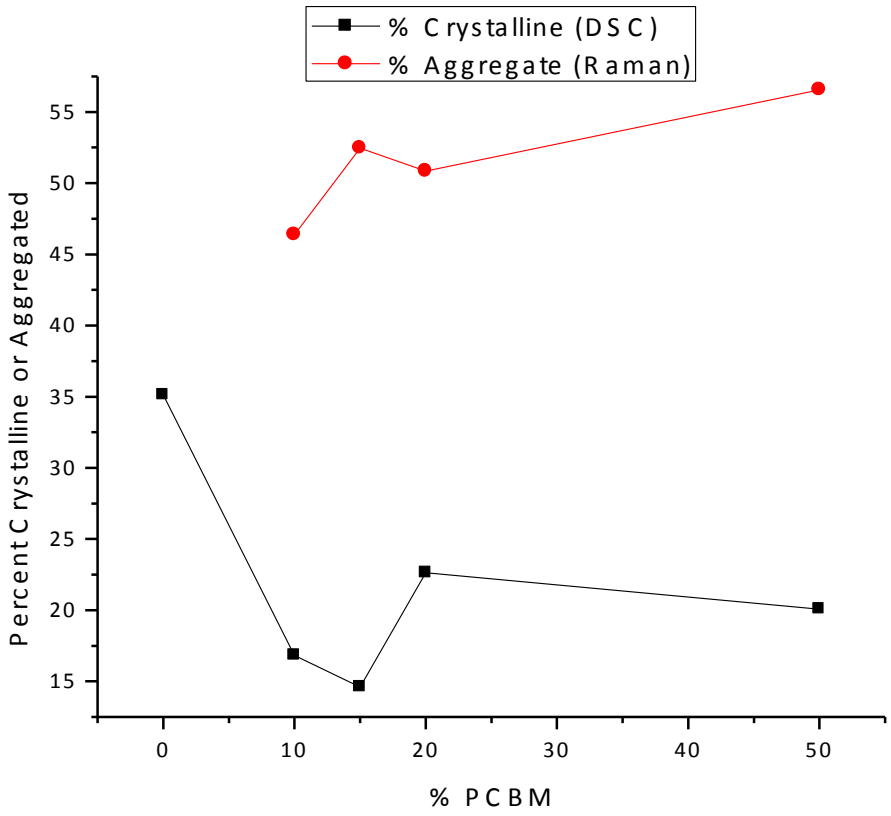

Figure 3.13. DSC percent crystalline data versus Raman percent aggregate data of P3HT/PCBM films.

different structural components in these thin films. Further supporting this interpretation is that RRa-P3HT doesn't show a diffraction peak in GIXRD, indicating that there is no crystalline order in this system, [67] and yet there is a presence of a longer "more ordered" "aggregated" species in the Raman spectra. One possible explanation this discrepancy is that the P3HT in the samples exhibit more than two conformational states, crystalline or amorphous. Rather, there may exist a conformational state in between that of the crystalline and amorphous conformations.

3.4 Grazing Incidence X-ray Diffraction to Probe Local Chain Packing

After examining the structure and photoluminescence of a wide range of P3HT/PCBM compositions, it is clear that further analysis is needed to understand the role of PCBM in the ordering of P3HT in the active layers and to clarify the nature of the "aggregated" species that is monitored by Raman spectroscopy. To realize this goal the experiments focused on a smaller concentration range in the miscible regime to allow for more involved analysis. Also, at this point, the need for a better source of polymer and fullerene became apparent and changing the substrate to Si wafer to allow for a more detailed analysis. The Si wafer allows us to better control the silicon dioxide surface on which the active layer resides. According to literature, higher regio-regularity in the P3HT molecule enables closer packing of the crystalline lamella, which in turns contributes to larger field-effect mobility. Figure 3.14 demonstrates that even though the inter-chain spacing within the thiophene ring plane ($d_{a\text{-}a}$) is found to be unaffected by this variation in RR, the

Figure 3.14 The energy-minimized molecular structure of P3HTs (11 repeating units per chain) for 100% RR (da_a^{100} and db_b^{100} are the *a*-direction and *b*-direction chain-stacking spacings, respectively) and 90% RR (da_a^{90} and db_b^{90} are the corresponding spacings). The *a*-direction and *b*-direction are parallel and perpendicular to the thiophene ring plane, respectively [11].

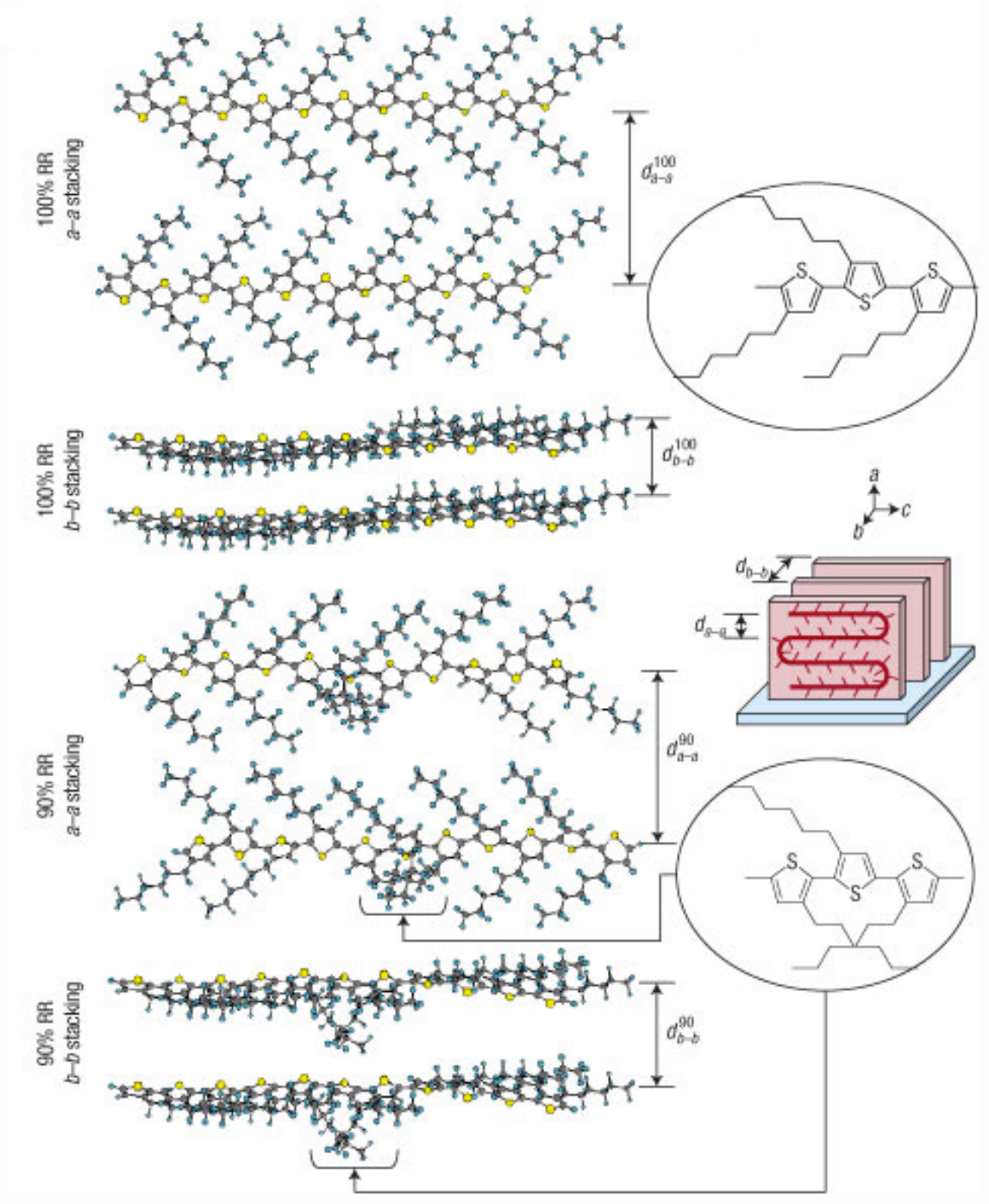

Figure 3.14 Continued

inter-chain spacing perpendicular to the ring ($d_{b\text{-}b}$) increases for lower RR P3HT, verifying that higher RR increases inter-chain interactions [68,69].

From the GIXRD curves of our samples, the extent of P3HT crystallinity can also be monitored, along with the average crystal size from the Scherrer equation (Equation 3.3). To accurately compare the results from GIXRD for different samples, the spectrum of each sample is normalized to high q because at high q the intensity is only proportional to the amount of sample and is not dependent on the sample structure.

Also for each sample, the GIXRD spectra were corrected for the varying amount of P3HT, where the intensity of the peaks and thus area of the peaks are normalized to the amount of P3HT in the sample. Overlaying the spectra from the different thin film samples in Figure 3.15 shows little deviation in the high q scattering curve allowing for the direct comparison of the area of the (100) peak, which characterizes the amount of crystalline P3HT. Both of these techniques are used to monitor and better understand the ordering of P3HT and the impact of P3HT preparation conditions on the organization of the P3HT.

When the Raman spectroscopy data is correlated to the GIXRD results, it becomes apparent that the "aggregated" P3HT as determined by Raman does not correlate to the crystallinity, as was observed in the DSC experiments. Thus, if the P3HT "aggregates" are not P3HT crystals, what physical characteristic is actually monitored by the quantification of the amount of this "aggregated" species. From a spectroscopic standpoint, it is an increase in conjugation length. From a polymer structure standpoint, does it represent changes in crystallinity or crystal size?

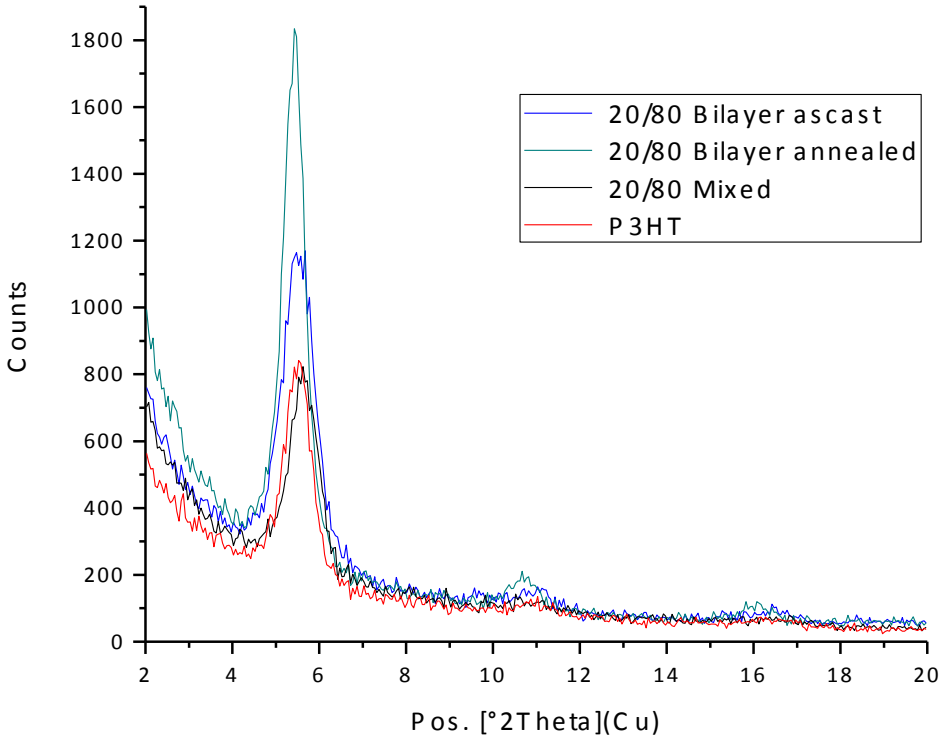

Figure 3.15 GIXRD spectra. Relatively the same intensities at high q allows for the comparison between all different samples types and concentrations.

If not, how can the "aggregated" species be correlated to the crystallinity and/or crystal size of the P3HT domains?

As illustrated in Figure 3.16, P3HT has both crystalline and amorphous phases that are intermixed; however, because they are interspersed, there are chains that link the two phases together, which means that P3HT segments are not limited to just two conformational structures. These segments that are connected to crystals, but are not ordered on a crystal lattice have been identified as conformationally disordered crystals, also known as a condis crystal, where the structure permits liquid-like ordering while retaining orientational order [70]. Therefore, there are chain segments in crystals that are most ordered, segments that are in the amorphous phase that are the least ordered, and segments that link the two phases together that have an intermediate state of order. This intermediate amount of order will have a different conjugation length than that of the amorphous polymer or the crystalline polymer and may manifest itself as an "aggregated" species in Raman spectroscopy.

The highly ordered crystalline domains that form with annealing will alter the number and amount of these connecting chains that exist between the crystalline structure and the disordered amorphous domains. These relatively ordered segments might be reflected in the Raman spectra, i.e. as the "aggregated" species that reside between the crystalline structure and the amorphous segments. Just comparing the percent crystallinity area to the amount of aggregated species as denoted by the Raman results does not provide a physical structure to correlate to the spectroscopic result because the percent crystallinity correlates to the volume of

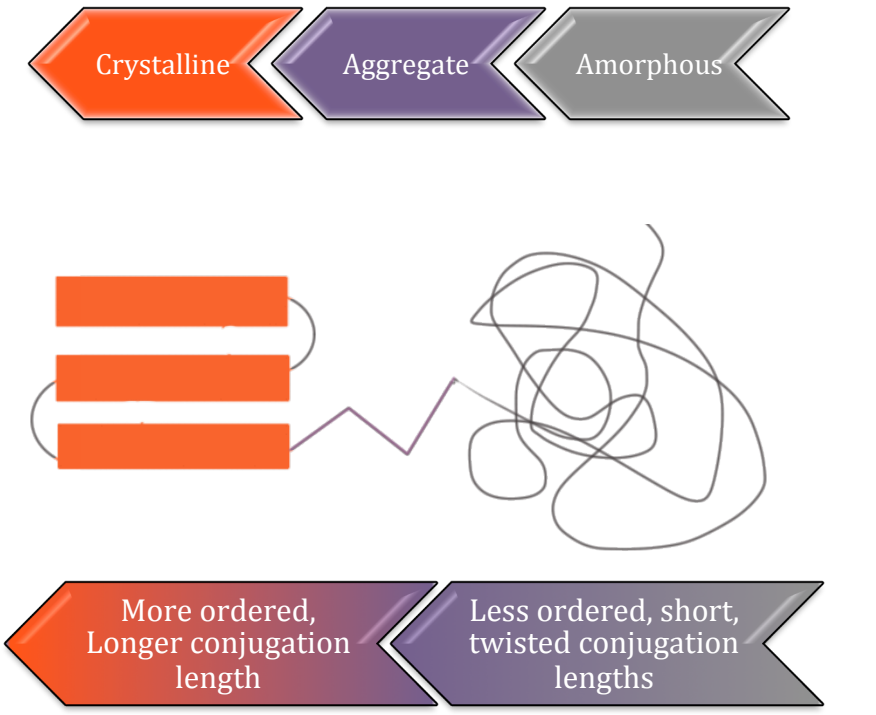

Figure 3.16. P3HT shows a difference in conjugation lengths and ordering from crystalline to aggregate, to amorphous structures.

the crystal. The amount of connecting chains between the crystal and amorphous phase correlate to the surface area of the crystal, rather than the volume of the crystal. Therefore, a qualitative term that is proportional to the surface area of crystalline structure is needed. This can be qualitatively realized by taking a measure of the volume of the crystal, such as the crystallinity, and dividing it by a measure of the size of the crystal (i.e. length), offering a measure of the surface area of the crystals ($A_{Surface}^{Crystalline}$) (Equation 3.6). This qualitative term gives a representation of the area of interface between the crystalline structures and the amorphous phase, which is where the conformationally disordered crystals reside.

$$Crystallinity/_{Crystal\ Size} = vol/_{length} = A_{Surface}^{Crystalline} \qquad (3.6)$$

If this measure of the crystalline surface area correlates to the amount of the "aggregated" phase that exists as monitored by Raman, this would be consistent with the interpretation that the Raman "aggregated" species is structurally correlated to the formation of chains that link the crystalline and amorphous phases. Figure 3.17 illustrates that an increase in crystal size corresponds to a decrease in the crystal surface area and the number of chains that link the crystal to the amorphous phase, where Figure 3.17 schematically illustrates the change in the crystal surface area with changes in the crystal size. Therefore, qualitatively, an increase in crystal size as measured with GIXRD should correspond with the decrease in amount of linking chains, which should correlate to a decrease in the amount of aggregated species as determined by

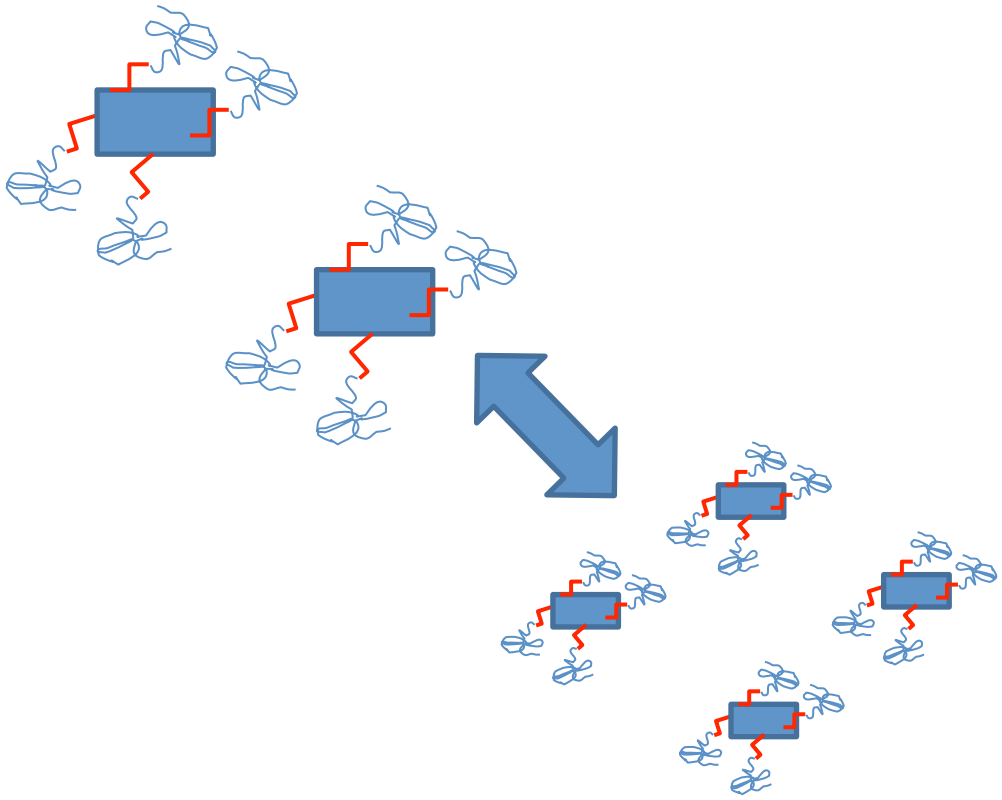

Figure 3.17 Visual representation of the surface area of the crystal where this "aggregated" species as the longer conjugated domains neighboring the crystalline domains followed by the shorter/twisted domains of the "unaggregated" species. Change in these species via the crystal surface area can be correlated to the spectroscopic response.

Raman, because larger crystal sizes would mean less connecting chains between the crystal and amorphous phase.

Therefore, if this interpretation is correct, the changes in crystal surface area should correlate to the changes in percent aggregation as measured by Raman for a variety of sample preparation conditions.

3.4.2 Understanding Ordering in Neat P3HT Thin Films

As always, an understanding of the most basic conditions is needed to build from, therefore the order of P3HT in its neat films is first determined via Raman spectroscopy. Literature reports that P3HT forms more crystalline domains with thermal annealing [63], but can this ordering process help us to understand the structural correlation of the longer conjugation length, "aggregated" species that are found with Raman spectroscopy?

Changes in the crystallinity of neat P3HT can be monitored by examining the intensity of the (100) peak in the GIXRD spectra. As seen in Figure 3.18, the peak intensity increases and full width half maximum changes as the P3HT molecules pack into crystals and become more ordered with thermal annealing. Figures 3.19 a-b show that the crystallinity and crystal size of the neat P3HT thin films both increase with thermal annealing, while Figure 3.19 d demonstrates the change in percent aggregation derived from the corresponding Raman spectra. Figure 3.19 c shows our new term, which is proportional to the crystalline surface area, to evaluate how this term correlates to the GIXRD and Raman results. Initial inspection suggests that percent aggregation as measured by Raman spectroscopy correlates much better to the surface area of the crystal than it does to the percent

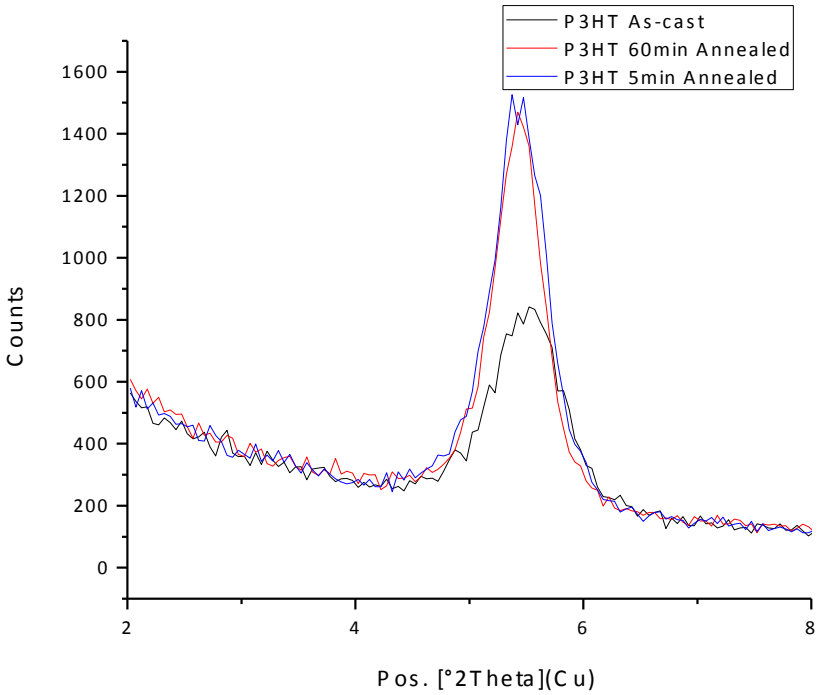

Figure 3.18. GIXRD of P3HT neat thin films, exhibiting changes in the full width half maximum and peak intensity with annealing.

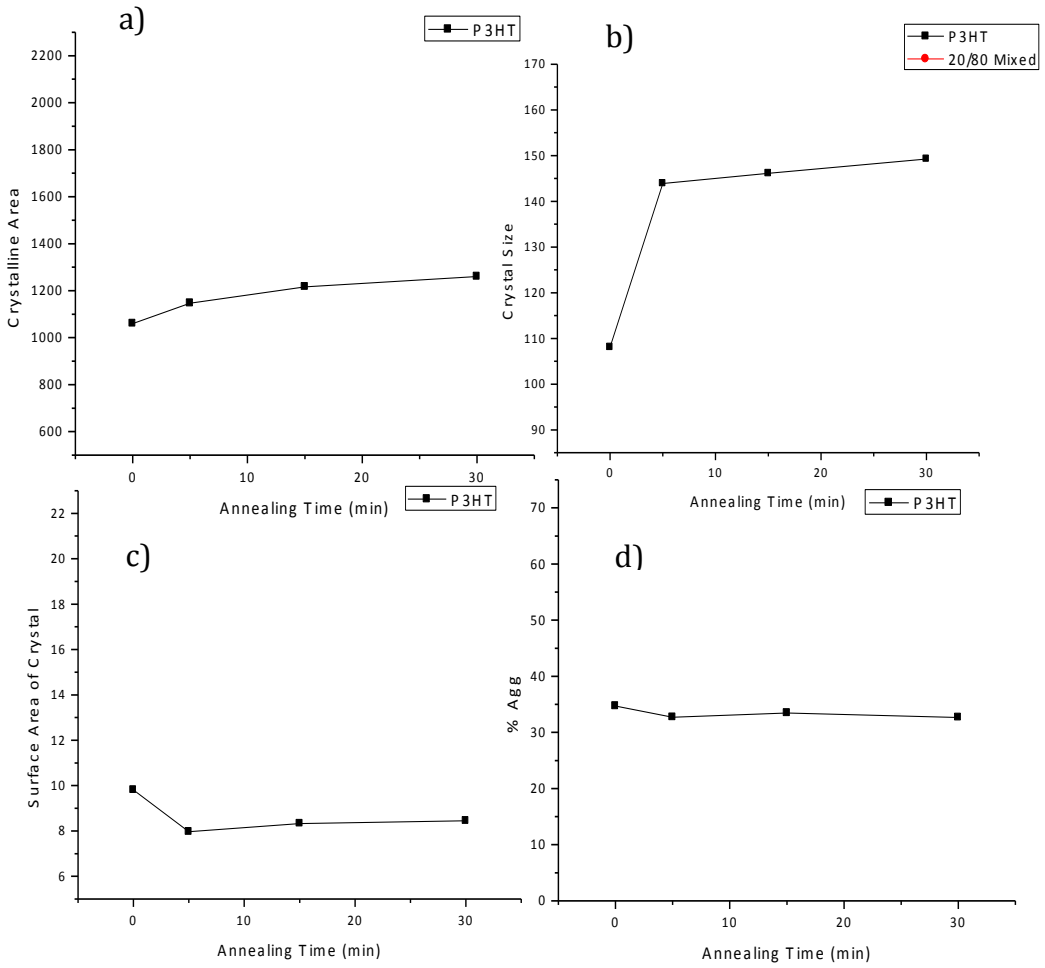

Figure 3.19 Neat monolayer of P3HT. a) shows the increase in overall area crystalline with annealing time. b) As expected with exposure to thermal annealing the size of the average crystal makes a dramatic initial jump then begins to level off. c) As the crystal size grows then plateaus, we see the surface area of crystal decrease and plateau off. d) Then in good correspondence with the surface area results the amount of aggregation shows a slight decrease.

crystallinity.

To test this correlation further and understand the impact of PCBM on the ordering of P3HT, the impact of thermal annealing on the ordering of P3HT in a neat monolayer is first monitored. It is well documented in literature, that with exposure to heat, P3HT crystalizes further. This is supported by our results in Figure 3.19. A slight increase in crystallinity is seen, as well as a dramatic initial jump in crystal size, which plateaus at longer annealing times. The crystalline surface area corresponds well with this as seen in Figure 3.19c; mirroring the jump in crystal size with a decrease then leveling off. With this decrease in surface area, a good correlation to a slight decrease in the amount of aggregation is seen. Thus, this detailed analysis of the P3HT neat monolayer provides a good baseline to monitor how the addition of PCBM alters the P3HT ordering by documenting deviations from the behavior of the neat P3HT thin film upon incorporating PCBM.

Therefore, the ordering of the P3HT in the presence of PCBM in a miscible system is investigated. For instance, Figure 3.20 shows the results of examining the 20/80 P3HT/PCBM mixed thin film. The change in crystallinity and crystal size with annealing as determined by GIXRD are shown in Figure 3.20 a-b, the change in crystalline surface area is presented in figure 3.18 c, and the Raman spectra "aggregation" is displayed in Figure 3.20 d. A quick glance comparing the structure of the neat monolayer to that of the mixed thin film reveals a distinct change in P3HT crystallinity due to the presence of the PCBM in the mixed layer, but surprisingly little change in the three other terms.

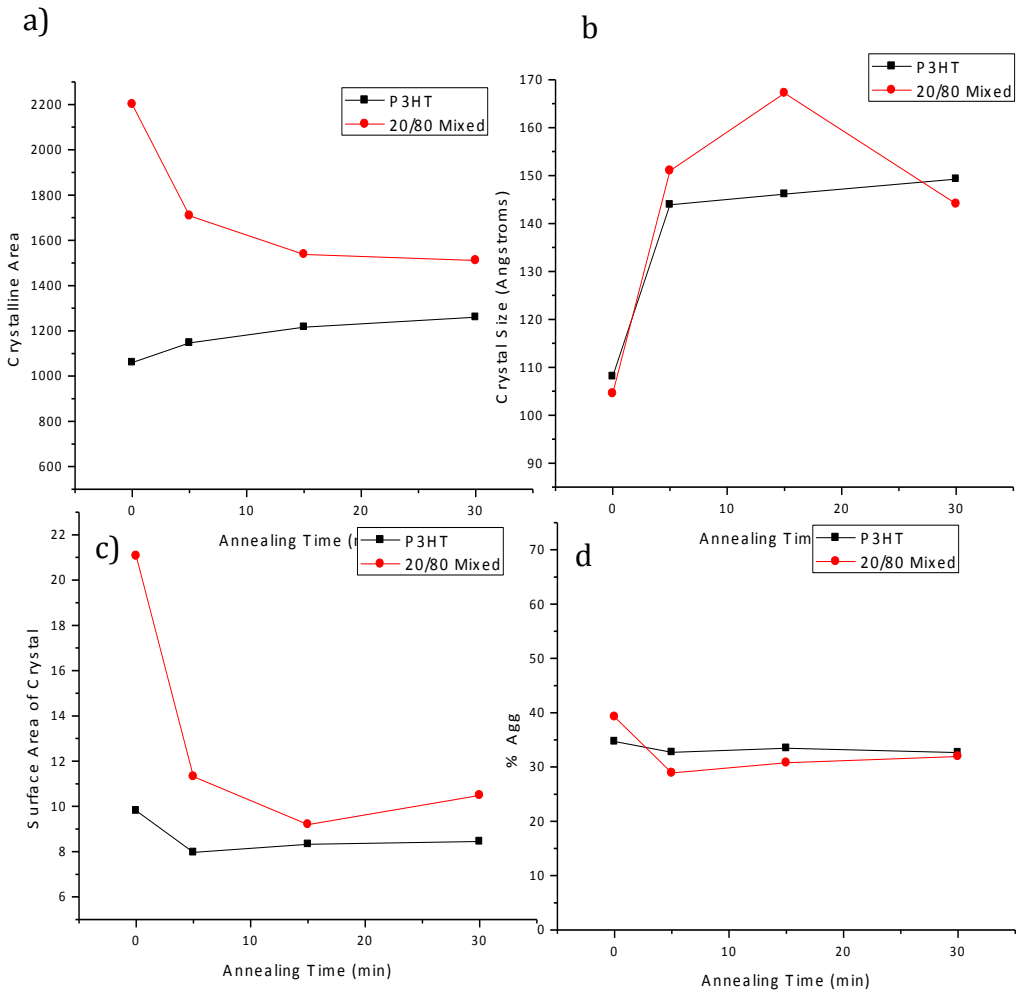

Figure 3.20 20/80 PCBM/P3HT mixed thin films. a) Miscible PCBM nucleates crystal growth then begins to act as a solvent decreasing the crystallinity. b) As PCBM dissolves smaller crystals the overall average crystal size increase, until at longer annealing times when PCBM begins to erode even larger crystal structures. c) Higher crystalline area yields a larger amount of initial surface area, quickly followed by a dramatic decrease as the crystal size increases. d) Again the aggregated species is following in behind the decrease in surface area of crystal.

3.4.3 PCBM/P3HT 20/80 Mixed Thin Films

The deviation of the P3HT crystallinity in the 20/80 mixed film from that of a neat P3HT thin film is therefore examined. Recent results from our group [55,71] and literature show that P3HT and PCBM have significant miscibility. In fact, PCBM is miscible to ~22 percent in P3HT. Therefore, 20/80 PCBM/P3HT mixed thin film were examined in order to better understand how the ordering of the P3HT is influenced by the presence of PCBM that is thermodynamically mixed in the amorphous phase.

The impact of PCBM on the ordering of P3HT can be seen immediately. There is a dramatic spike in the amount P3HT crystallinity in the initial samples, however with increased annealing the crystallinity decreases significantly. Initially, the miscible PCBM appears to nucleate crystal growth, but then with annealing the results indicate that the PCBM begins to act as a solvent for the smaller P3HT crystals. This explains the increase in the crystal size and a decrease in crystallinity with annealing. At longer annealing times, it appears that the PCBM begins to disrupt the order of the larger P3HT crystalline domains, as seen by the decrease in crystal size after 30 minutes annealing times. The higher crystallinity and smaller average crystal size results in a larger amount of crystalline surface area than that which was observed in the neat P3HT films, as observed in Figure 3.20c. Moreover, as the crystal size of the P3HT increases, the crystalline surface area decreases. With this decrease in surface area, there is a commensurate decrease in the amount of aggregated species as monitored by Raman, further corroborating the hypothesis that the "aggregated" species that is monitored by Raman is related to the amount of

connecting chains between the P3HT crystal and the amorphous phase. With the incorporation of PCBM in the miscible regime, the P3HT forms larger crystals than are formed in the neat P3HT. This appears to be influenced by PCBM's role as a plasticizer in the amorphous phase; allowing P3HT to form larger crystalline domains. The role of PCBM as a plasticizer was further confirmed by Tg measurements using DSC. The incorporation of a plasticizer results in more chain flexibility, therefore lowering the Tg of that polymer [72].

3.5 Conclusions

In this chapter, a fundamental correlation between P3HT's ability to order and pack with its efficiency to dissociate an exciton was analyzed. It was also discovered that by introducing PCBM into the system, more interfacial area between the PCBM and P3HT is created, which allows for better exciton dissociation than in the neat P3HT. The dissociation of the exciton appears to be dependent on both the ordering of the P3HT and the amount of PCBM that is dispersed in the P3HT amorphous phase. The crystalline domains can't be too big, such that the excitons recombine before reaching an interface, and there has to be sufficient amorphous P3HT to allow for effective intermixing of the PCBM and P3HT to create a plethora of interfaces for exciton dissociation.

In attempting to understand the role of PCBM's presence plays on the ordering of P3HT, it became obvious that the "aggregated" species as monitored by Raman spectroscopy does not correlate well to the amount of crystalline P3HT that exists in the sample. Further analysis led to the hypothesis that this "aggregated" species correlates to the amount of P3HT chains that link the crystalline phase to the

amorphous phase, which should scale with the surface area of the crystal. Further analysis of the crystalline structure and Raman spectra of neat P3HT films and P3HT/PCBM miscible films clearly show that there is a strong correlation between the amount of "aggregated" species as determined from Raman, and the amount of crystalline surface area. This corroborates the interpretation that the "aggregated" species as monitored by Raman correspond to the amount of polymer chains that link the crystal to the amorphous phase, which are also known as condis crystals.

A more detailed comparison of the crystalline structure and local ordering of P3HT in miscible P3HT/PCBM thin films shows that the PCBM appears to act as a plasticizer in the P3HT, causing a decrease in the amount of P3HT crystallinity and an increase in crystal size, which is interpreted to indicate that the diffusion of the PCBM in the amorphous P3HT phase erodes the smaller crystalline domains. These changes in crystal size and crystallinity, result in decrease of the "aggregate" species, yet this sample still showed good exciton dissociation abilities.

Chapter 4

Examining the Ordering of P3HT in P3HT/PCBM "Bilayer" Systems

4.1 Introduction

The studies of mixed layers of P3HT and PCBM indicate that PCBM acts as a plasticizer of the P3HT, altering the percent crystallinity and the size of the crystalline domains of the P3HT/PCBM thin films. However, depositing films from a mixed solution limits the control of the ordering of the P3HT and the morphology of the films that is available. Recent work by Schwartz and Lee [47,52], among others, have shown that the consecutive deposition of P3HT and PCBM layers to ostensibly form a bilayer is a feasible fabrication process for P3HT/PCBM active layers in OPV devices. This fabrication procedure opens additional pathways to independently control the P3HT ordering and the morphology of the mixture. For instance, by depositing the P3HT layer first and annealing before depositing a PCBM layer provides a method to control the crystallization of the P3HT layer independent of it mixing with PCBM, providing provide an additional level of control in directing the morphology of the active layers.

The use of orthogonal solvents for P3HT and PCBM allows for the sequential deposition of two layers onto the substrate. Based on the work of Lee et al [52], it is clear that this fabrication process does not create two pure layers with a sharp interface, but rather form a stack that consists of a P3HT rich under a PCBM rich layer.

Raman spectroscopy and GIXRD are used to establish an understanding of how the presence of PCBM alters the ordering of the P3HT in these "bilayers", where the ordering of the P3HT before PCBM deposition is tunable. The independent ordering of the P3HT potentially creates pathways to new and interesting morphologies. In this chapter, the change in the ordering of P3HT in these bilayers are contrasted to the ordering of P3HT in pure P3HT films and mixed P3HT:PCBM layers to document how specific fabrication procedures impact the bulk heterojunction morphology and P3HT ordering.

4.2 Experimental

Active layer materials were purchased and use as received, P3HT from Rieke Metals and PCBM from Nano-C. For bilayer deposition PCBM and P3HT were dissolved separately in DCM and ODCB, respectively, to allow for separate casting of the layers. Prior to casting, the solutions were allowed to dissolve for approximately 12 hours then heated to 55 °C for several hours before spin coating in order to achieve complete dispersion. Spin coating was carried out at 1000rpm for 90 seconds for the P3HT layer of the bilayer thin films. After spin casting of the P3HT layer onto Si wafer, the layer was allowed to dry for 20 minutes in a N_2 atmosphere. Freshly applied layers were allowed to crystallize at 150 °C in a vacuum oven at times ranging from 0 minutes to 30 minutes. After this annealing procedure, the PCBM in DCM was spun on top of the P3HT layer at 4000 rpm for 10 seconds, thus creating our "bilayer" samples.

Sample notation for the Raman spectroscopy and GIXRD bilayers may be a bit

more confusing than those of simple mixed layers. In the fabrication of the bilayers, an additional parameter is the thermal annealing of the P3HT layer at 150 °C prior to the deposition of the PCBM layer, which requires a slightly different notation to clarify what sample is being discussed.

In this chapter, the notation "as-cast" and "annealed" correlate to the annealing process of the overall bilayer, not the individual layers, as illustrated in Figure 4.1. Therefore, an annealed sample represents a sample that both P3HT and PCBM layers have been thermally annealed simultaneously. This is separate from the time that the P3HT monolayer is annealed at 150 °C prior to the deposition of the PCBM layer, which varies from 0, to 5, 15, or 30 minutes. For clarity, the change in all parameters are plotted as a function of the total time the P3HT layer was exposed to heat, which is equal to the P3HT crystallization time plus the "annealed" time.

4.3 Results and Discussion

4.3.2 Miscible System of 20/80 PCBM/P3HT Bilayers

The results in the previous chapter show that the PCBM has the ability to act as a plasticizer in the P3HT, limiting P3HT crystallization and interrupting the ordering of smaller crystals when the P3HT and PCBM are co-deposited into a mixed thin film. This brings up the question of whether PCBM can also behave as a plasticizer in the P3HT and PCBM are consecutively deposited. Fabricating the sample as this "bilayer" allows for the separate control of the thermal history, and therefore ordering, of each layer; providing an additional parameter that can be

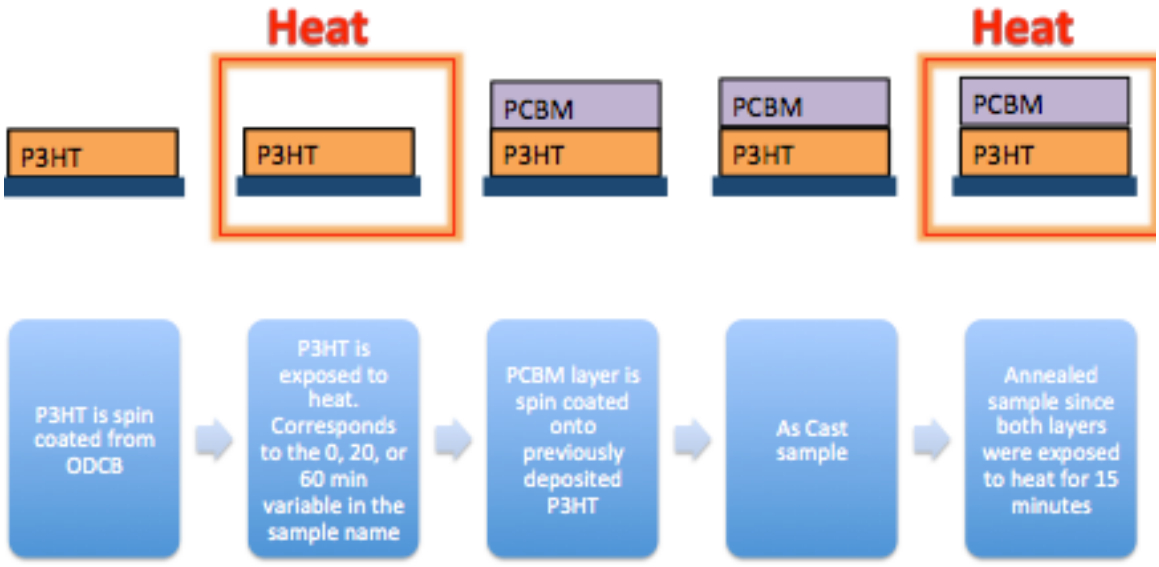

Figure 4.1. Step by step process of depositing the two layers and the heat exposure difference between as cast and annealed samples.

adjusted to tune the ordering and morphology of the final P3HT/PCBM mixed film. For instance, by thermally annealing the P3HT layer prior to depositing the PCBM layer, the ordering of P3HT in the absence of PCBM is promoted. But, what happens to the ordered P3HT that was formed during annealing when a PCBM layer is applied? The relative thicknesses of the P3HT and PCBM layers dictate the final composition of the layer after two layers mix, where the first sample examined is a 20/80 PCBM/P3HT bilayer, which will form a mixed layer that is miscible. Figure 4.2 shows the percent crystallinity (GIXRD), crystal size (GIXRD), crystal surface area (GIXRD), and percent aggregation (Raman) as a function of P3HT annealing time of the 20/80 PCBM/P3HT as-cast bilayer sample, the 20/80 PCBM/P3HT mixed layer sample, and the neat P3HT thin film. The thickness of the P3HT layer in the neat film and the 20/80 bilayer are the same to allow for direct comparison between the two.

Comparison of the crystallinity and P3HT ordering in the as-cast 20/80 bilayer and in the neat P3HT film provides direct evidence of the role of the deposition of PCBM layer onto the P3HT layer on the structure of the underlying P3HT layer. Figure 4.2 clearly shows that there is significantly larger amount of P3HT crystallinity than in the monolayer, presumably because there is penetration of the PCBM (and solvent) into the P3HT layer during deposition, which promotes the formation of smaller crystals. These smaller crystals translate into a higher crystal surface area, which correlates strongly to higher percent aggregation as determined by Raman spectroscopy. It is also worth noting that the decrease in

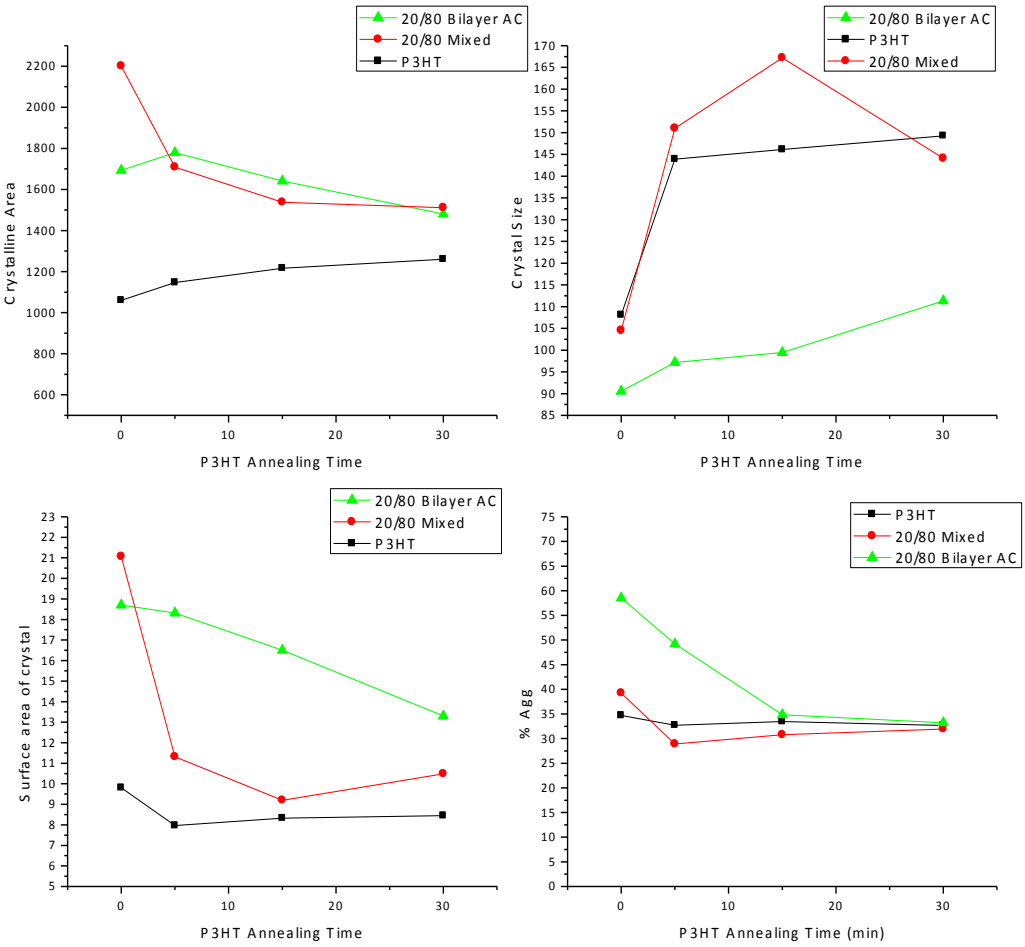

Figure 4.2 20/80 as cast bilayer thin films. a) Significantly larger area of crystallinity than seen in the monolayer. b) Smaller crystal formation promoted during spin coating. c) Crystalline area and crystal size result in the surface area decreasing with annealing. d) Percent aggregation decreases with surface area of crystal.

crystal surface area with thermal annealing follows closely the decrease in percent aggregation by Raman, further strengthening the structural correlation of the Raman determined percent aggregation to the chains that link the crystalline to the amorphous phase.

Further changes occur when the two separate layers are annealed simultaneously. According to previously reported neutron scattering results of Lee K. et al, thermal annealing of the PCBM rich/P3HT rich "bilayer" allows PCBM rich layer to diffuse into the P3HT rich layer [52], forming a single mixed layer, as depicted schematically in Figure 4.3. This procedure, therefore, allows us to determine the impact of the PCBM infiltration into the P3HT film on the ordering of the P3HT. The results reported in Chapter 3 indicate that the diffusion of PCBM in the mixed layer disrupts the ordering of P3HT, and it is interesting to determine if this is possible in these "bilayer" samples as well.

The change in the ordering of the P3HT with annealing of the bilayers relative to that to those that occur in a pure P3HT can also be observed in Figure 4.2. The annealing of P3HT prior to PCBM deposition is expected to improve the packing of the P3HT chains and form more robust crystalline domains [66]. During the annealing of the bilayer after PCBM deposition, PCBM is diffuses into the P3HT rich layer, containing these tightly packed, crystalline domains. The results in Chapter 3 indicate that the PCBM has the ability to disrupt P3HT crystalline domains, decreasing the percent crystallinity in the P3HT as these robust domains are broken up. Interestingly, the destruction of P3HT crystals with the infiltration of the PCBM into the pre-annealed P3HT layer during deposition is not observed. On the

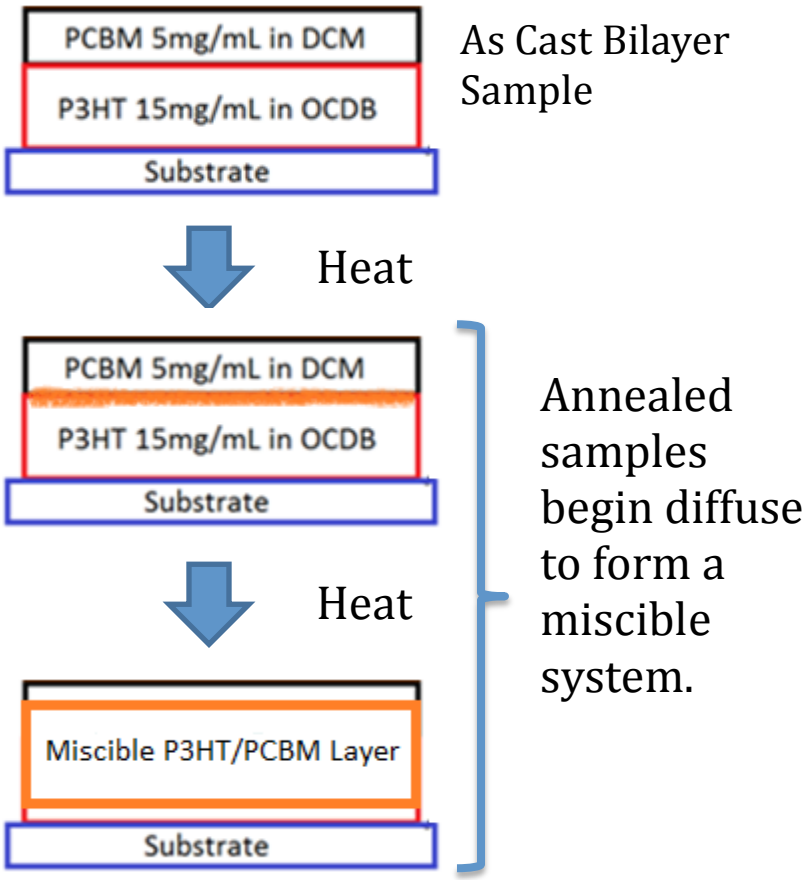

Figure 4.3. According to the work of Lee K. et al, with annealing the bilayer samples move from two separate rich layers to one miscible layer.

contrary, an increase in the size of the P3HT crystals is observed, with very little change in the percent crystallinity.

The discussion above examines the ordering of the P3HT in a miscible P3HT/PCBM sample that is formed from an initial "bilayer". However, these samples consist of separate P3HT-rich and PCBM-rich layers, but this examination does not address the impact of the thermally activated diffusion of PCBM into the P3HT-rich layer on the P3HT ordering. It is interesting to ask whether the control of the crystallinity of the P3HT layer before deposition of the PCBM layer alters the ability of PCBM to further impact the P3HT ordering. Inspection of Figure 4.2 allows us to make this comparison. As mentioned earlier, the thickness of the P3HT layer in the bilayer is the same as that of the P3HT neat monolayer, to allow direct comparison. Interestingly, Figure 4.2 shows that the ordering in the as-cast bilayers varies slightly from that of the neat P3HT monolayer. Figure 4.2 also shows a significantly larger percent crystallinity in the as-cast "bilayer" than in the pure P3HT monolayer. The "bilayer" sample also has significantly smaller crystal sizes than in the neat P3HT monolayer and mixed 20/80 thin film. Corresponding to this smaller crystal size, the crystalline surface area is also significantly higher than those reported in Chapter 3. Lastly, these changes correspond to a commensurate decrease in percent aggregation as determined from Raman. The as-cast "bilayer" sample has a higher amount of crystallinity, yet a significantly smaller crystal size than that of the comparable P3HT monolayer. This difference is attributed to the penetration of the solvent and PCBM into the P3HT layer during the deposition of the PCBM layer. It appears that the DCM swells the P3HT layer during PCBM deposition, which allows

for penetration of PCBM into the P3HT, creating a broad interface[47]. This penetration is apparently sufficient to promote the formation of small P3HT crystals, resulting in an overall higher crystallinity and smaller average crystal size in the as-cast "bilayers" than is observed in the neat P3HT monolayer. This larger amount of small crystals in the as-cast sample results in higher crystalline surface area. But with annealing of the P3HT layer before PCBM deposition, there is an increase of the crystal size, while the aggregation and crystalline surface area drop.

The promotion of smaller crystal formation is shown to be an additive effect of the solvent and PCBM during the deposition process by also examining the crystal size of the P3HT layer after spin coating just the solvent (DCM) on the P3HT film. Figure 4.4 shows the crystal size of the neat P3HT, the P3HT film that has had DCM spin coated on it, and the true bilayer sample. The results clearly indicate that spin coating the solvent by itself on the P3HT thin film decreases crystal size by about 20 Å, while spin-coating the PCBM and solvent on the P3HT thin film decreases the crystal size by 30-40 Å. This clearly shows that the alteration in the P3HT crystal size is a combination of both the solvent swelling during deposition and the PCBM diffusion into the P3HT layer.

With an understanding of the structure of the as-cast "bilayer" samples, the role of PCBM on the ordering of P3HT when the two layers are simultaneously annealed, allowing the PCBM to diffuse into the P3HT layer is of interest. Previously reported results clearly show that with annealing, the P3HT-rich layer and the PCBM-rich layer diffuse together into a single PCBM/P3HT layer if the amount of PCBM is less than ~ 20% of the sample[52]. Based on the results presented above, one

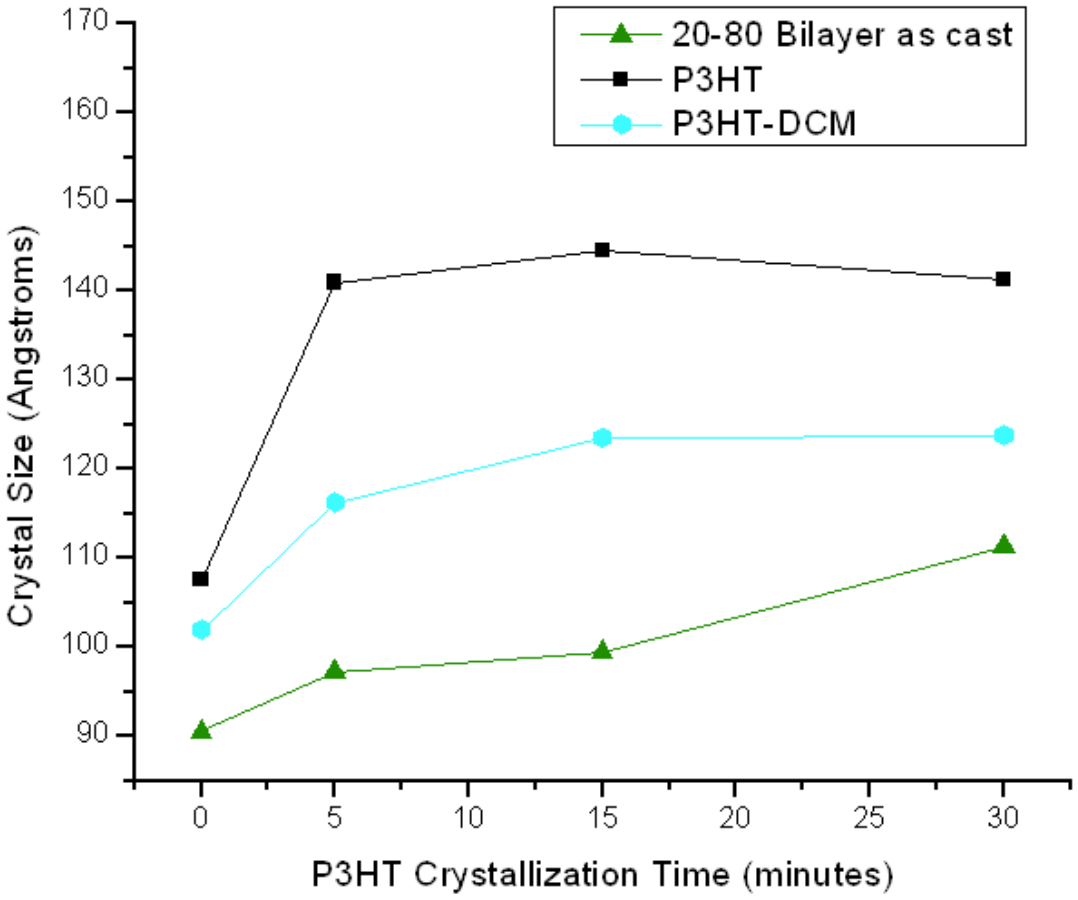

Figure 4.4 Combing affect of the solvent DCM and PCBM on the crystal size of P3HT formed during the deposition of the bilayer.

might expect that as PCBM diffuses into the P3HT layer, it may partially infiltrate the P3HT crystals, degrading the structure of the crystals, resulting in a decrease in P3HTcrystallinity. Figure 4.5 compares the percent crystallinity, crystal size, crystal surface area, and percent aggregation of the as-cast (AC) and annealed (AN) "bilayers". This figure shows that the ordering of the P3HT does not really change with the intermixing of the two layers; only a modest increase in the crystal size is observed. The percent crystallinity surprisingly does not change much at all with annealing. The modest change in crystal size may be attributed to the coarsening of smaller crystals during the annealing process. The surface area of the crystals in the annealed miscible "bilayer" correlates to the increase in crystal size of the initially annealed samples, then follows back in line with the trend of the as cast sample, almost as if its an extension of the trend line of the as-cast sample. Clearly, the diffusion of PCBM into the crystalized P3HT layer occurs without the destruction of the ordered P3HT domain, presumably allowing the PCBM to diffuse throughout the amorphous domains that exist in these films. In fact PCBM, appears to acts as a plasticizer for the smaller P3HT crystals formed during spin coating, allowing them to coarsen.

Thus, it appears that the fabrication procedure where the PCBM and P3HT layers to be deposited separately allows the P3HT to form a more robust structure than when cast in the presence of the PCBM; forming ordered P3HT domains that resist the penetration of PCBM into the layer.

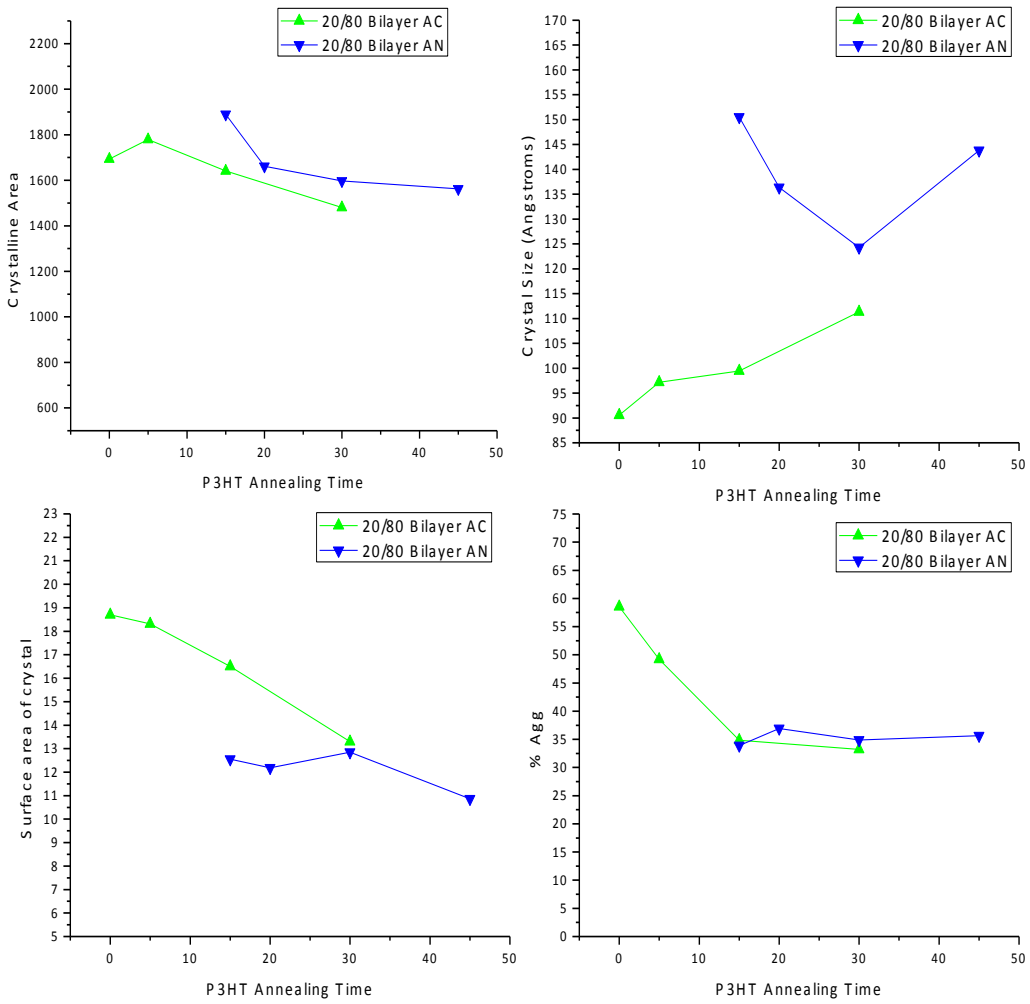

Figure 4.5 20/80 annealed bilayer thin films. a) Only a modest increase in crystallinity is observed. b) A slight difference in the crystal size due to the coursing of the crystals formed during the application of the PCBM layer. c) and d) Negligible affects of PCBM are observed.

4.3.3 Phase Segregated System of 40/60 PCBM/P3HT Bilayers

The 20/80 sample examined above achieves a final sample that is miscible, where all of the PCBM can infiltrate into the P3HT-rich layer upon annealing. However, most devices rely on the formation of a separate PCBM phase for electron transport, and thus the behavior of bilayers with higher PCBM loadings must be studied. With this in mind, a 40/60 PCBM/P3HT bilayer was examined, one that is expected to contain a separate PCBM phase after annealing.

Figure 4.6 shows the percent crystallinity, crystal size, crystal surface area, and percent aggregation as determined from Raman for the as-cast (AC) and annealed (AN) 40/60 PCBM/P3HT bilayer. The percent crystallinity increases steadily with annealing times, while the crystal size in these systems is significantly smaller than that of the neat P3HT or miscible P3HT/PCBM samples, yet the percent aggregation stays fairly constant with increased annealing times.

Inspection of Figures 4.6 a) and b) shows that the this phase segregated morphology results in a significantly smaller average crystal size than is found in the neat P3HT films, suggesting that the presence of the PCBM limits the P3HT crystallization. However, the ability of PCBM to penetrate the P3HT film and dissolve smaller P3HT crystals is not observed in these samples. Rather, it would appear PCBM helps nucleate small crystal growth resulting in a higher percent crystallinity than in the neat films. Also, this increase in the amount of smaller crystalline domains results in more surface area of the crystals that is commensurate with the amount of "aggregated" species in the sample.

Another surprising note, is that the phase segregated system follows closely

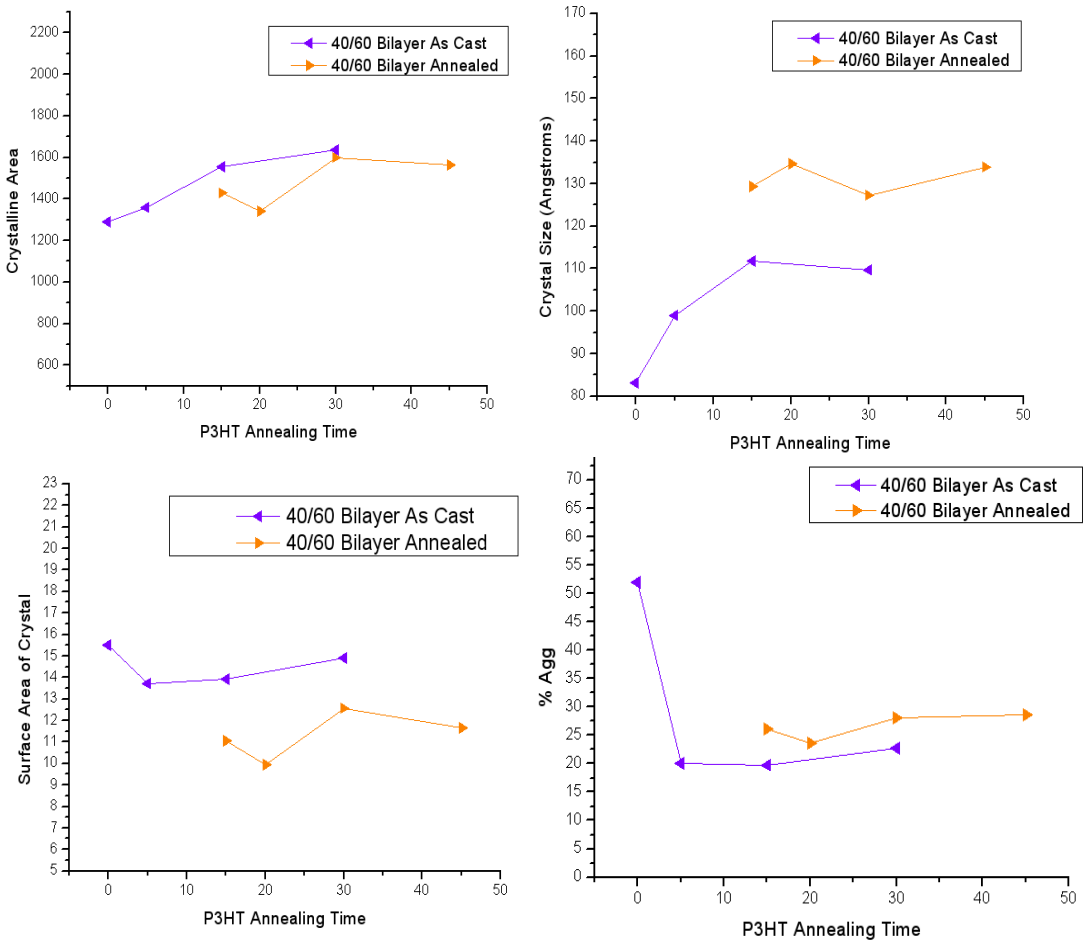

Figure 4.6. GIXRD and Raman results for 40/60 PCBM/P3HT bilayer samples. With longer annealing time the trends move similar to that seen in the miscible bilayer system.

the behavior of the miscible system, in that there is not a notable change in the P3HT crystallinity or aggregation during the annealing of the as-cast samples. It would appear that the phase-segregated system reaches an equilibrium state where PCBM is intermixed with the amorphous P3HT. The PCBM that is intermixed with the amorphous P3HT therefore appears to guide the crystallization behavior of the P3HT, forming a system with similar characteristics to those of the 20/80 bilayer.

4.4 Conclusions

The results in this chapter and Chapter 3 demonstrate that the ordering of the P3HT and, therefore the formation of P3HT crystals is influenced by the specific fabrication procedure and presence of PCBM. The examination of the P3HT/PCBM mixed layers shows that the presence of miscible PCBM in P3HT impedes P3HT crystallization, where PCBM can act like a solvent for smaller P3HT crystals. Investigation of the bilayers shows that the process of spin coating a separate PCBM layer on top of the P3HT thin film increases the ordering of the P3HT and promotes the formation of small P3HT crystals. The bilayer study also shows that annealing the P3HT layer prior to deposition of the PCBM creates more robust crystals that resist the intrusion of PCBM into the crystal, limiting its ability to disrupt the P3HT structure as the two layers migrate together to form one miscible layer. This would be consistent with the diffusion of the PCBM into the P3HT layer solely within the amorphous P3HT domains, leaving the robust crystalline domains intact.

These results therefore provide a foundation in which to controllably alter the ordering and mixing morphology in P3HT/PCBM bulk heterojunctions. These protocols can be used to create larger crystalline domains, which should improve

hole transport or create a system with smaller domains generating larger amounts of surface area for exciton dissociation. With this control, further studies can directly correlate these structural characteristics to OPV performance and provide guidelines towards improved photovoltaic devices.

Chapter 5

the Depth Profile of PCBM/P3HT "Bilayers" as Determined by Neutron Reflectivity and NEXAFS

5.1 Introduction

Neutron reflectivity (NR) provides a direct characterization of the depth profile of thin films and can therefore offer insight into the infiltration of PCBM into the P3HT layer of the "bilayer" samples that were examined in Chapter 4. NR provides information regarding the structure of the film normal to the surface and so is ideally suited to probe the detailed structure within a thin film provided suitable contrast can be designed into the system. In a protonated P3HT/PCBM film, there is sufficient neutron scattering contrast between components due to the higher density and lack of protons in PCBM, (it consists primarily of carbon), resulting in a greater scattering length density (SLD) than P3HT [73]. This difference provides ample contrast to probe depth profiles of the as-cast and annealed bilayers.

In the last chapter, the crystalline structure present in the P3HT thin films was examined by GIXRD. However, GIXRD only provides an average crystal structure in the film, but does not differentiate between crystals that are aligned parallel or perpendicular to the surface, which can have an impact on the active layer OPV performance. NEXAFS provides a mechanism to determine the orientation of the P3HT crystals near the surface, and is therefore used to elucidate the changes to crystal orientation that may occur during the annealing processes used to modify the BHJ morphology and the P3HT crystalline structure.

5.1.2 Probing of Active Layers with Neutron Reflectivity

There is limited contrast between the carbon-based conjugated polymer (donor) and carbon nanoparticle fullerene derivatives (acceptor) using electron-based techniques, leading to ambiguity in the determination of the morphology, depth profile, and mixing behavior of the P3HT/PCBM system by these methods. In particular, differentiating between an amorphous P3HT phase and an amorphous mixture of P3HT and PCBM is very difficult with these techniques. Similarly, AFM provides information only on the surface, which may not represent the bulk morphology. Therefore, there is a need to identify additional analytical techniques that are available to accurately characterize the morphology and depth profiles of conjugated polymer/fullerene mixtures.

Neutron scattering, however, provides sufficient contrast for this system because the scattering length density (SLD) of fullerene derivatives is significantly different from that of the protonated conjugated polymer and, hence, provides a method to determine much more detailed information on their structure, interfaces, and morphology.

5.1.3 NEXAFS

A crystalline lamella of P3HT is made of stacked polymer chains with their backbones aligned, with the direction of the alkyl side chains denoted as the ***a*** direction as shown in Figures 5.1a-c. In turn, the adjacent lamellae are stacked perpendicular to the parallel/co-facial conjugated backbones, which is denoted as the ***b*** direction, as shown in Figures 5.1a-c. In this schematic view, the π-stacking

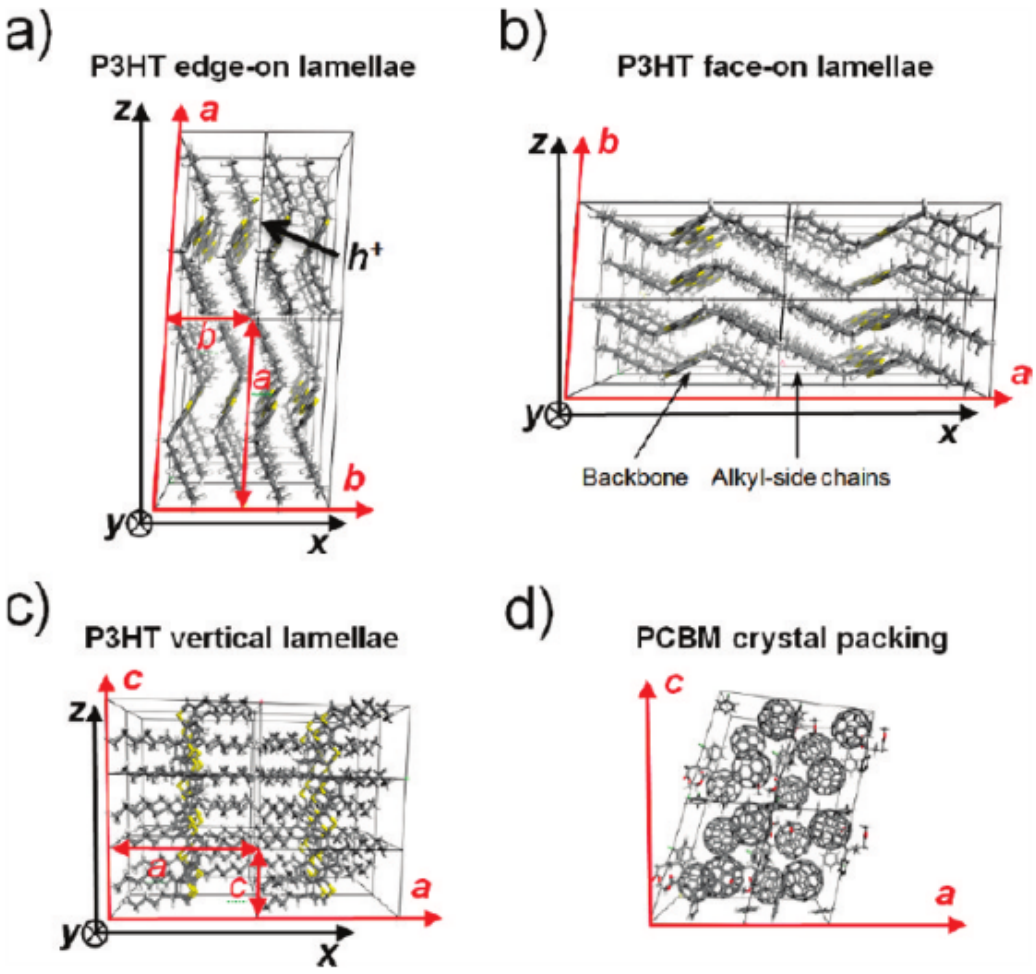

Figure 5.1. Illustration showing P3HT and PCBM crystal packing. The unit cells are enclosed by the boxes and are described by the lattice vectors a, b, and c. The P3HT alkyl- and π-stacking directions are along the a and b vectors, respectively. SiO_2 substrate coordinates are indicated with x, y, and z. Depending on the processing conditions, P3HT mainly self-organizes into (a) edge-on, (b) face-on, and (c) vertical lamellae (less likely).

direction is always orthogonal to the alkyl-stacking direction, but can be parallel to the sample substrate, denoted as a face-on orientation (Figure 5.1b). Alternatively, the π-stacking direction may be perpendicular to the substrate surface, an orientation known as 'edge-on' (Figure 5.1a). The vertical arrangement with the backbone perpendicular to the substrate, and both π–π stacking and alkyl-stacking directions prarallel to the substrate, is far less liekly (Figure 5.1c).

Processing conditions, solvents, polymer molecular weight, and substrate treatment can affect the orientation of the lamellae relative to the surface. This is important because the charge mobility in P3HT is highly anisotropic: hole (h+) charge mobility is greatest in the backbone direction, lower in the π-stacking direction where conduction occurs by hopping, and is negligible in the alkyl direction [74]. Furthermore, conduction can occur via mesoscale hopping through polymer chains bridges between crystalline domains. Thus, the transport of the hole from the polymer to the electrode surface in an OPV device occurs best in the vertical structure, where the P3HT backbone chains are perpendicular to the substrate, Figure 5.1c. [69]

5.2 Experimental

Samples for neutron reflectivity experiments were made with the same process and conditions as the bilayer samples that were studied in Chapter 4. However, as reflectivity requires a larger and thicker Si wafer for the substrate, the spin rates for each layer had to be adjusted to attain the targeted thicknesses. To provide a consistent coverage of the larger wafer, the spin rate was slowed; where

the spin rates required to achieve the same thicknesses of each layer were determined experimentally.

All reflectivity measurements were completed on the Liquids Reflectometer at the Spallation Neutron Source at Oak Ridge National Laboratory with a neutron wavelength varying from 2.75–5.75 Å and an effective q-range of 0.006–0.105 $Å^{-1}$ ($q = 4\pi/\lambda \sin\theta$, where λ is the neutron wavelength and θ is the scattering angle).

Layers and Motofit software were used to fit the reflectivity profiles with model scattering length density profiles in order to determine the depth distribution of components in the thin films.

Assuming Fickian diffusion, the time needed for a PCBM molecule to diffuse across the thickness of the film can be readily estimated. Using literature values for the diffusion coefficient of PCBM (2.5×10^{-14} m^2 s^{-1} at 140 °C), [75] the PCBM molecule will traverse a 1600 Å film (the thickest film studied) in less than a second. Thus, all samples measured had adequate time to readily reach equilibrium during the annealing processes examined[51].

Unfortunately, it is not possible to directly extract structural information of the scattering sample from the measured reflectivity. To circumvent this limitation, the reflectivity of a model scattering length density (SLD) depth profile is calculated and compared to the experimentally measured reflectivity. The reflectivity of the model depth profile is iteratively refined until the calculated and experimental reflectivity profiles match. With foreknowledge of the sample scattering

characteristics and suitable constraints imposed to maintain a physically realistic system, the fitting provides a result that accurately reflects the structure of the scattering sample. One constraint used in the fitting of these data includes a mass balance of the P3HT and PCBM in the sample. The depth profile of the spin-cast bilayers and subsequently annealed bilayers was modeled using 2–5 layers.

The SLD, thickness, and roughness of each layer were freely varied. A model is assumed to accurately reflect the structure of the sample when the model reflectivity profile converges with the experimental profile, where the quality of fit is gauged using χ^2 statistics described by Equation 5.1, and the mass balance of the model system is within 5% of the mass balance of the sample.

$$\chi = \sum R_{(q)calc} - R_{(q)exp}/R^2_{(q)exp} \tag{5.1}$$

In Equation 5.1, R(q)calc and R(q)exp are the calculated and experimental reflectivities. The SLD profile is then analyzed to obtain the concentration depth profile of each component in the system.

$$\Phi_{(z)PCBM} = \frac{SLD_{(z)} - SLD_{(P3HT)}}{SLD_{(PCBM)} - SLD_{(P3HT)}} \tag{5.2}$$

For instance, the PCBM concentration depth profile is determined using Equation 5.2, where $\phi\,(z)_{PCBM}$ is the volume fraction of PCBM at depth z, $SLD_{(z)}$ is the experimental scattering length density at depth z, and SLD_{P3HT} and SLD_{PCBM} are the SLD of P3HT and PCBM, respectively. In order to quantitatively analyze the

reflectivity curves, the accurate scattering length density (SLD) of each component is needed. The density of crystalline P3HT is taken as 1.12 g cm^{-3}, based on X-ray diffraction data [52] and the density of amorphous P3HT is estimated to be ~10% less than that of crystalline P3HT, 1.01 g cm^{-3}. Using these values, the scattering length densities of crystalline P3HT and amorphous P3HT are calculated to be 0.69 x 10^{-6} $Å^{-2}$ ($SLD_{P3HT,c}$) and 0.62 x 10^{-6} $Å^{-2}$ ($SLD_{P3HT,a}$) respectively. Since the exact amount of crystallinity isn't know in the samples SLD of P3HT can be based off of the work previously done in our lab. This recent work in our lab suggests that 20% crystallinity is a reasonable value, and thus a SLD of 0.64 x 10^{-6} $Å^{-2}$ is used for the P3HT phase in these bilayer samples. Given the proximity of $SLD_{P3HT,c}$ and $SLD_{P3HT,a}$, any error in this assumption will not significantly impact the results presented below. The density of crystalline PCBM is reported to be 1.67 g cm^{-3} for crystals formed from ODCB [53]. Following the assumption that amorphous PCBM is 10% less dense than crystalline PCBM, the SLD of amorphous PCBM is calculated from its density and composition to be 4.4 x 10^{-6} $Å^{-2}$ [54] which agrees with previous work and our fitting of the neutron reflectivity profile of a spin-cast PCBM monolayer [55].

Near edge X-ray absorption fine-structure spectroscopy was used to monitor the molecular orientation and composition of the P3HT/PCBM mixture near the surface. Measurements were taken on beamline U7A at the National Synchrotron Light Source (NSLS) at Brookhaven National Laboratory. The partial electron yield (PEY) signal was collected using a channeltron electron multiplier with an

adjustable entrance grid bias (EGB). A negative bias of 50 V was applied to prevent low-energy photoelectrons from reaching the detector. Signal at different angles were collected by rotating the sample holder with respect to the incident beam in the plane of incidence. The angle reported is the angle of the incident beam with respect to the substrate surface. The monochromator energy scale was calibrated using the C K-edge π* transition of graphite, located at 285.5 eV.

5.3 Neutron Reflectivity Profiles

Through fitting of neutron reflectivity profiles, the depth profile of the components normal to the film surface and the segregation of the components at the interfaces can be determined, which is crucial to the charge collection and transport processes. [76] Neutron reflectivity profiles are noted by their Kiessig fringes, where these fringes are directly related to the thickness and roughness of the layers. As seen in Figure 5.2, sharper interfaces are characterized by distinct peaks and as the roughness increases between the layers, these fringes smooth out [77].

Figure 5.3 and 5.6 show the neutron reflectivity profiles of the 20/80 PCBM/P3HT bilayer as-cast and annealed at 150 °C for 15 minutes samples respectively. These data are plotted as RQ^4 vs Q with χ^2 values less than 3, to accentuate the quality of the fit. The resulting scattering length density (SLD) profiles can be found in Figures 5.4 and 5.7, to visually represent the distribution of PCBM and P3HT throughout the thickness of the films.

Figure 5.3 shows the reflectivity of the 20/80 PCBM/P3HT 0 min film both as-cast and annealed at 150 °C for 15 minutes. Inspection of these curves clearly

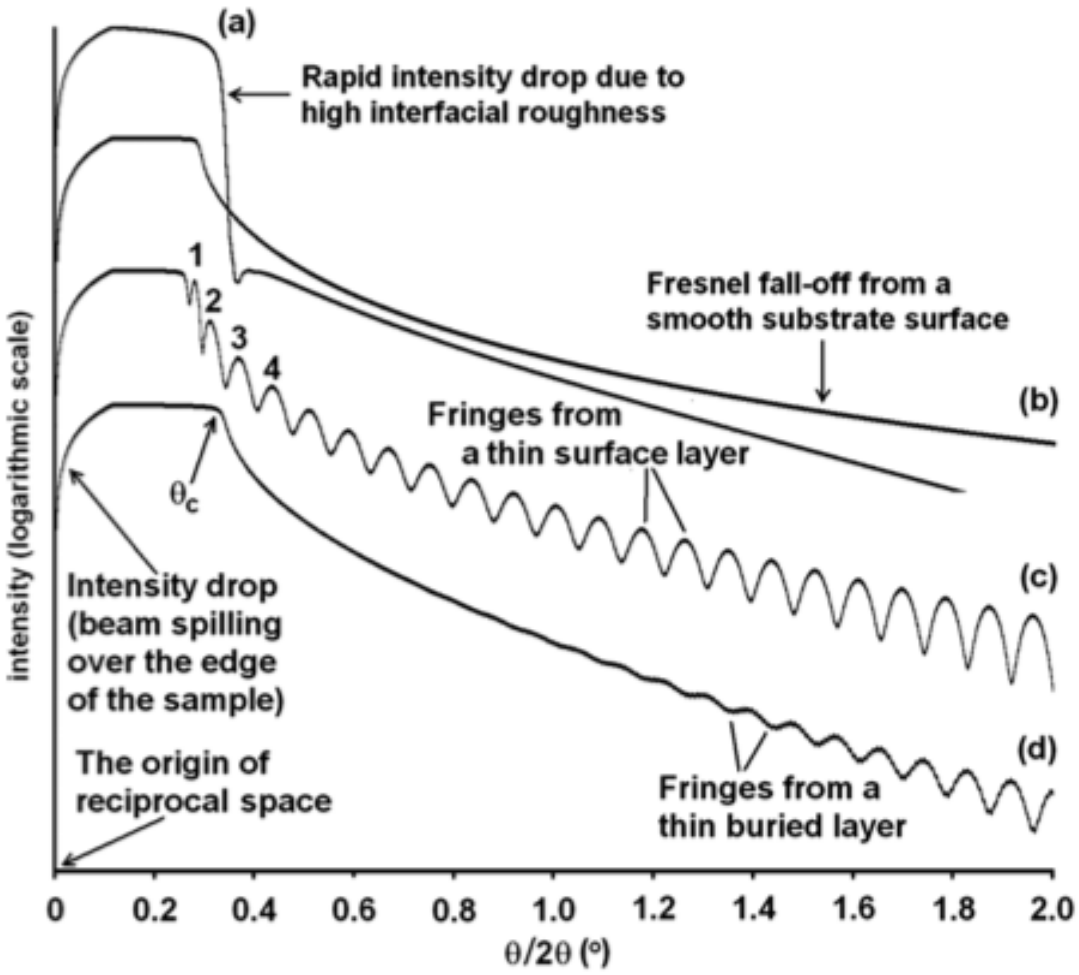

Figure 5.2. Kiessig fringes seen in neutron reflectivity profiles can be used to understand layers thickness and roughness. [73]

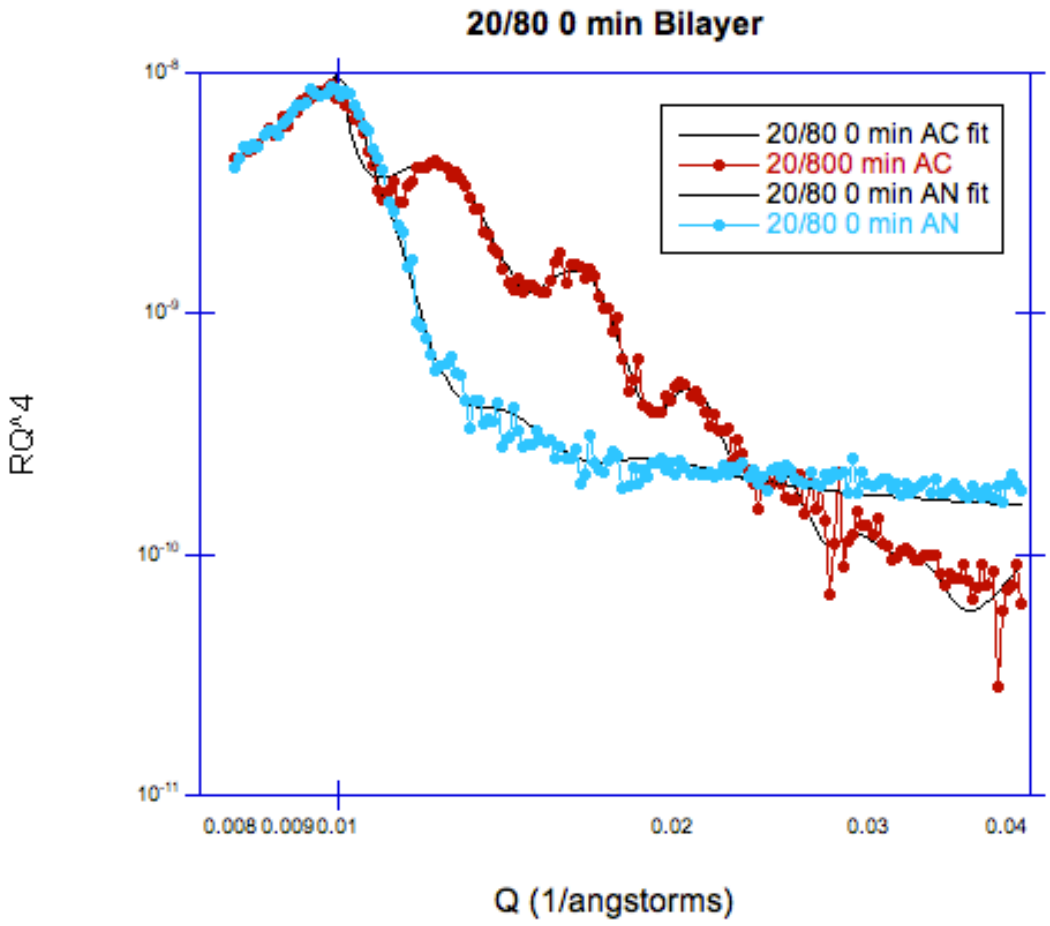

Figure 5.3 Reflectivity profiles and respective fits of 20/80 PCBM/P3HT bilayers show a lose of Kiessig fringes indicating a broadening of interfaces with annealing.

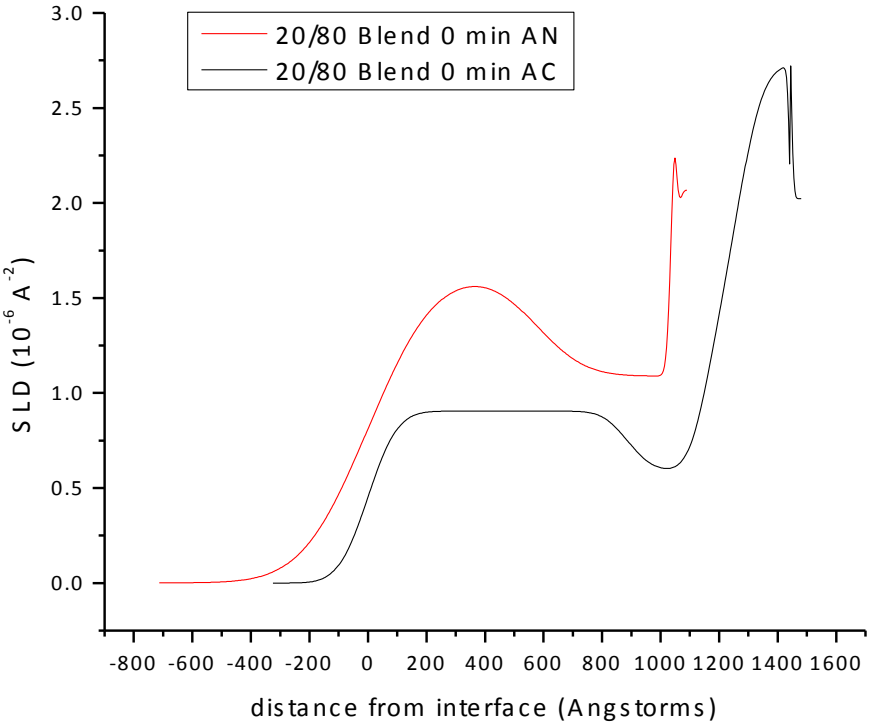

Figure 5.4 SLD profiles of 20/80 0 min as cast and annealed. Air/surface interface at z=0. Higher SLD in the annealed profiles exhibits the affect of PCBM distribution throughout the layer.

shows a change in the reflectivity with heating. Based on the loss of the Kiessig fringes, it is clear that the as-cast sample has sharper interfaces that broaden and disappear with annealing. This is indicated by the distinct sharp peaks in the as-cast reflectivity curve that disappear in the annealed reflectivity curve. This suggests that the two layers are diffusing together to form a single layer with annealing.

Recall that PCBM has a higher scattering length density than P3HT, and therefore, inspection of Figure 5.4, which is the SLD profile of the as-cast and annealed samples, shows that the PCBM penetrates the complete film during the deposition process and segregates to the substrate interface during the deposition process. This is shown by the very high SLD at the substrate indicating a mostly PCBM concentration. This excess PCBM at the substrate results in a depletion of PCBM from the area immediately above it, creating a P3HT rich layer with significantly lower SLD. Yet closer to the air/surface interface, a plateau region exists from ~200-700 Å, which is indicative of PCBM intermixed into the P3HT.

With annealing, the separate P3HT and PCBM rich layers blend together through the bulk of the thin film. The intermixing of the PCBM and P3HT results in a higher SLD throughout the entire layer. Also, there appears to be an excess of PCBM developing immediately below the air/surface interface at long annealing times.

The concentration profile of PCBM as a function of the thin film depth as presented in Figure 5.5 clearly shows the intermixing of PCBM and P3HT. The as-cast sample has an excess of PCBM at the silicon substrate. While guiding research suggested that a PCBM rich layer will form at the air/surface interface followed by a

P3HT rich layer at the substrate in these films during bilayer deposition [52], it is not surprising to find PCBM at the substrate. Literature reports suggest that the segregation of nanoparticles to the substrate is entropically favored due to a depletion attraction between the particles and the substrate [78]. It is interesting that it appears there is sufficient time during the drying of the spin-coated sample for the fullerene to migrate to the silicon substrate.

On comparing these results to those of Lee, a different depth profile is observed in our samples that what was reported previously. This difference may be attributed to a variation in drying conditions after the deposition of the P3HT. This exemplifies the importance of processing conditions on the resultant morphology. Lee dried the P3HT layer at 60 °C for 20 minutes before depositing the PCBM layer. However, our protocol allowed the P3HT layer to dry under a N_2 atmosphere for 20 minutes with no heat. It appears that the application of heat during the drying process allows for the creation of more P3HT crystals and removal of all solvent. Under these conditions, the PCBM is inhibited from penetrating into the P3HT layer by its extended crystalline structure. Thus, most PCBM remains at the top of the layer and a small amount penetrates the P3HT film. However, in this study, the samples are not heated during drying, which should result in a sample with fewer crystals and residual solvent. This would allow the PCBM to migrate through the P3HT film during the drying process, as the P3HT layer should be more fluid like.

Figure 5.5 shows that there exists a significantly large region of miscible P3HT/PCBM as a result of spin coating. As the sample is annealed, the PCBM rich

Figure 5.5. Volume fraction or concentration depth profiles calculated from the SLD profiles. Z = 0 is the air/surface interface while Z ~ 1000 Å denotes the Si substrate interface.

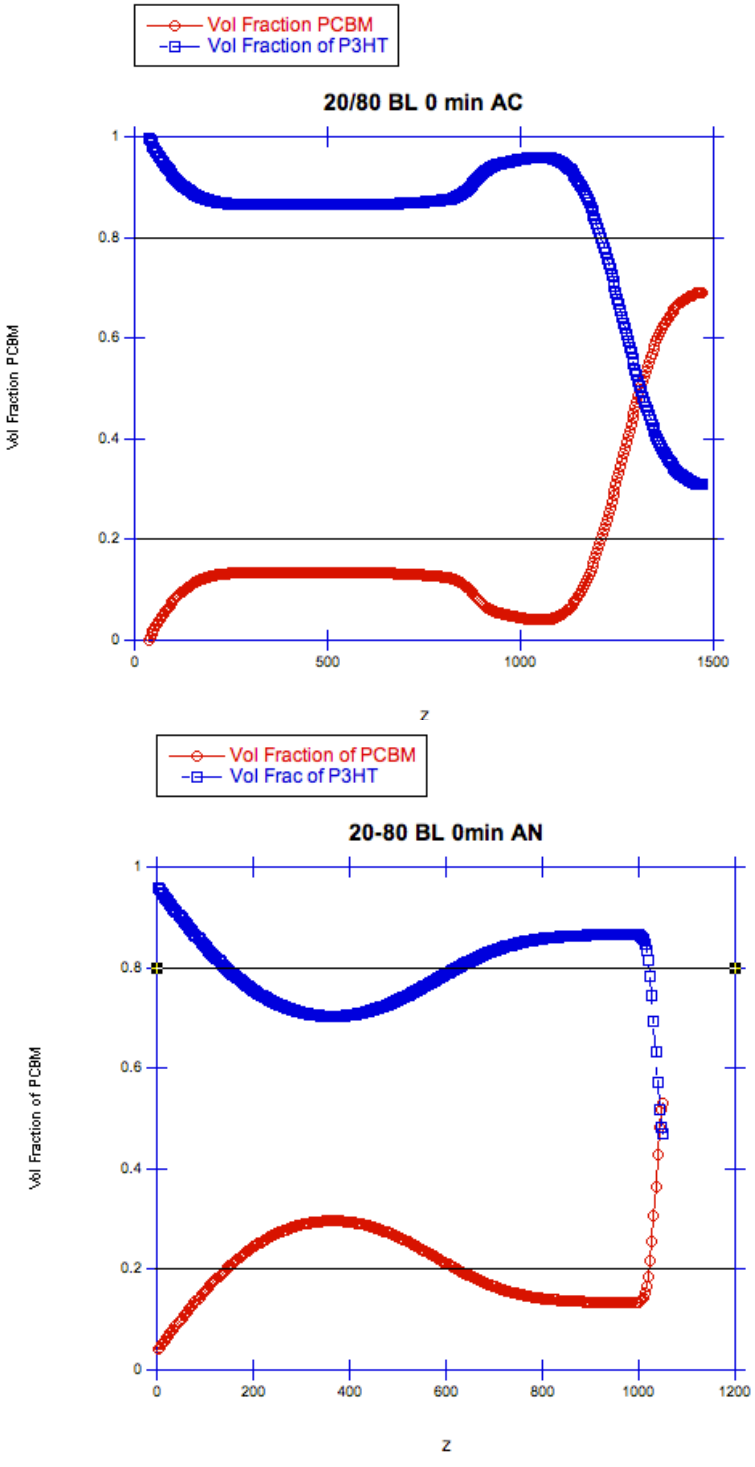

Figure 5.5 Continued

layer at the substrate disperses into the P3HT rich layer in the bulk of the film. This indicates that sufficient amorphous P3HT exists to allow the PCBM to mix, resulting in the PCBM loading remaining right around the miscibility limit throughout the film depth. A slight surface excess of P3HT at the air surface is due to its lower surface energy, which leads to a slight depletion of P3HT in the 200-600 Å depth, and a concomitant increase in P3HT loadings near the silicon surface (600-1000 Å). The PCBM depth profile mirrors that of the P3HT.

The neutron reflectivity of the 20/80 PCBM/P3HT bilayer system where the P3HT layer has been pre-exposed to heat for 60 minutes is shown in Figure 5.6. Similar to the sample where the P3HT was not heated before PCBM deposition, the loss of fringes in the NR profile with thermal annealing indicates a broadening of the interfaces that exist in the as-cast layer, suggesting that the PCBM redistributes throughout the film with annealing.

In Figure 5.7, the depth profile of the SLD of this 20/80 PCBM/P3HT bilayer is displayed. In the as-cast sample, there exists a significant segregation of PCBM to the substrate as indicated by the high SLD, which again indicates that the film morphology allows the PCBM to diffuse through the whole sample during the deposition of the PCBM on the P3HT layer. Unlike the previously discussed sample, the excess PCBM doesn't cause a neighboring depletion layer. Rather, there is a significant excess of P3HT at the air interface under which a bulk layer exists that consists of a PCBM/P3HT mixture whose composition is very close to that of the 20/80 overall composition of the film. This indicates that the consecutive deposition

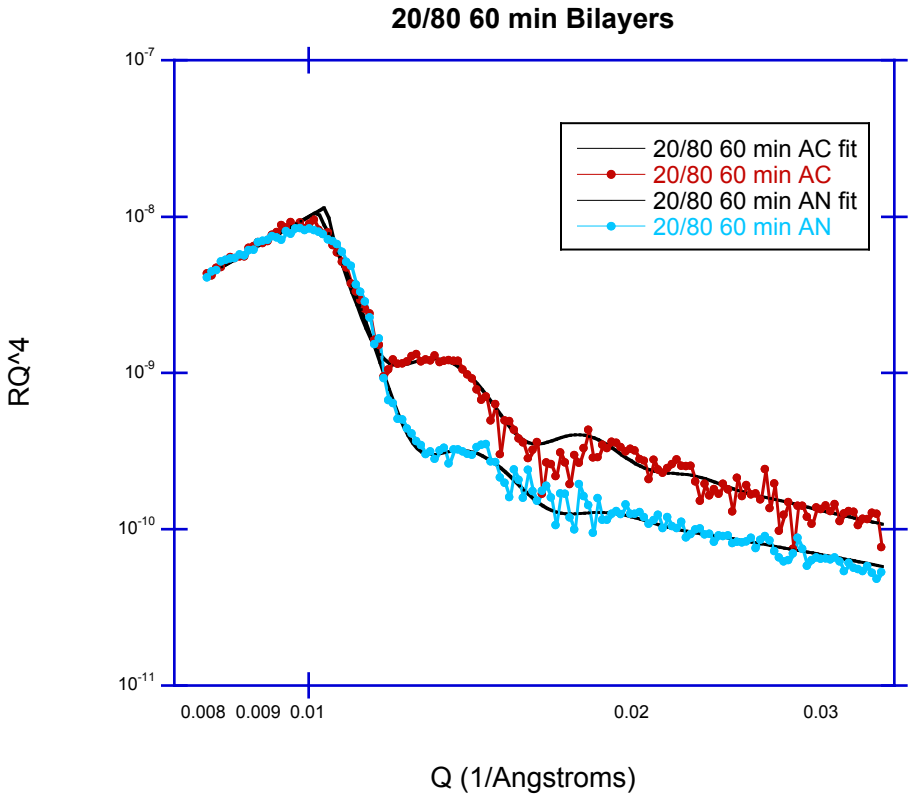

Figure 5.6 Reflectivity profiles with fits of 20/80 60 min bilayer as cast and annealed. Annealing shows slightly less changes in profiles than those of the 0 minute bilayers.

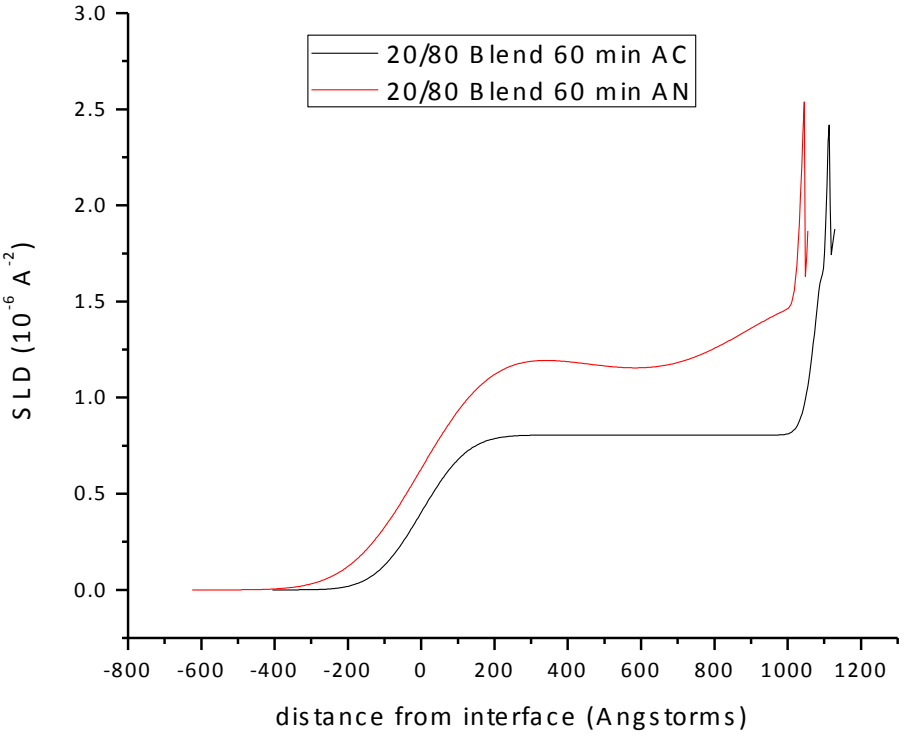

Figure 5.7 SLD profiles of 20/80 60 min as cast and annealed. The air/surface interface is at Z=0.

of the P3HT and PCBM results in a fairly mixed layer if the P3HT is crystallized first. When this sample is further annealed at 150 °C for 15 minutes, the PCBM and P3HT distribute throughout the film.

Figure 5.8 depicts the concentration depth profile of the 20/80 bilayer where the P3HT layer has been annealed for 60 minutes before depositing the PCBM. These longer P3HT crystallization times yield films that change less with annealing. The bulk of the as-cast film shows a nearly constant depth profile that is 80/20 P3HT/PCBM, with slight excesses at both the air and silicon interfaces. It is also clear that the concentration profile of the PCBM and P3HT in the P3HT 60 min sample does not vary much with further annealing, implying that the incursion of PCBM into the P3HT layer does not modify that layer. Therefore, for this 20/80 sample, the results indicate that with annealing at 150 °C, the PCBM that is segregated to the silicon surface redistributes through the film evenly. This results in the slight excess of PCBM just below the air/surface interface. This process is limited by the increase in the crystallinity of the bottom P3HT layer that grows with annealing before PCBM deposition.

Comparing Figures 5.5 and 5.8 shows that less PCBM is able to redistribute through the 60 minute film because of the barrier properties of the P3HT crystals. In all of the systems, the deposition process distributes PCBM throughout the whole layer, with PCBM aggregating at the silicon surface for all as-cast samples. The higher surface energy for P3HT causes PCBM to migrate and form an excess layer at the substrate interface. However, as crystallization time of the P3HT layer before

Figure 5.8. Volume fraction or concentration depth profiles calculated from the SLD profiles. Z = 0 is the air/surface interface while Z ~ 1100 Å denotes the Si substrate interface.

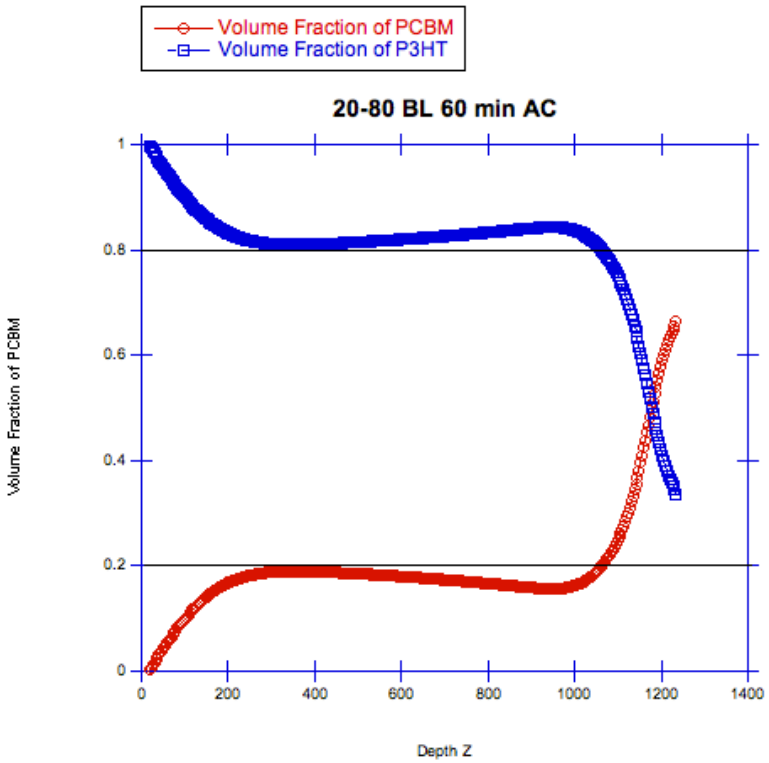

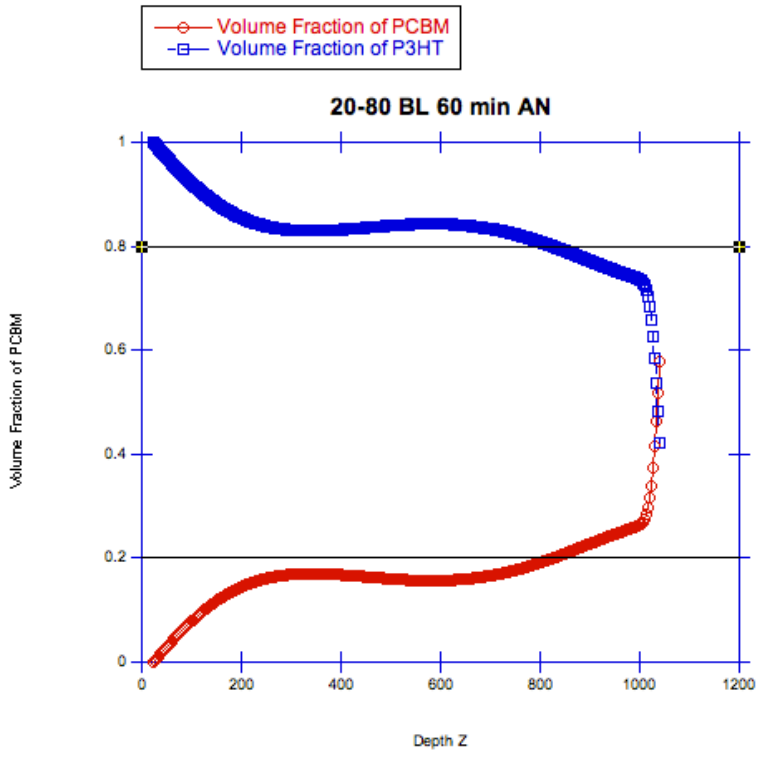

Figure 5.8 Continued

deposition of the PCBM is increased, the amount of PCBM that migrates to the silicon surface decreases substantially. The P3HT that is not annealed before PCBM deposition has a very distinct layer of PCBM at the silicon substrate, where the amount of crystallinity in this P3HT layer is relatively small. With an increase in the P3HT crystallization prior to PCBM deposition, the amount of PCBM that can migrate through this layer to the surface decreases. This makes sense, as the P3HT is exposed to heat, order and crystallization is promoted, and these ordered domains block and limit the pathways for PCBM to diffuse to the silicon surface during the deposition process.

The reflectivity curves of the 40/60 bilayer sample, which is in the phase segregated regime, are shown in Figure 5.9. Figure 5.10 shows the SLD profile of the 40/60 PCBM/P3HT sample where the P3HT is not annealed prior to the deposition of PCBM for both the as-cast and annealed samples. At a quick glance, the Kiessig fringes are not nearly as distinct as in the 20/80 bilayer samples, indicating that this phase segregated system contains more roughness and broader interfaces. [79] Also of interest is that in all of the 20/80 bilayer samples the thickness of the total film decreases with annealing, however in the 40/60 bilayers the total film thickens with annealing. This is attributed to the slight change in the percent crystallinity of the P3HT with annealing. In the 20/80 bilayers, a slight decrease in the P3HT crystallinity was observed with annealing, however in the 40/60 bilayers there is a slight increase in in crystallinity with annealing.

Figure 5.11 shows the corresponding concentration depth profiles that are

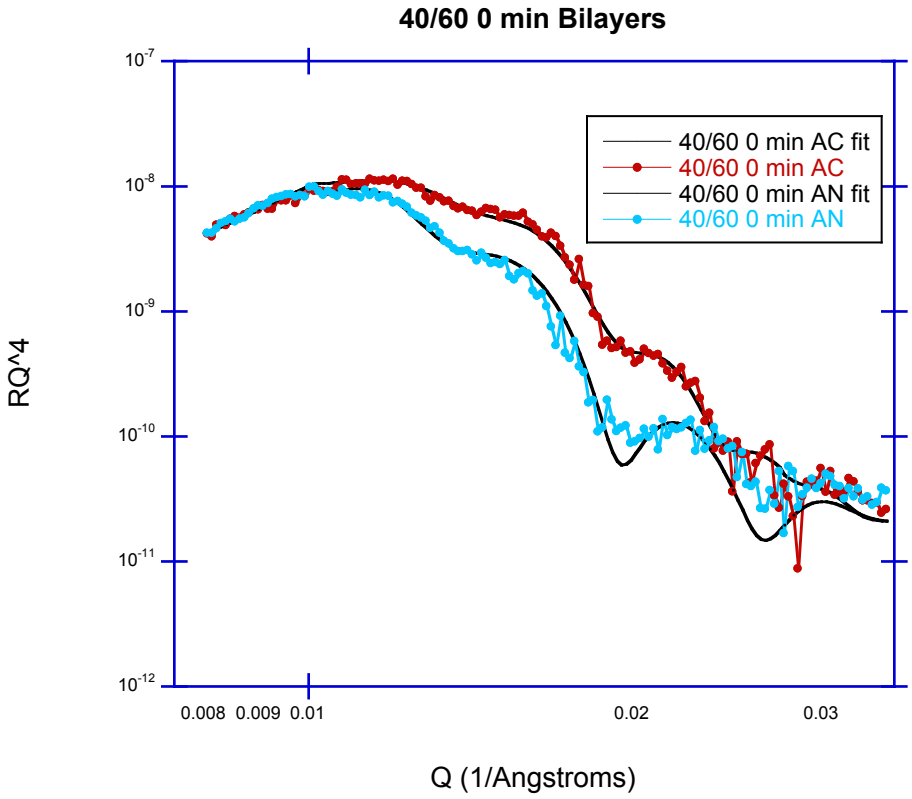

Figure 5.9 Reflectivity profiles with fits of 40/60 0 min bilayer as cast and annealed.

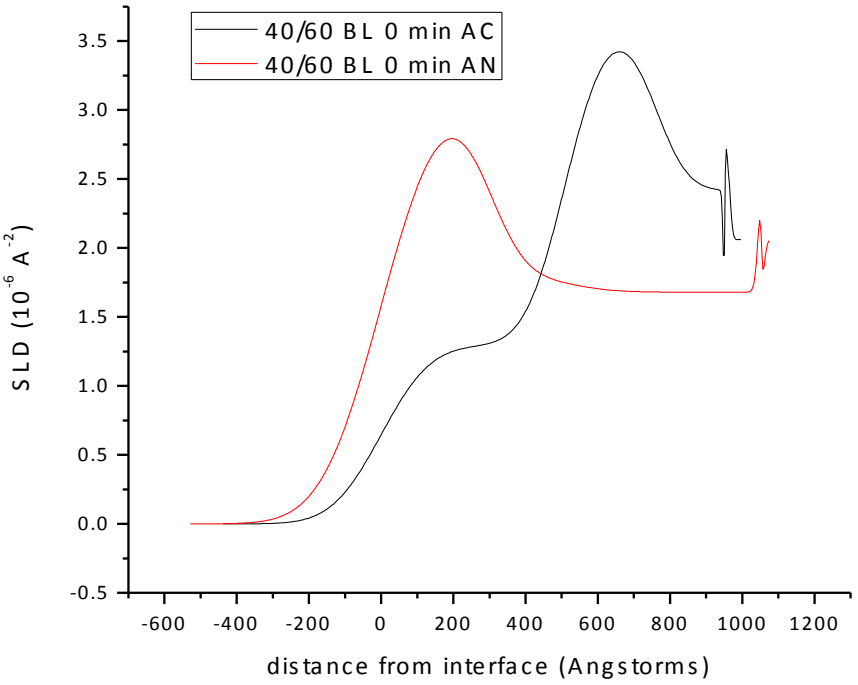

Figure 5.10 SLD profiles of 40/60 0 min as cast and annealed. Air/surface interface at Z=0. Changes in SLD indicate the redistribution of PCBM away from the substrate with annealing.

Figure 5.11. Volume fraction or concentration depth profiles calculated from the SLD profiles. Z = 0 is the air/surface interface while Z ~ 1100 Å denotes the Si substrate interface.

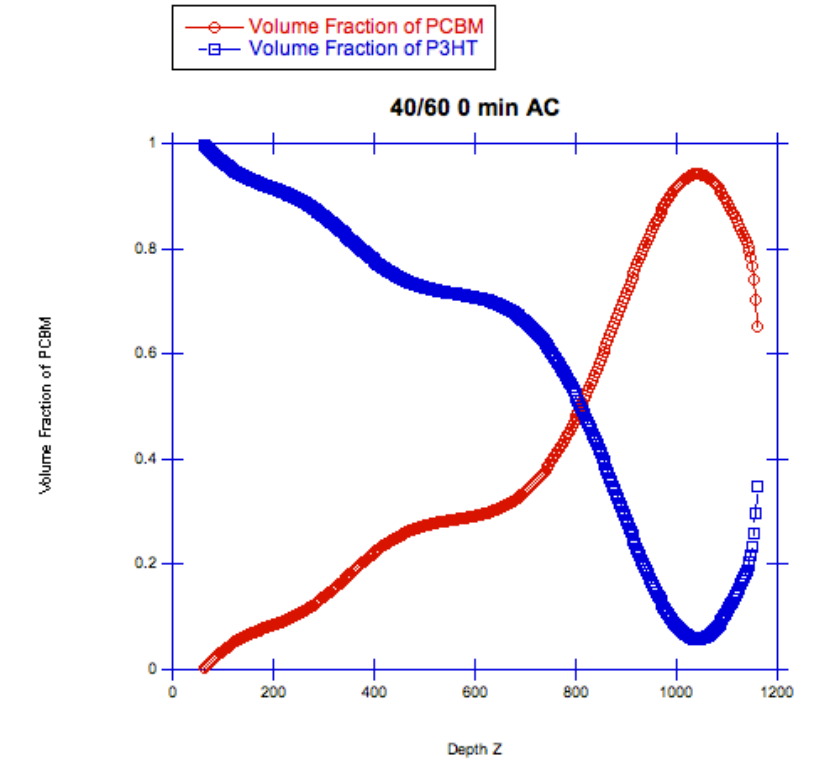

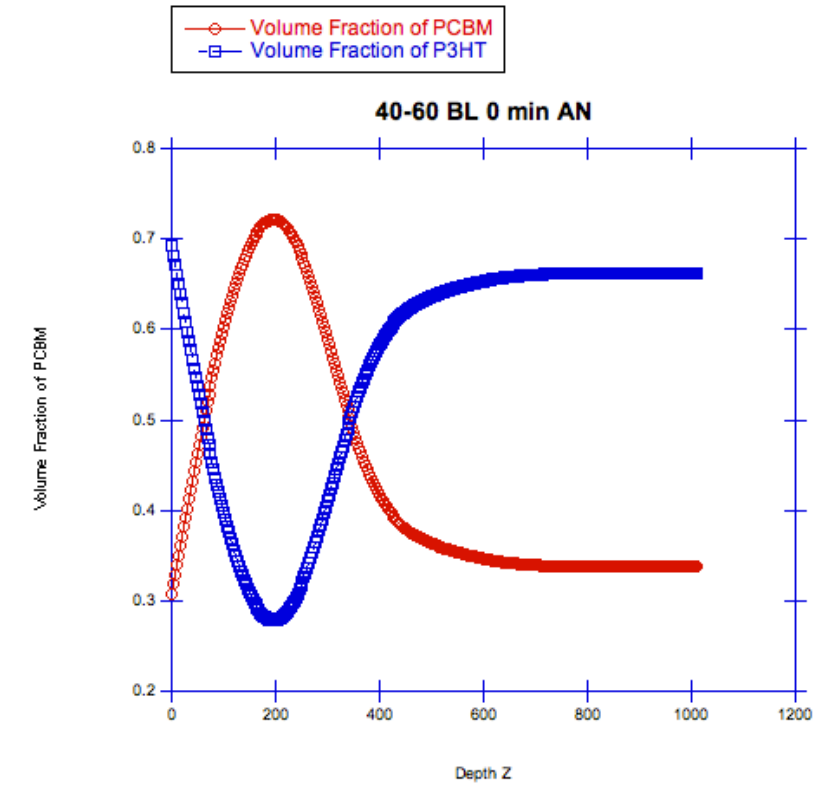

Figure 5.11 Continued

derived from the data in Figure 5.10. The as-cast sample has a PCBM rich layer near the silicon surface, and a P3HT rich layer near the air surface with a very broad interface between them. With annealing, the layers interdiffuse to form a PCBM rich layer near the air interface and mixed layer below that. However, the concentration of the P3HT layer at the air/surface interface is significantly less than that observed in the 20/80 bilayers, which is consistent with there being more crystalline P3HT. As the polymer chains begin to form more crystalline domains, the ability of PCBM to migrate away from the air interface is hindered. These crystalline domains block the pathways of PCBM, resulting in this higher concentration of PCBM at the air interface.

The reflectivity, SLD profile, and composition depth profile of the 40/60 PCBM/P3HT sample that has the P3HT annealed for 60 minute before PCBM deposition are shown in Figures 5.12, 5.13, and 5.14. This sample shows a P3HT rich layer near the air surface that is above a PCBM rich layer, demonstrating that the overall film structure is dominated by the immiscibility of P3HT and PCBM at this composition. As with other samples, the PCBM is able to diffuse to the silicon surface during the deposition of the PCBM onto the P3HT layer. It is interesting to note that the compositions of both 'layers' are about 10-15% of the minority component. Thus, in this sample the P3HT bottom layer can absorb about 15% of its volume with PCBM without significant change to its structure.

As mentioned above and in the 20/80 bilayer as-cast samples, the deposition process allows for the distribution of PCBM throughout the whole system, resulting

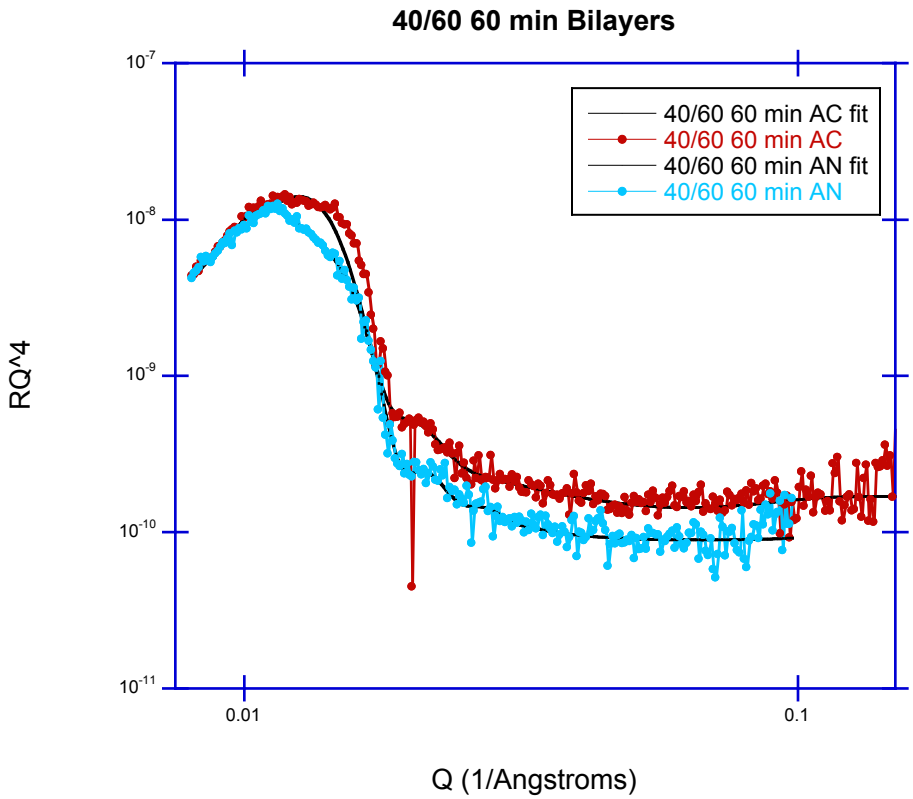

Figure 5.12 Reflectivity profiles with fits of 40/60 60 min bilayer as cast and annealed samples. Increased crystallization of P3HT decreases the changes seen in annealed samples.

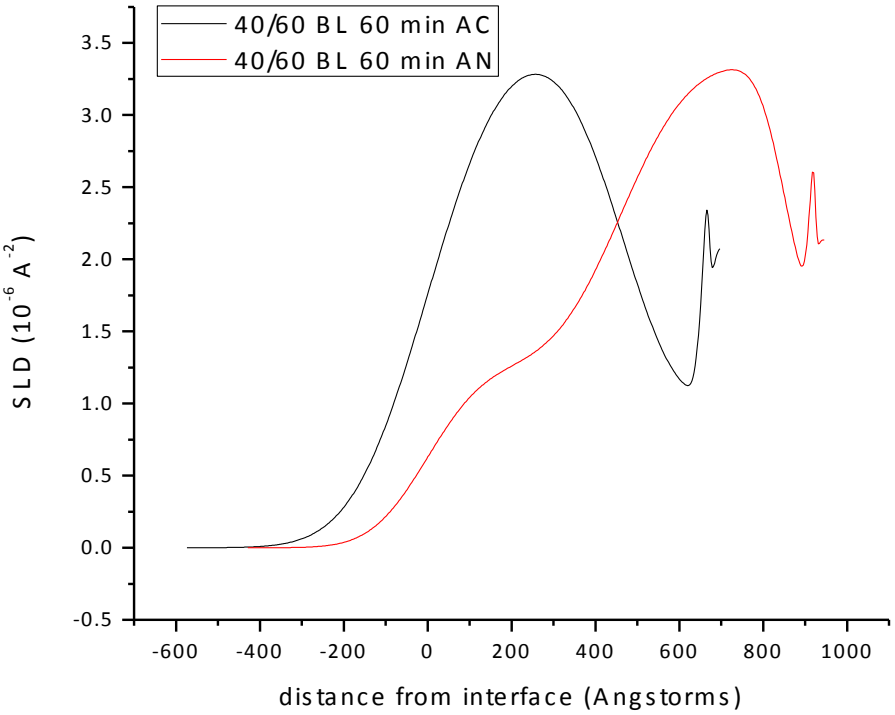

Figure 5.13 SLD profiles of 40/60 60 min as cast and annealed. Air/surface interface at Z=0.

Figure 5.14. Volume fraction or concentration depth profiles of the 40/60 60 min sample calculated from the SLD profiles. Z = 0 is the air/surface interface while Z ~ 800 Å denotes the Si substrate interface.

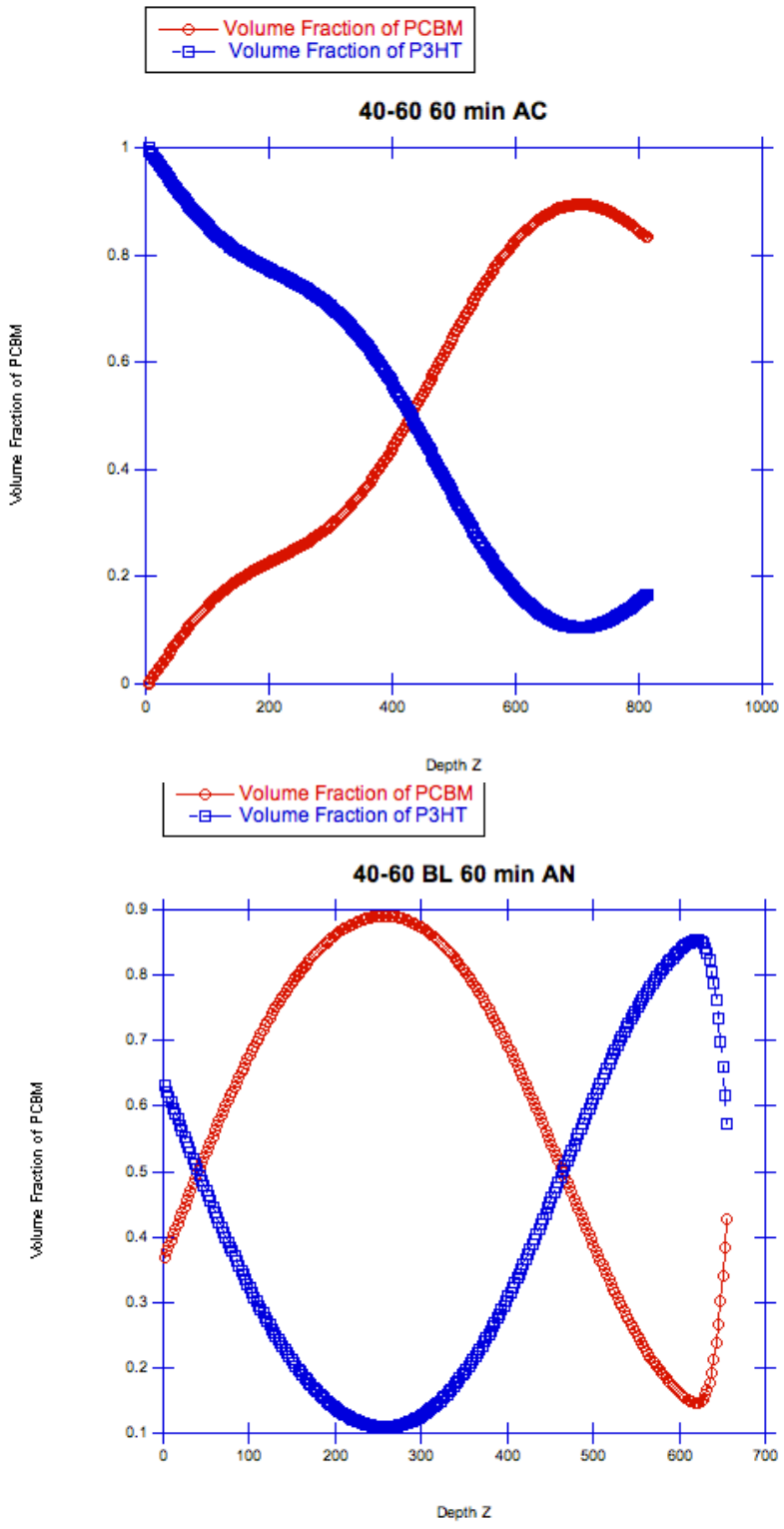

Figure 5.14 Continued

in an excess of PCBM at the substrate interface. This holds true even for the phase-segregated system of 40/60 bilayers displayed in Figures 5. 11 and 5.14. There is a more distinct PCBM layer formed near the substrate interface in the 0 minute as-cast than is formed in the sample with a longer P3HT crystallization time (60 minutes) prior to PCBM deposition. It appears that the crystal domains that are formed during this annealing process limit the diffusion of the PCBM throughout the thin film during deposition.

However, unlike the miscible 20/80 system, annealing has a more drastic affect on the concentration profile and redistribution of PCBM. With annealing the system forms more of a bilayer sample, with the P3HT rich layer at the substrate and a PCBM rich layer immediately below the air/surface interface. The increased crystallinity of the 60-minute sample appears to preclude the PCBM from going to the bottom layer with annealing, limiting the PCBM migration into the film. The composition of the bottom layer goes from ~30% PCBM in the 0 minute sample down to ~15% PCBM in the 60 minute annealed sample, which is consistent with the presence of more crystalline P3HT translating to less amorphous P3HT into which the PCBM can mix.

5.4 NEXAFS to Characterize the Surface Composition and Orientation of P3HT

The NEXAFS spectra of carbon containing compounds are dominated by resonances arising from transitions from the *1s* core level to unfilled molecular orbitals with π* and σ* character, which are specific to the bonding within different functional groups. As shown in Figure 5.15, the peaks at 285.0 and 286.46 eV are

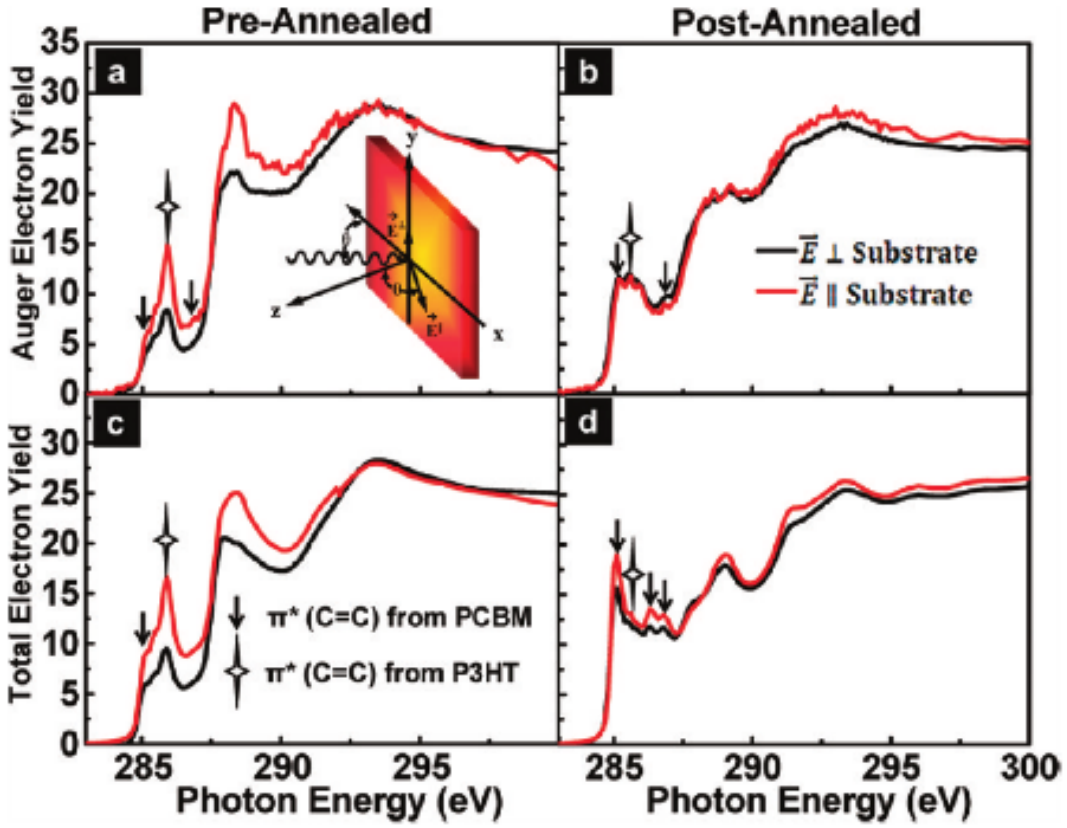

Figure 5.15 NEXAFS spectra showing the contributing peaks from PCBM and P3HT [76]

C=C π* resonances from PCBM, and the peak at 285.85 eV is the C=C π* resonance from P3HT. The broad features at higher energies are transitions to σ* orbitals. Synchrotron radiation is strongly polarized in the horizontal plane, as shown schematically in Figure 5.15 [80], so that by rotating the sample, the electric field vector of the X-ray beam can be changed from being nearly normal to the film surface (shallow-incidence angle) to being nearly parallel to the film surface (substrate, high-incidence angle). The angular dependence of the highly asymmetric π* and σ* orbitals can therefore be used to determine the orientations of the functional groups, [81,82] distinguishing between the edge-on and face-on orientation of the P3HT chain packing [80] at the surface. By taking NEXAFS measurements at two or more angles of incidence of the X-rays, the spatial orientation of an orbital can be determined [83].

Because of the spherically symmetric fullerene cage of PCBM, it should not exhibit angular dependence [84]. Therefore, comparison of the intensity of the π* peaks of PCBM and P3HT in Figures 5.16-5.19, can be interpreted to characterize the change in concentration of the two molecules at the surface. These figures can also be used to quantify the orientation of P3HT at the air surface. The dichroic ratio, R, as defined in Equation 5.3, can be determined by fitting the variation in resonance intensity with respect to incident light orientation; a plot of intensity versus the square of the sine of the incident angle should be linear. R can range from ≈0 .7 (1 is not possible because of a finite X-ray polarization) to -1, where more positive values indicating a greater edge-on conjugated plane orientation, and values approaching -1 indicate the presence of a perfectly flat, face-on orientation [85].

Figure 5.16. NEXAFS for 20/80 0 min bilayer.

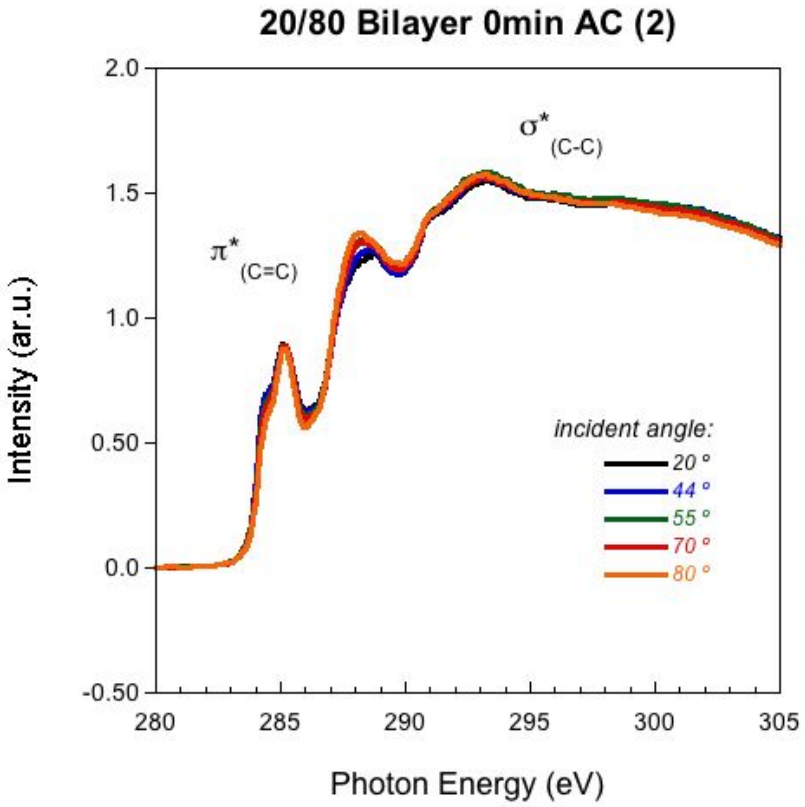

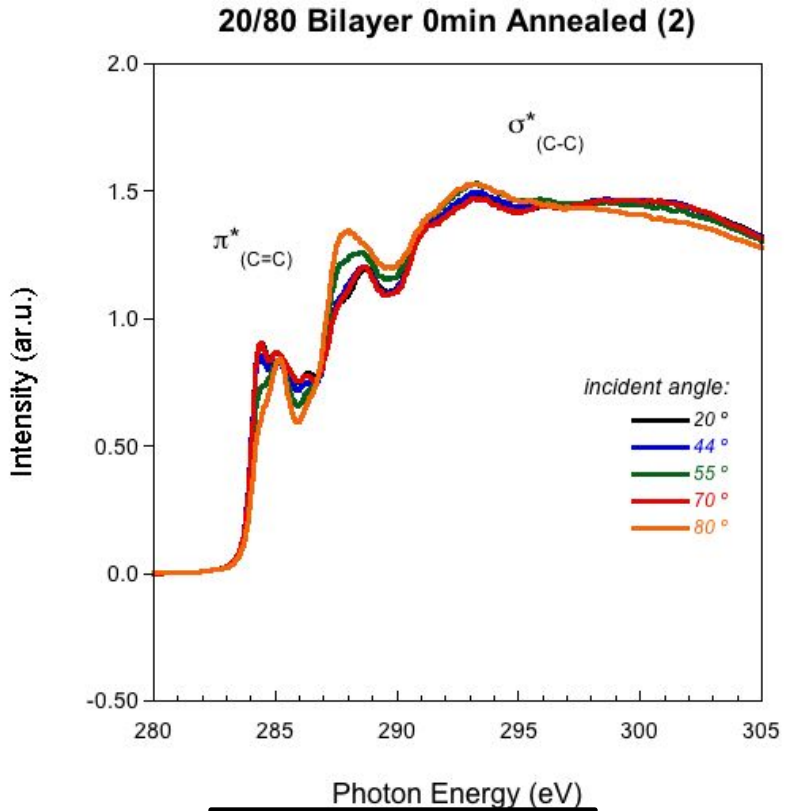

Figure 5.16 Continued

Figure 5.17. NEXAFS for 20/80 60 min bilayer.

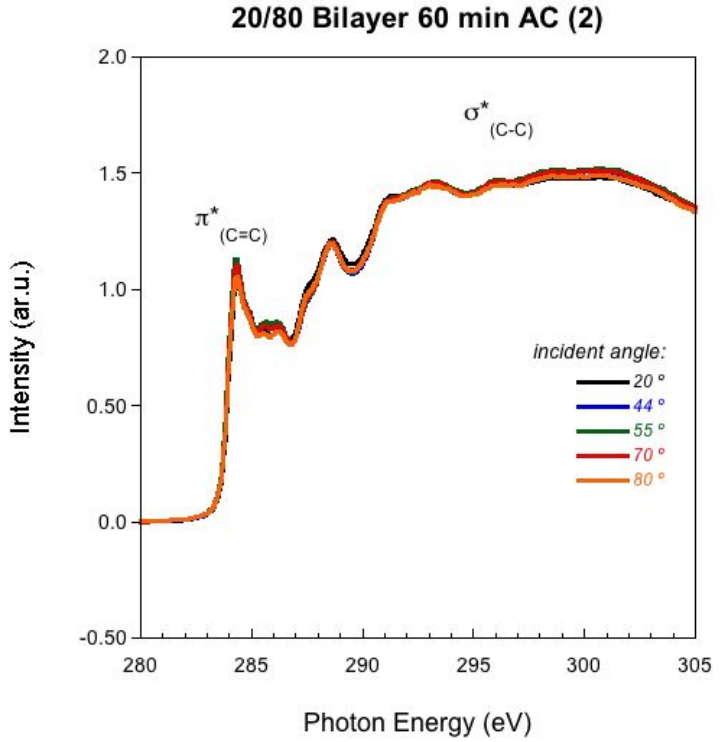

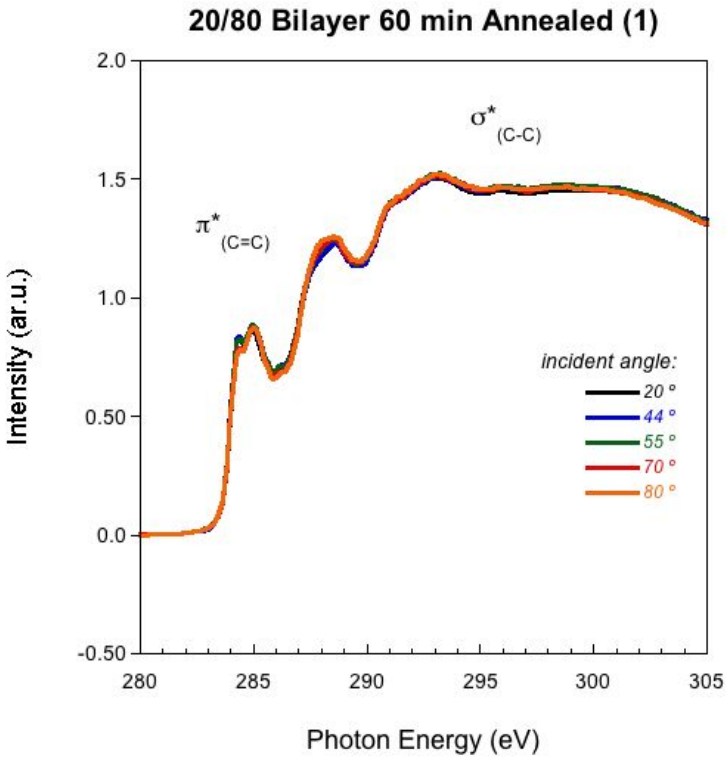

Figure 5.17 Continued

Figure 5.18. NEXAFS for 40/60 0 min bilayer.

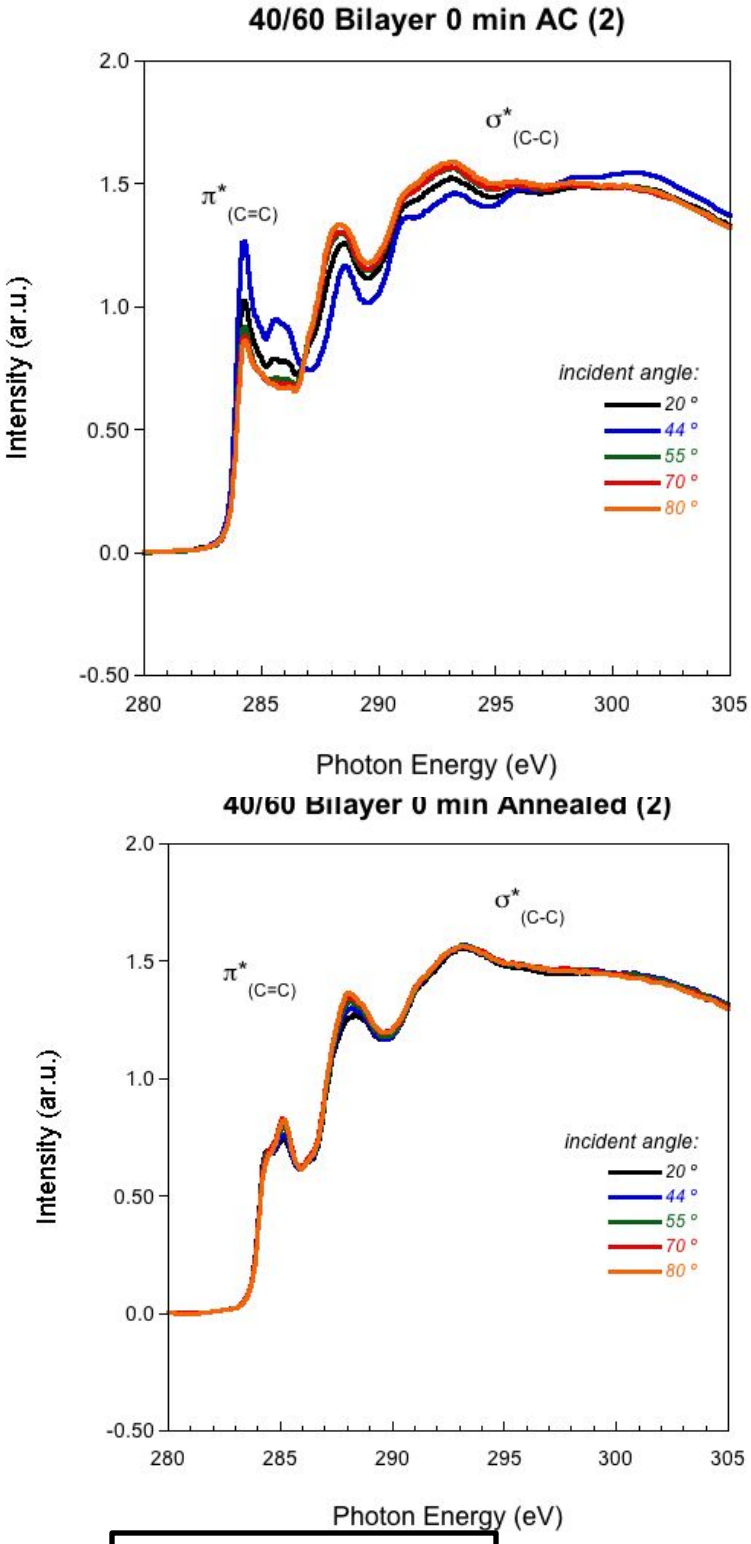

Figure 5.18 Continued

Figure 5.19. NEXAFS for 40/60 60 min bilayer.

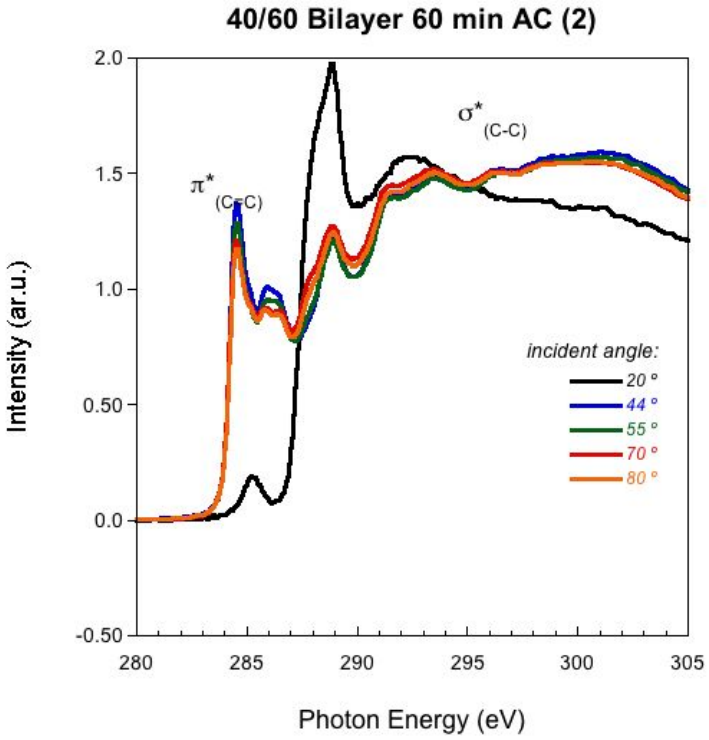

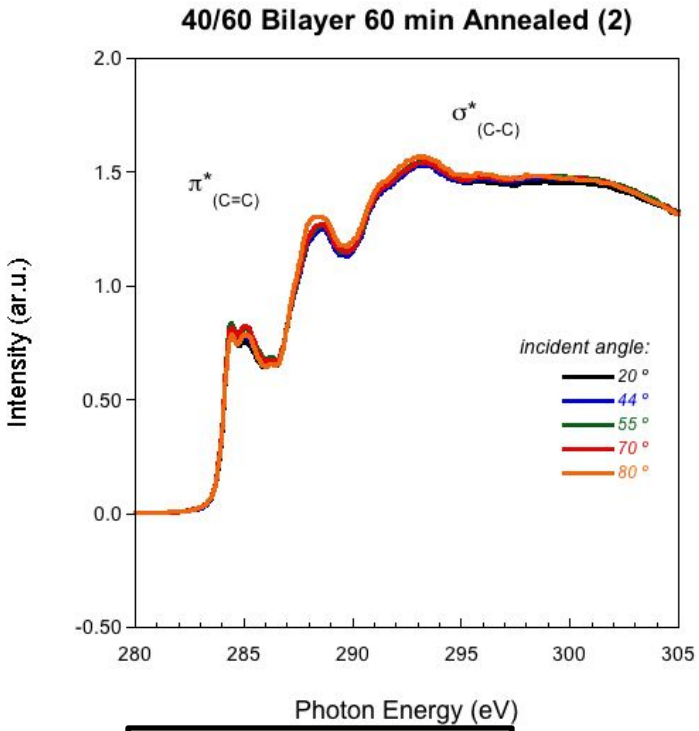

Figure 5.19 Continued

$$R = {(I_{90^\circ} - I_{0^\circ})}\Big/{(I_{90^\circ} + I_{0^\circ})} \qquad (5.3)$$

In Equation 5.3, I_{90° and I_{0° are the intensities at 90° and 0° incidence, linearly extrapolated from the data with incident angle as demonstrated in Figure 5.20a [86]

Evaluating the π* peaks also provides the composition of PCBM at the surface, which is plotted as a function of the crystallization time of P3HT for the 20/80 bilayer samples in Figure 5.21. The data indicate that there is an increase in PCBM at the air interface with longer P3HT crystallization times. This makes sense, as increased crystallization limits the ability of PCBM to diffuse from the surface into the bulk. More subtly, the increased annealing time of the P3HT before PCBM deposition results in a steady increase in crystal size, and minor changes to the overall crystallinity. Thus, this coarsening of smaller crystal structures into more robust crystalline domains hinders the migration of the PCBM away from the air interface and into the bulk.

Lastly, the measurement of the NEXAFS data at multiple incident angles allows us to calculate the dichroic ratio, R, which provides information on the orientation of the P3HT crystals at the polymer-air interface. Figure 5.22 plots the dichroic ratio, R, as a function of P3HT crystallization time. R provides insight into the alignment of the P3HT crystals, where more positive values indicate edge-on orientation of the chains, and more negative values correlate to polymer chains that are aligned face-on (Figure 5.20b). The results, shown in Figure 5.22, indicate that the P3HT chains are slightly more edge-on oriented, but fairly isotropically aligned (R ~ 0). The results also show that there is not a significant change in orientation of

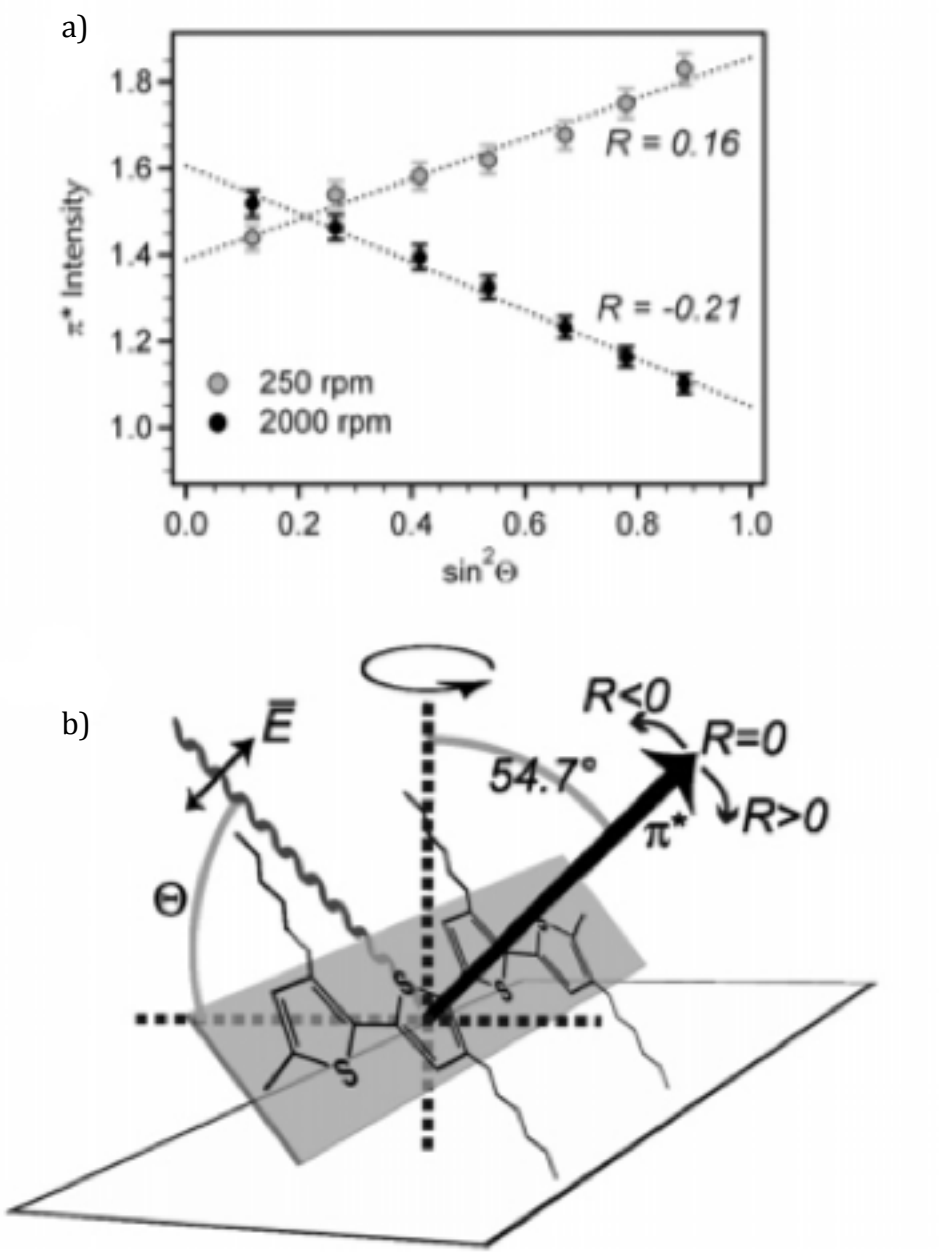

Figure 5.20 a)Dichroic ratio, R, calculated from the plot of intensity for different incident angles versus sine squared theta allows for the interpretation of P3HT orientation. b) Positive R values indicate more edge-on and negative R represents the more face-on orientation of P3HT. [72]

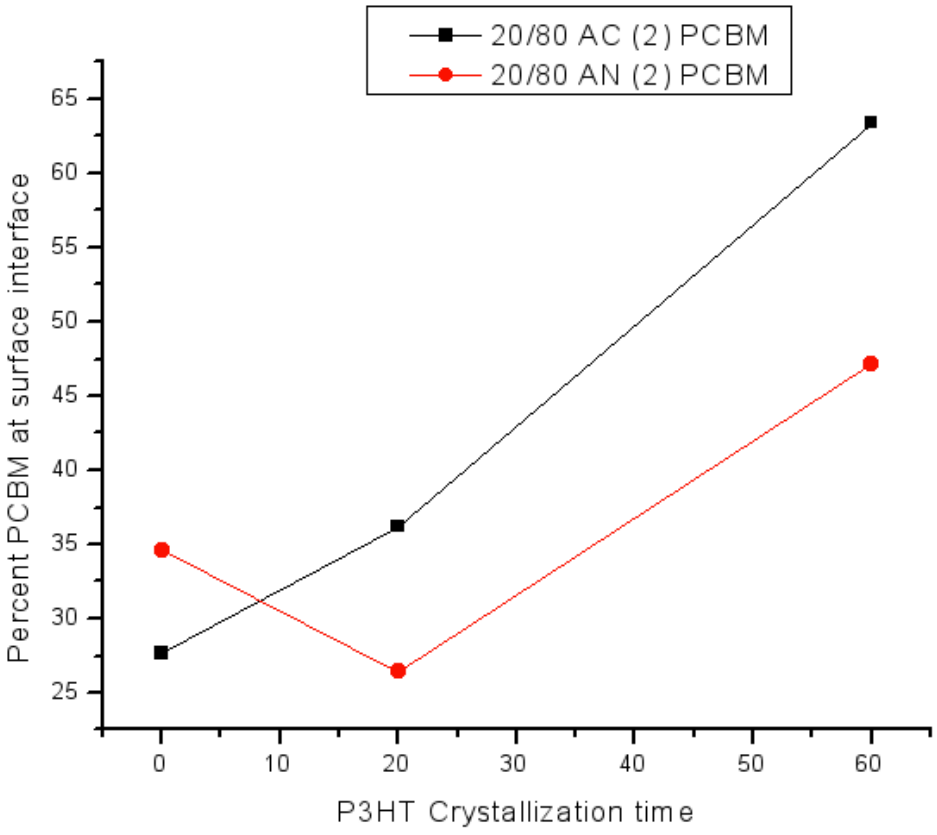

Figure 5.21 Composition of PCBM at the air/surface interface as a function of P3HT crystallization time before PCBM is deposited. These values are calculated from the NEXAFS spectra of the 20/80 bilayers.

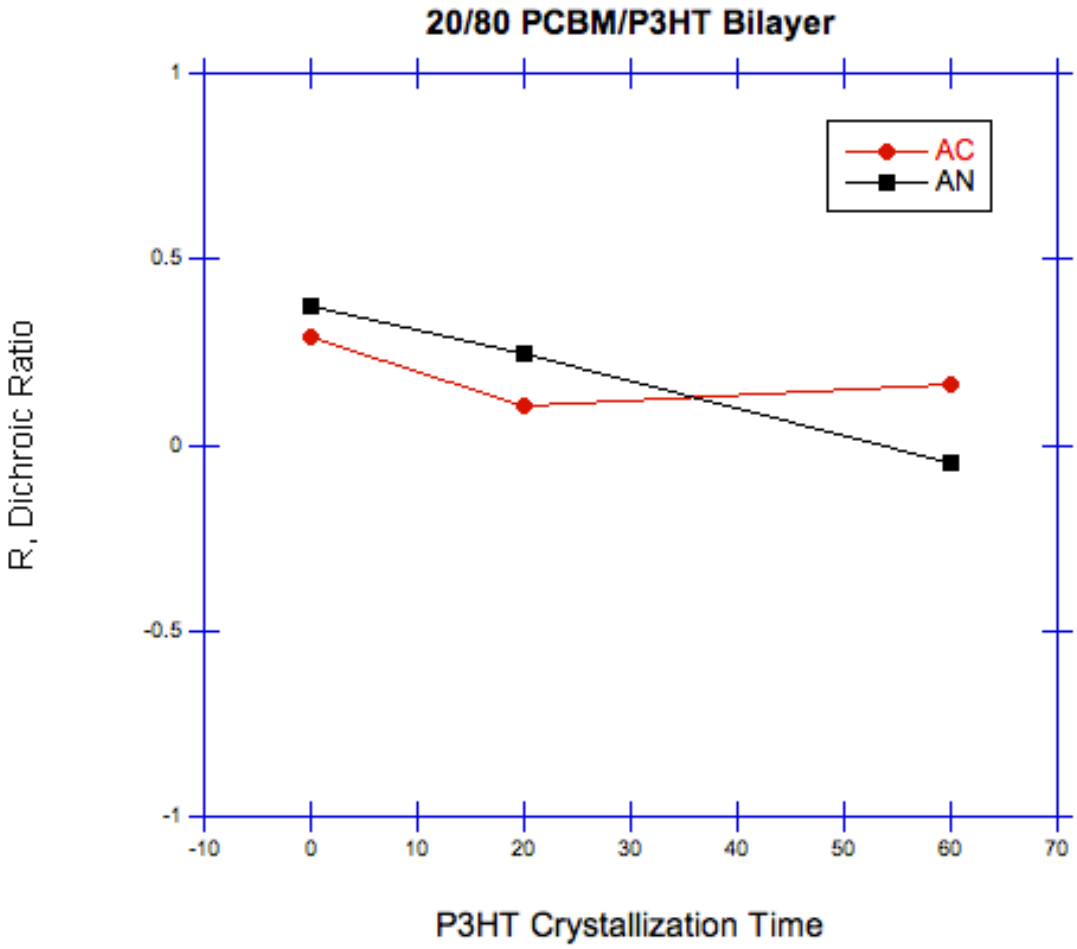

Figure 5.22 The dichroic ratio of the 20/80 bilayer samples as a function of P3HT crystallization time.

the P3HT chains with P3HT crystallization time before PCBM deposition or with annealing of the 'bilayer' at 150 °C for 15 minutes. This allows us to assign the analysis of the area under the P3HT d100 peak from the GIXRD results to the percent crystallinity of the polymer. Because our x-ray data is obtained on a 1-d detector, changes in the P3HT orientation near the surface could impact the measured peak area. This data, however, indicates that the orientation of the P3HT near the surface does not change with our annealing procedures.

5.5 Conclusion

Neutron reflectivity shows that the PCBM diffuses to the silicon surface during deposition in the 20/80 "bilayers", which is a composition where P3HT and PCBM are miscible. These results also indicate that the amount of PCBM able to diffuse to the silicon surface during deposition decreases when the P3HT is annealed at 150°C for 60 minutes, presumably due to the presence of robust P3HT crystals that limit the diffusion pathways of the PCBM to the bottom of the film during film drying. Regardless of the thermal history of the P3HT layer, the depth profile of these "bilayers" after annealing results in a nearly homogeneous film with slight concentration excesses at the air and silicon surfaces.

NR also shows that the depth profile of the 40/60 sample, which is beyond the PCBM miscibility limit, forms an initial layered structure upon consecutive deposition of the P3HT and PCBM. Regardless of the thermal history of the P3HT layer, the film initially consists of a PCBM-rich layer at the silicon surface that is topped with a P3HT-rich layer. Annealing these films at 150 °C for 15 minutes

forms a bilayer that consists of a P3HT-rich layer on the bottom that resides under a PCBM rich layer on the top, apparently driven by the miscibility limit of PCBM in P3HT. For all samples, pre-crystallization of the P3HT layer before deposition of the PCBM limits, but does not eliminate, the penetration of the PCBM through the P3HT layer to the silicon surface.

Finally, NEXAFS provides insight into the composition of the surface layer and the orientation of the P3HT crystals relative to the surface. These results are in reasonable agreement with neutron reflectivity results, indicating that the PCBM concentration at the surface increases with crystallization times due to the increased crystallinity limiting the diffusion of PCBM away from the surface. Analysis of the dichroic ratio indicates that the orientation of the P3HT slightly favors an edge-on orientation, but does not change much with thermal annealing, deposition process, or P3HT crystallinity. This regularity verifies that the interpretation of changes in crystalline structure as determined by GIXRD is from a change in crystallinity and not just a rearrangement of the orientation of the crystals.

Chapter 6

Understanding the Polymerization of Ethyl-Cyanoacrylate to Improve Fumed Latent Prints

6.1 Introduction

In many forensic investigations, the recovery and identification of latent fingerprints are vital in recreating a crime scene. A latent fingerprint is considered the transparent residue, deposited from a fingertip onto a substrate, leaving an image of the unique identifiable pattern of an individual's fingerprint ridges. Latent fingerprints are nearly invisible and must be enhanced in some way before they can be visually detected. Numerous methods have been developed to visualize fingerprints, including vacuum metal deposition (VMD), the powder method, and cyanoacrylate (superglue) fuming method (CFM). As latent fingerprints age, however, changes to the chemical nature of the print residue results in a decrease in the quality of the impression obtained using CFM. The nature of this change in the fingerprint residue and how it affects the polymerization of ethyl cyanoacrylate (ECA) is not well understood. To address this shortcoming, the polymerization processes of superglue fuming during latent fingerprint development are examined. A variety of methods to improve the quality of aged latent prints developed by CFM are investigated, including the rehydration of the prints and control of the print temperature during polymerization. At the same time, a molecular level understanding of print "hardening" that is often required post fuming is investigated.

6.2 Experimental

6.2.2 Fuming from Sodium Lactate solution

Materials: The chemicals l-sodium lactate (Fluka), ethyl cyanoacrylate (Sirchie), sulfuric acid (Fischer), and 30% hydrogen peroxide (Fischer), hydrochloric acid (Fischer), ACS grade tetrahydrofuran (THF) (Fischer), and ACS grade toluene (Fischer) were used as received. Nanopure water was obtained using a Milli-Pore water treatment system. The pH of each solution was controlled with 4, 7, and 10 pH buffer solutions (Fischer) along with a pH meter (Eutech Instruments) and electrode (Accumet) to measure the pH of each lactate solutions. Silicon wafers obtained from Wafer World were used as the substrates.

A 10mM sodium lactate solution was made by adding 0.0544g of sodium lactate to 100mL of nanopure water in a 100mL volumetric flask. The target pH of the 10mM sodium lactate solution was 4.73, which was obtained by the addition of 1M HCl or 1M NaOH as needed. Solutions were then stored in a refrigerator until needed. The pH was altered for two reasons. First, to provide a method to control and adjust the mechanism by which ions are introduced into the systems, and because the pH has a direct effect on the structure of the initiators. In the lactate system, the variation in pH dictates the counter ion at the carboxylate group, either a sodium or hydrogen atom. In an alanine system, the carboxylate group is altered in much the same way as in the lactate system; however, pH adjustment also impacts the protonation of the amine as well as the zwitterionic nature of amino acids. Amino acids display zwitterionic behavior around their isoelectric point [56]. Secondly, the pH was altered to mimic the environment in the body [56].

Silicon wafers were cut into 1 inch by 1 inch pieces and cleaned via submersion into "piranha" solution for one hour. The piranha solution consisted of a three to one mixture of sulfuric acid to 30% hydrogen peroxide. After an hour, the wafers were taken out of the piranha solution and washed with nanopure water and dried under a stream of dry N_2 gas. The cleaned wafers were stored under vacuum until needed.

Sodium lactate droplets (3-6 drops ~50μL) were deposited onto a Si wafer via an autopipet. The silicon wafer was held in place during the fuming process by a 3-arm clamp attached to a ring stand at a distance of 2 inches above a hotplate containing an aluminum weighing pan with approximately 2g of ethyl cyanoacrylate monomer. Once white fumes appeared, the Si wafer containing the droplets of initiator was turned upside down so that the Si wafer and droplets were in direct contact with the cyanoacrylate monomer vapors. A cardboard box was placed over the entire set up as a way to concentrate the fumes onto the initiator droplets. Droplets were then fumed for varying times of 30, 60, 90, 120, and 150 seconds.

6.2.3 Examination of the crosslinking of poly(ethyl cyanoacrylate)

Materials used in these studies were ethyl cyanoacrylate (Sirchie), standard microscope slides (Fischer), and ACS grade tetrahydrofuran (Fischer).

Clean glass slides were weighed via a Mettler Toledo MS105 Semi-micro balance with 0.015mg repeatability. Four prints were applied to the slide via our standard fingerprint deposition method. The prints were then fumed for ten minutes according to the procedure described above. After fuming, the slides were then weighed again to obtain the mass of polymer on the print. Prints were then

allowed to dry for varying time intervals ranging from 2-24 hours. During drying, the slides were covered from the top to prevent contamination but vented from the sides to allow for interaction with atmospheric conditions in the lab. After achieving the desired drying time, samples were then soaked in THF for 30 minutes to remove the "uncrosslinked" polymer from the print ridges. After soaking, the samples were allowed to dry and the mass of the remaining "crosslinked" polymer was measured.

6.2.4 Quartz Crystal Microbalance to Monitor the Mass

The increase in mass of polymer on the print during fuming was monitored using a research quartz crystal microbalance (QCM) from Maxtek, Inc, which has a mass resolution of <0.4 ng/cm^2. Prints where deposited on crystals using the standard fingerprint deposition method. The QCM crystal was then placed in the probe and clamped face down 3 inches above a hotplate containing an aluminum pan of approximately 2g of cyanoacrylate. Once fumes could be seen coming from the pan, the sample was covered in the cardboard box setup previously mention and then monitored for changes in mass as the print was exposed to cyanoacrylate fumes for ten minutes. 5 MHz Ti/Au polished QCM crystals were purchased from Maxtek.

6.2.5 Temperature Control of Print During the Fuming Process

The temperature at which the fingerprint and monomer are exposed to vapor is controlled by using a cooling block. The temperature of the block was maintained by flowing a mixture of antifreeze and water through a Brinkman MGW Lauda RM6 heater-cooler. A temperature probe monitors the temperature of the substrate

throughout the entire fuming process. Prints were then fumed for ten minutes and then analyzed for mass and molecular weight changes via mass balance and SEC. SEC measurements were completed using a Polymer Labs GPC 20 equipped with two plgel 5 μm mixed C columns and a WellChrom K-2301 RI detector. HPLC-grade Toluene was used as the flow rate marker, and THF was used as the eluent in all GPC experiments, which were calibrated using polystyrene standards. SEC solutions were made by sonicating the fumed prints in THF for 15 minutes, and then concentrating the solution down in a Fisher brand 4 gram vial. This solution was filtered with a PTFE 0.45 μm syringe filter and then injected into the SEC using a gas-tight 2.5 mL Hamilton syringe. For sonication, a Branson 1510 40 KHz sonicator was used.

6.2.6 Exposure of the Latent Print to Water Vapor

Latent prints applied to glass slides and QCM crystals were exposed to water vapor for ten minutes and then fumed with cyanoacrylate to determine the impact of the exposure to water vapor, and potential rehydration, on the mass and molecular weight of the polymer that grows off of the modified print. QCM provides a measure of the change in mass on the crystal in real time during the fuming of all prints that were exposed to water vapor prior to fuming. The amount of polymer that grows off of the print on the glass slides was analyzed by a mass balance, accompanying the determination of the molecular weight of the poly(ethyl cyanoacrylate) via SEC. Prints were applied as clean prints using the standard fingerprint deposition method and then as oily prints by touching one's forehead after the hand washing and drying process.

6.2.7 Infrared Spectroscopy of the Curing of Poly(cyanoacrylate)

For initial studies, a quartz apparatus was made by the Chemistry Department glass shop, which consists of a Teflon cuvette confined between two quartz slides. To monitor the reactions that occur in the polymerization of ethyl cyanoacrylate monomer, neat ECA monomer was placed in the cuvette and an IR spectrum was taken every two hours for 24 hours. The absorbance spectra were collected on a Varian 4100 FT-IR Excalibur Series instrument, from wavenumbers 400-8000 at 128 scans with a resolution of 0.5 cm^{-1}. A background of the empty quartz apparatus was accounted for in the analysis. Subsequent experiments utilized gold-coated slides from Evaporated Metal Films Corporation as the substrate for latent prints. Using the same print deposition and fuming process, the spectra of a fumed latent print was obtained and compared to the spectra from the curing of the ECA monomer in the bulk to identify variations in the reactions that occur in the two polymerization processes.

To monitor the growth of poly(ethyl cyanoacrylate) in-situ during the fuming process, a Bruker Equinox 55 FTIR spectrometer equipped with an Axiom Analytical Diamond ATR probe (DMD-270) was used. The FT-IR-ATR spectra were collected using a Nicolet Nexus spectrometer equipped with a Nicolet Smart Endurance single bounce diamond ATR accessory. Each spectrum consisted of 64 co-added scans obtained over the 4000 cm^{-1} to 525 cm^{-1} region at a resolution of 4 cm^{-1}. The spectra were collected every 5 seconds for times up to ten hours. Dipping the probe tip into cyanoacrylate monomer during its polymerization monitored the chemical reactions that occur during the polymerization of the monomer in the bulk. To monitor the

polymerization of ECA during the fuming process, a clean latent print was applied to the diamond tip of the probe via the standard print laying method. The print was then exposed to cyanoacrylate fumes for ten minutes using the fuming technique described above. After ten minutes of fuming, the hot plate was turned off and the continued polymerization and other reactions were monitored for up to ten hours. A background of the monomer vapor was subtracted out to insure the reaction being monitored was of the polymerization of the cyanoacrylate.

6.3 Sodium Lactate

Sodium lactate has been identified as one of the primary components of eccrine sweat in the fingerprint[87]. It is also been shown to be a primary initiator of the polymerization of ethyl-cyanoacrylate during fuming[45]. As such, the growth of PECA from the fuming of sodium lactate droplets was examined. In this procedure, four to six drops of sodium lactate were placed on a Si wafer and fumed for various times. With increased fuming times from 30 seconds to 150 seconds, the mass of the polymerized cyanoacrylate accumulated on the droplets increases linearly, as seen in Figure 6.1. This increase in mass verifies the ability of ethyl-cyanoacrylate vapors to polymerize from the individual initiators that are in clean latent prints.

6.4 Rehydration of Aged Fingerprints by Exposure to Water Vapor

It is known that one change in print composition with aging is the loss of water. Therefore, exposing aged latent prints to water vapor in an attempt to rehydrate them may be a reasonable method to improve the growth of PECA during the fuming process from aged prints. Previous work in our group has shown that

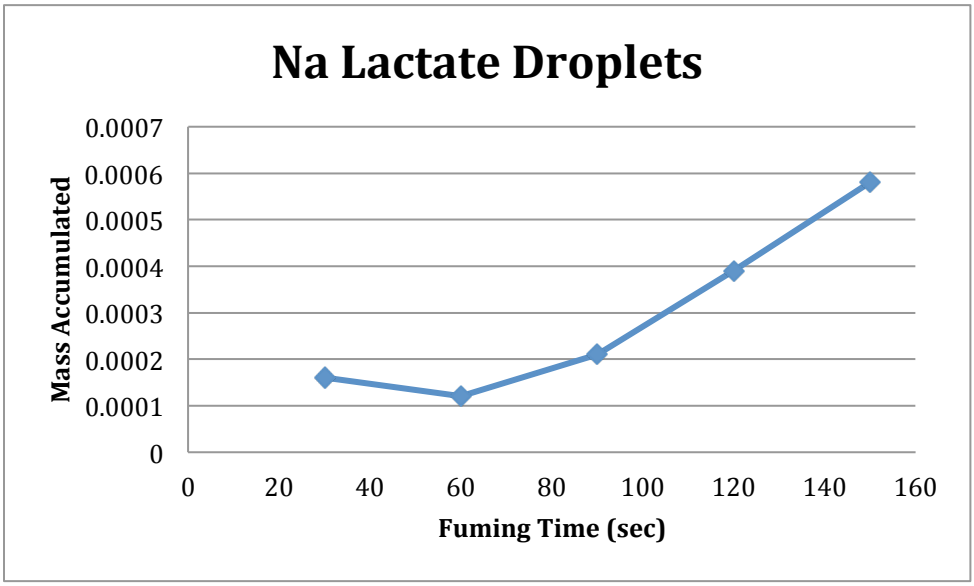

Figure 6.1 Mass accumulation on sodium lactate drops with exposure to ethyl cyanoacrylate vapor.

exposing aged latent prints to ammonia and acetic acid vapor prior to fuming improves the quality of the fumed print[42]. Similarly, can the introduction of water to the aged print improve the quality of the fumed print? It is important to remember that the role of water in the polymerization of ECA can vary; while water can act as an initiator for polymerization, it can also act as a terminating agent limiting the polymerization and development of the print. [45]

To examine the efficacy of rehydrating aged prints, an initial study was performed, where clean prints were applied to glass slides and allowed to age for 30 days. After the aging period, the prints were exposed to boiling water vapor or room temperature water vapor, after which they were fumed for ten minutes. The mass of the resulting print and poly(ethyl cyanoacrylate) after the fuming process is plotted as a function of the water exposure time in Figure 6.2. A control print was fumed without any water exposure. The ability of water to rehydrate the aged print is shown by the increase in the print mass with water vapor exposure, especially for those samples exposed to room temperature water vapor. In this sample, the rehydration improves the growth of PECA, however, the sample exposed to boiling water vapor shows a different trend. In this case, the amount of PECA formed decreases with extended exposure to boiling water vapor, which may indicate that the boiling water is washing away initiators in the print prior to fuming.

As a follow on study, the impact of shorter aging times and the composition of the print on the ability of water vapor exposure to alter the growth of PECA from the aged print during fuming were examined.

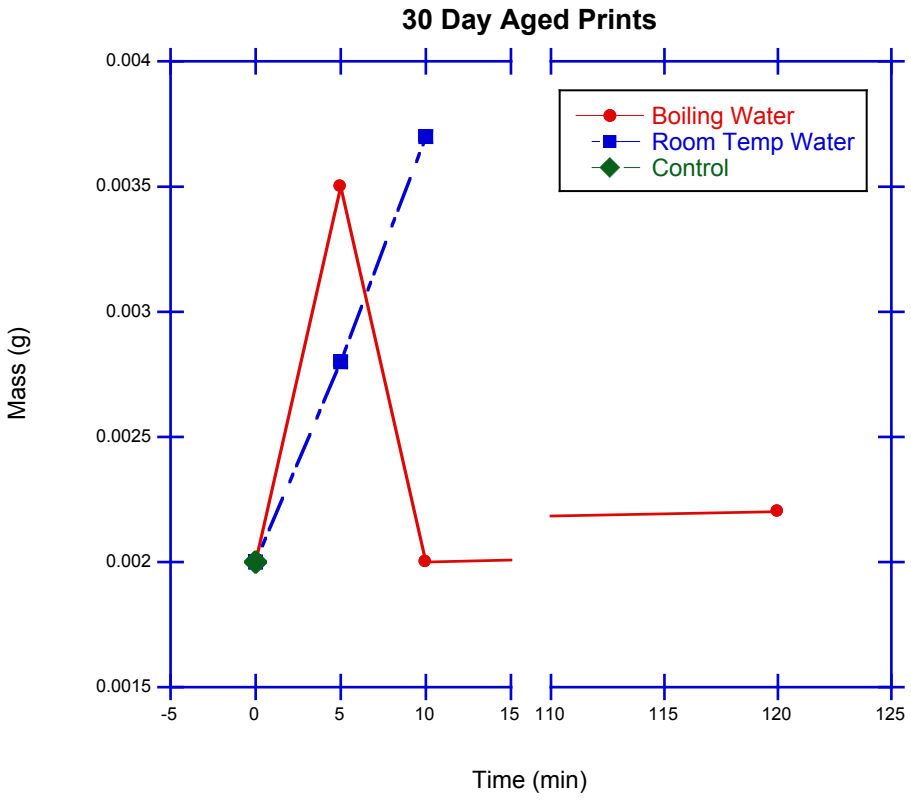

Figure 6.2 Mass of 30 day aged prints after fuming as a function of water vapor exposure time.

For this experiment, the impact of exposure to water vapor on the amount of polymer that is grown off of fumed latent prints that were aged for 0, 14, and 28 days is examined. Figure 6.3 shows the average change in mass of each print after water vapor exposure, which is determined by weighing the print before and after exposure to the water vapor. These results document the ability of the print to absorb water and rehydrate. This data shows that exposure of the print to boiling water decreases its mass, indicating that the water vapor is washing off some of the print. However, it would appear that exposure of the prints to room temperature water vapor increases the mass of the print, indicating that these prints take up water and possibly rehydrate. In particular, the oily print that is aged for 14-days seems to absorb water, but the impact of this change on the quality of the fumed print must now be determined.

In Figure 6.4, the amount of PECA that grows off of each print as a result of fuming is plotted. The results show that the fresh prints (0 day) do not exhibit an increase in the amount of PECA grown off the print with water exposure after exposure to either room temperature or boiling water vapor. It is also important to note that the error of the balance is reasonably large (2e^-4 mg), for these measurements.

The amount of PECA that grows off the prints that were aged for 14 days do not change much with water exposure, but there is an indication that exposure to boiling water vapor decreases the amount of PECA grown off of the print. Specifically, the oily print that was exposed to boiling water vapor shows less polymer growth, in agreement with the data presented in Figure 6.3, which showed

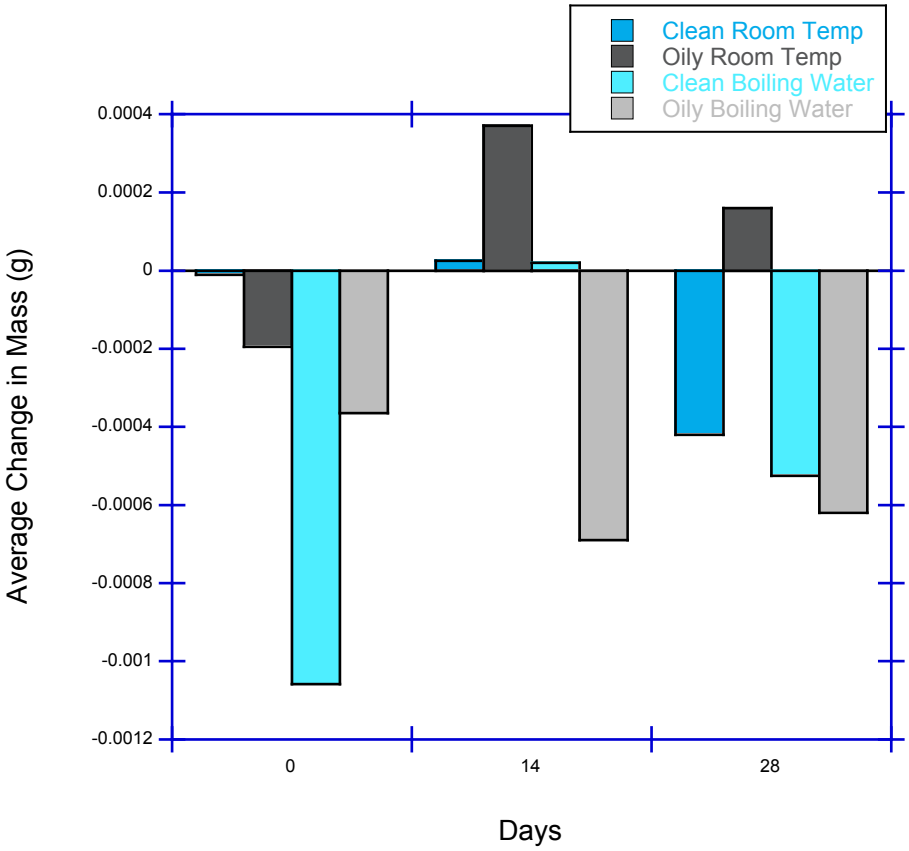

Figure 6.3 Change in mass of 0, 14, and 28 day aged prints after water vapor exposure.

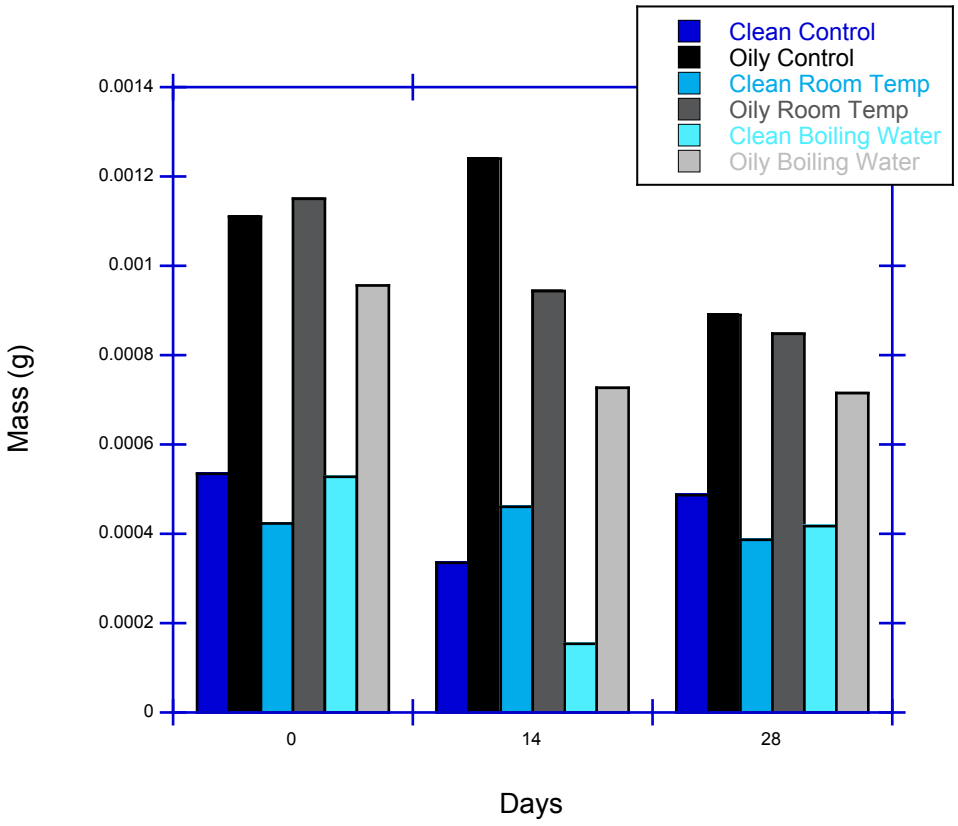

Figure 6.4 Accumulated mass after fuming for 0, 14, and 28 day aged clean and oily prints exposed to water vapor prior to fuming.

a loss in print mass after exposure to boiling water vapor. Lastly, the data also shows that the prints that are exposed to water vapor after 28 days of aging do not exhibit a significant increase or decrease in the polymer grown on the print during the fuming process.

The sensitivity of the balance used in these experiments limits the reliability of the interpretation of these results, thus similar experiments using the quartz crystal microbalance, which has much greater sensitivity were completed.

6.5 The Impact of Water Vapor Exposure on the Fuming of Aged Latent Prints using Quartz Crystal Microbalance

The mass of PECA that grows off of the latent print is monitored in real time using QCM, documenting the affect of water vapor exposure on the growth of PECA from aged prints. Figure 6.5 and 6.6 plot the change in mass of the aged print with exposure to water vapor as a function of exposure time. A linear fit to the data provides a slope that quantifies the rate of water uptake. Comparison of Figures 6.5 and 6.6 shows that the mass of the latent print increases with exposure to room temperature water, however the mass of the aged print decreases with exposure to boiling water vapor. This verifies that exposure of the latent print to boiling water vapor washes some of the print away. This is in contrast to the prints that are exposed to room temperature water vapor, whose mass increases slightly or remain the same.

However, the aged latent prints that are exposed to room temperature water vapor do not grow more polymer from the print during fuming than a similar print that is not exposed to water. This is shown in Figure 6.8, which shows photographs

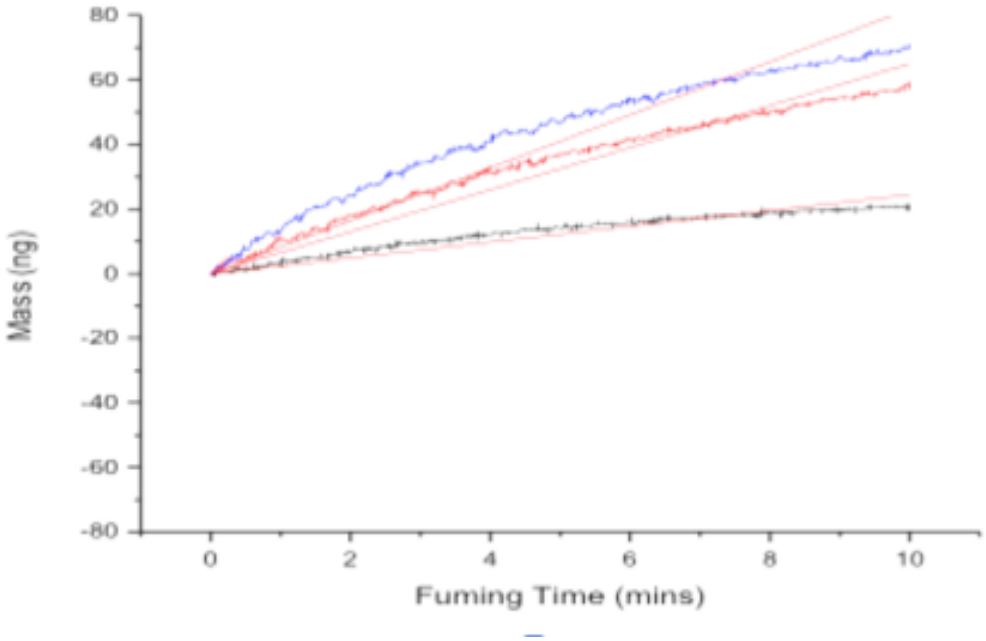

Figure 6.5 QCM data of aged clean prints exposed to room temperature water vapor.

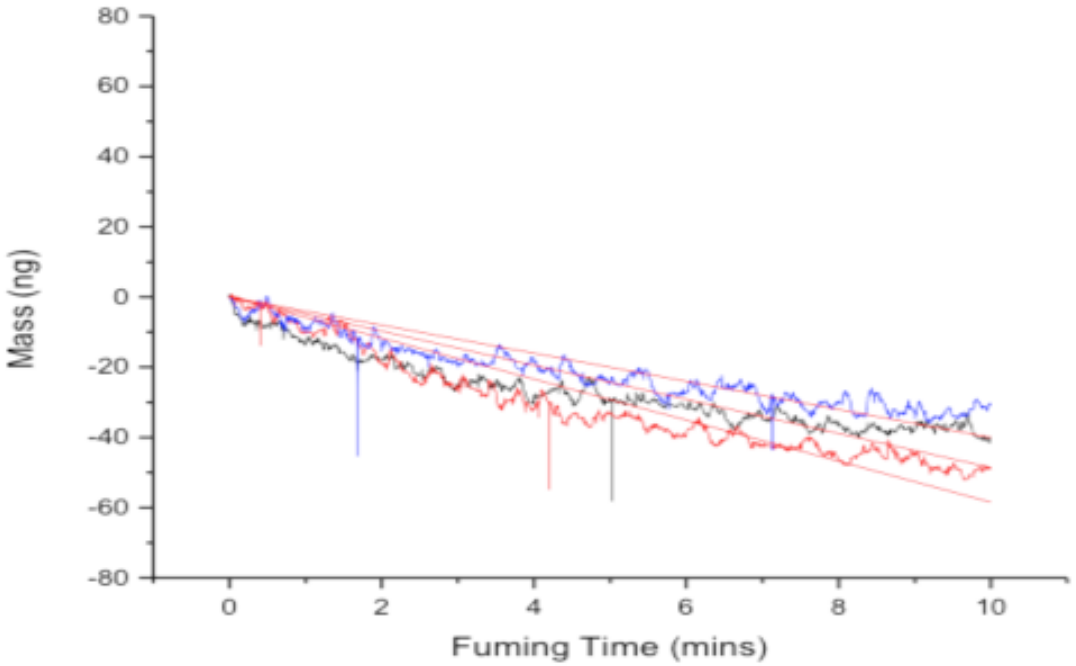

Figure 6.6 QCM data of aged oily prints exposed to boiling water vapor.

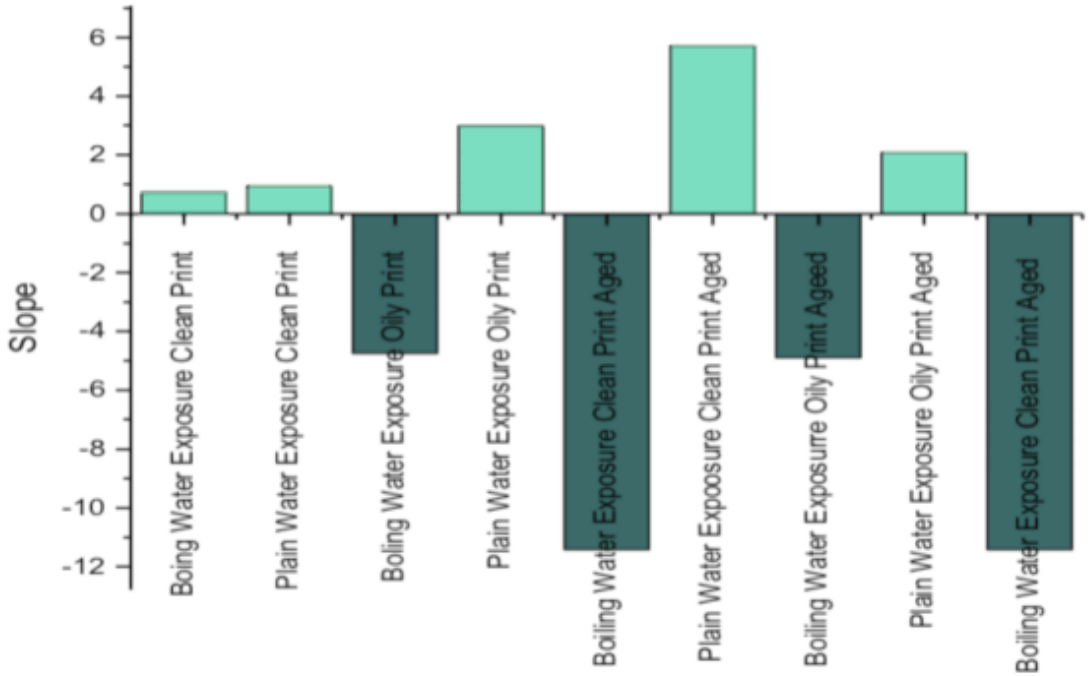

Figure 6.7 Rate of QCM mass accumulation during fuming process for clean and oily prints with boiling and room temperature water vapor exposure.

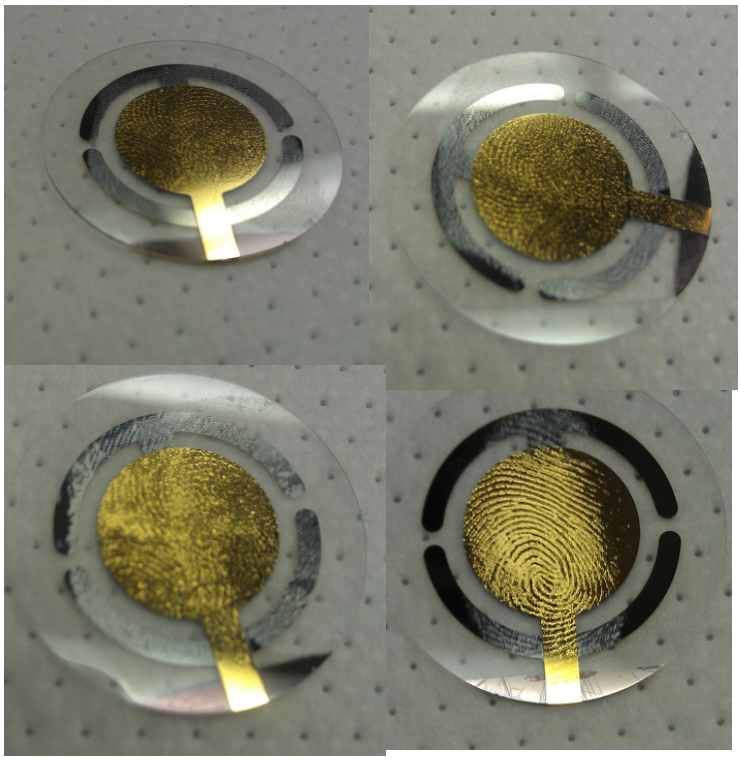

Figure 6.8 The initial clean fresh print is shown (top left), then after it is exposed to room temperature water (top right), and the print after fuming (bottom left). Lastly, a fumed clean fresh print with no water vapor exposure (bottom right).

of clean latent prints that are aged for 0 days and exposed to room temperature for 10 minutes before and after fuming. The effect of exposure to the room temperature water on the quality of the print can be observed by comparing the first and second photograph. The first photograph shows a clean fresh latent print after being deposited. The second photo shows the minimum change in the print ridges after exposure to room temperature water vapor. However the third picture (bottom left) clearly shows that fuming the print exposed to water vapor results in no distinguishable ridge formation. The fourth photograph is a picture of the fresh clean fumed print that is not exposed to water, which exhibits clear ridge detail as a result of fuming. This comparison clearly shows that exposure of the print to water vapor hinders, rather than helps, the formation of polymer on the print ridges.

Thus, the simple rehydration of aged latent prints is not a viable pathway to revive the components in a latent print that initiate the growth of poly(ethyl cyanoacrylate) from the print during fuming. Aggressive water vapor exposure procedures appears to erode the print, while modest water vapor exposure is insufficient to activate any initiators that may still remain in the print.

6.6 Improved Development of Latent Prints with Temperature Control

As print rehydration does not appear to be a viable pathway to improve the quality of fumed aged latent prints, other experimentally controllable variables must be considered. The polymerization of ethyl cyanoacrylate occurs by an anionic mechanism. Fundamental studies of anionic polymerization have demonstrated that decreasing the temperature creates more solvated (less tightly bound) ion pairs at the growing chain end, which should increase the initiation and propagation rate

of the polymerization. [88,89] Moreover, previous studies have shown that lowering the temperature of ECA polymerizations increases the rate of the reaction, due to a loosening of the ion pair that propagates the polymer chain growth.[46] Additionally, anionic propagation often occurs with several side reactions at higher temperatures. Therefore lowering the temperature suppresses these side reactions and termination [46]. This suggests that a decrease in temperature of the fuming of a latent print will increase the rate of polymerization, therefore more effectively utilizing initiators that exist in the print and potentially creating more polymer and a better quality fumed print.

The use of a heating/cooling block allows us to control the temperature of the print during the fuming process. Figure 6.9 shows a plot of the mass of polymer that forms on the print as a result of the fuming process as a function of fuming temperature (Appendix 1 shows the molecular weight results). At a quick glance, it is clear that lowering the temperature does in fact improve the rate of growth and limit termination.

It is clear in Figure 6.9 that increasing the temperature above that of room temperature does not improve the polymerization process, forming little polymer. However, just a ten degree drop from 40 °C to 30 °C yields a significant increase in the rate of propagation, resulting in significant increase in the amount of polymer that is formed.

Figure 6.10 compares the growth of polymer at room temperature and at -9 °C, verifying that the mass of PECA accumulated on the prints at the lower temperature is substantially higher than that of prints fumed at room temperature.

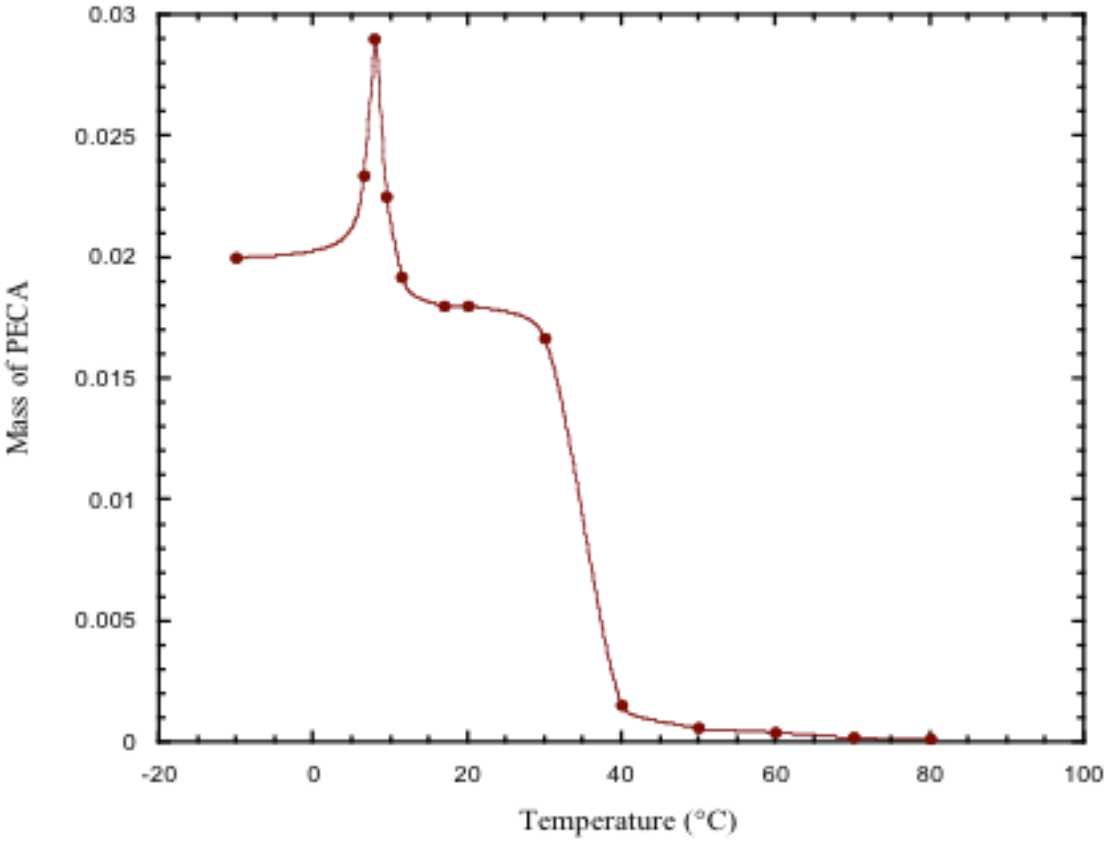

Figure 6.9 Mass of polymer on the fumed prints as a function of the temperature of the print during fuming.

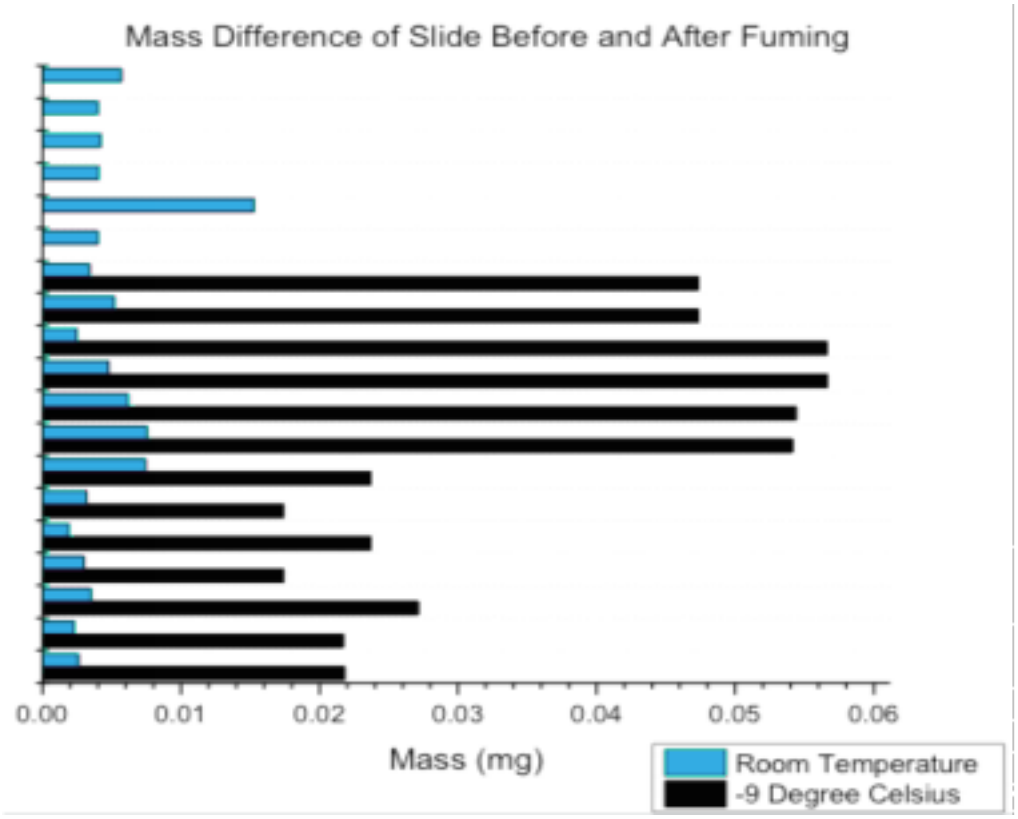

Figure 6.10 Comparison of mass difference of prints fumed at -9 °C and room temperature of 25 °C.

However, as the temperature is lowered, the amount of polymer first increases, until the temperature reaches 8-10°C, after which it begins to decrease again. This is likely the result of the fact that the propagation reaction slows at lower temperature because of the decrease in the kinetic energy of the monomer as it reacts with the growing chain end. These results therefore indicate that at ~10 °C defines the optimum temperature where there is a balance of looser ion pairs and sufficient energy to allow the reaction of monomer to the propagating chain end.

6.7 Investigation of Crosslinking in Fumed Latent Prints

Many forensic scientists have found that fumed latent prints will smear shortly after fuming. To prevent this, scientist often allow the prints to "harden" for 24 hours after being fumed. It is thought that this "hardening" time allows the polymerized cyanoacrylate to crosslink on the print ridges. This 24 hour waiting period slows down the analysis of evidence in a crime scene, and there is a desire to speed up this process. Therefore, investigation of the rate and molecular level mechanism of this "hardening" effect is needed, in order to develop methods to improve this time constraint.

To understand this process, the amount of insoluble (i.e. 'cross-linked') PECA that is formed on the print is monitored by sonicating the print in THF solution after fuming, where the mass of the PECA that remains after sonication is denoted as cross-linked material. Figure 6.11 shows the amount of the fumed print that remains on the slide after sonication in THF as a function of time after fuming. The mass of crosslinked polymer, mass of uncrosslinked polymer, and percent of the polymer that is crosslinked is determined by monitoring the mass of the fumed

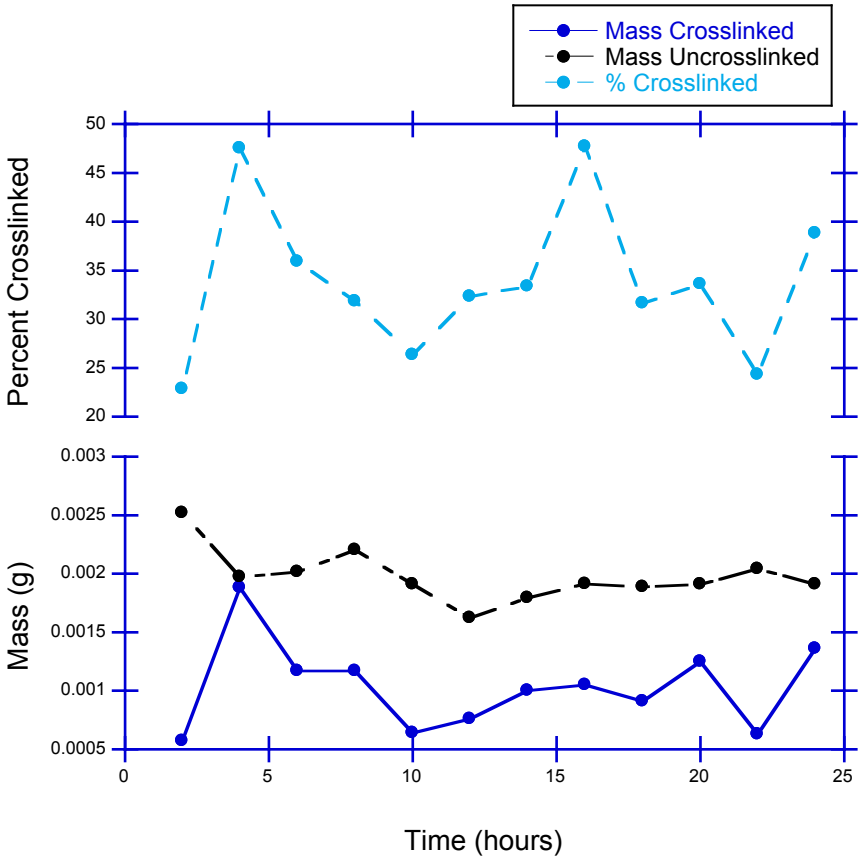

Figure 6.11 Percent and mass of uncrosslinked and crosslinked polymer on the prints as a function of time after fuming.

print after deposition, after fuming, time after fuming, and after THF exposure. This data, therefore, monitors the extent of crosslinking of the polymer as a function of time after fuming. Figure 6.11 indicates that there isn't a significant change in the amount of crosslinked polymer with time after fuming, i.e. as the print is allowed to 'harden'. The amount of uncrosslinked polymer on the print is also fairly constant with increasing time after fuming. This invariability suggests that the hardening process as observed by forensic scientists is not dominated by the cross-linking of the polymer chains, but may be dominated by other processes. More study is therefore needed to understand the chemistry and reactions that occur in the polymerization of ECA fumes by latent fingerprint components to provide sufficient fundamental information to control this phenomenon.

6.8 Understanding the Reactions of Ethyl Cyanoacrylate with FT-IR

In order to develop methods to improve efficiency and optimize the superglue fuming process, a more careful understanding of the molecular level processes that occur during fingerprint fuming and subsequent "hardening" is needed. Fourier Transform Infrared spectroscopy (FT-IR) provides specific information about chemical bonding and molecular structures, making it useful for analyzing organic materials and certain inorganic materials. Chemical bonds vibrate at characteristic frequencies, and when exposed to infrared radiation, they absorb the radiation at frequencies that match their vibration modes. Measuring the radiation absorption as a function of frequency produces a spectrum that can be used to identify the presence or absence of functional groups and compounds.

To understand the reactions that occur in the polymerization of ECA, the polymerization of the monomer ethyl cyanoacrylate (ECA) in the bulk was studied. The IR spectrum of a small amount of neat ECA was collected every two hours for a twenty-four hour time period. Inspection of these spectra show a decrease in intensity of the 3130 cm^{-1} peaks [90], as shown in Figure 6.12, which corresponds to the –C=C- stretching vibrations of the vinyl structures (-CH=CH_2). The C=C bond is of great importance for cyanoacrylate cure because this functionality disappears during the formation of polymer chains from the monomer units.

However, a decrease in the CN peak at 2240 cm^{-1} was not as expected, but is observed as shown in Figure 6.13. As described above, previous results from our groups show that a "hardening" effect experienced by most forensic scientists was not a result of PECA crosslinking. Further investigation is therefore needed to determine the reaction that occurs which decreases the CN peak, if it is not crosslinking.

To further explore the possible mechanism of the polymerization process, the IR spectra of fresh monomer, poly(ethyl cyanoacrylate) that is grown during the fuming of latent prints, and monomer that is cured in the bulk for 5 hours are compared. The latent prints were applied to a gold-coated microscope slide, and then fumed for ten minutes, after which they were analyzed via FT-IR.

Variations in the chemical structures of the three samples can be elucidated by inspecting the three spectra at various wavelengths, as shown in Figures 6.14, 6.15, 6.16, and 6.17. Inspection of Figure 6.14 shows that the peak at 810 cm^{-1} in the

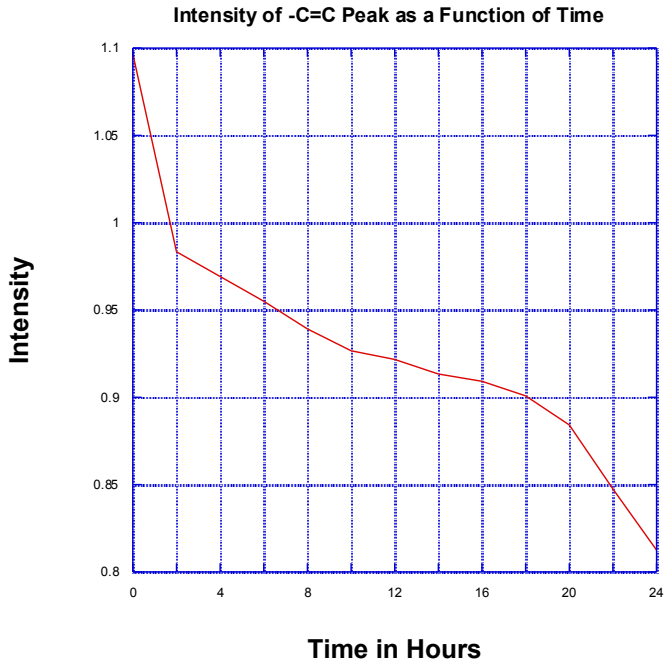

Figure 6.12 Change in the –C=C peaks of cyanoacrylate monomer during curing of the monomer.

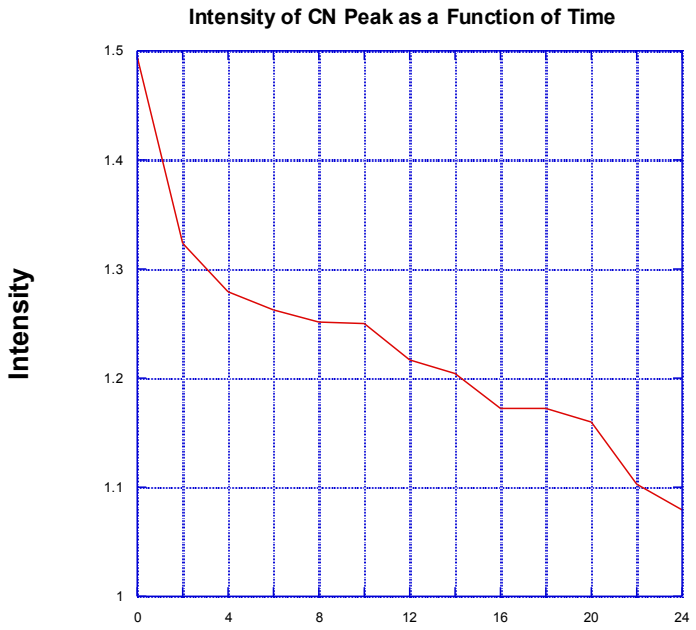

Figure 6.13 Change in -CN FTIR peak intensity as a function of curing time of the monomer.

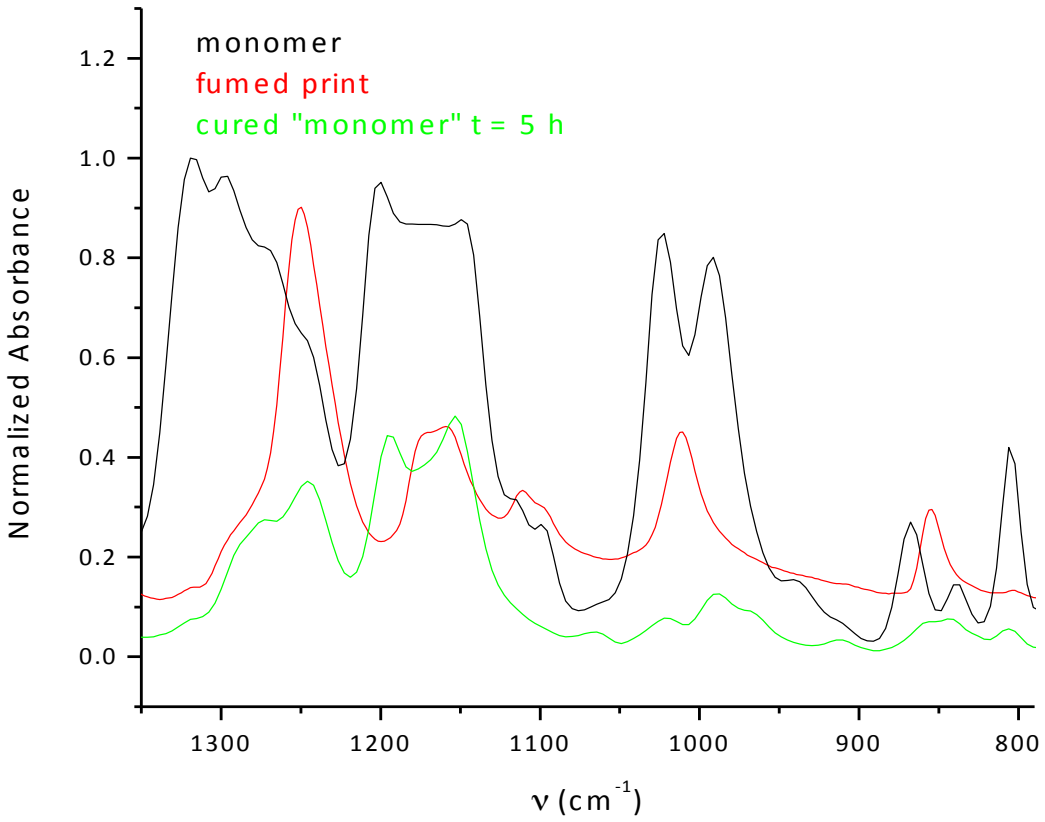

Figure 6.14 FT-IR of monomer, a fumed print, and cured monomer after five hours in the 800-1300 cm^{-1} region.

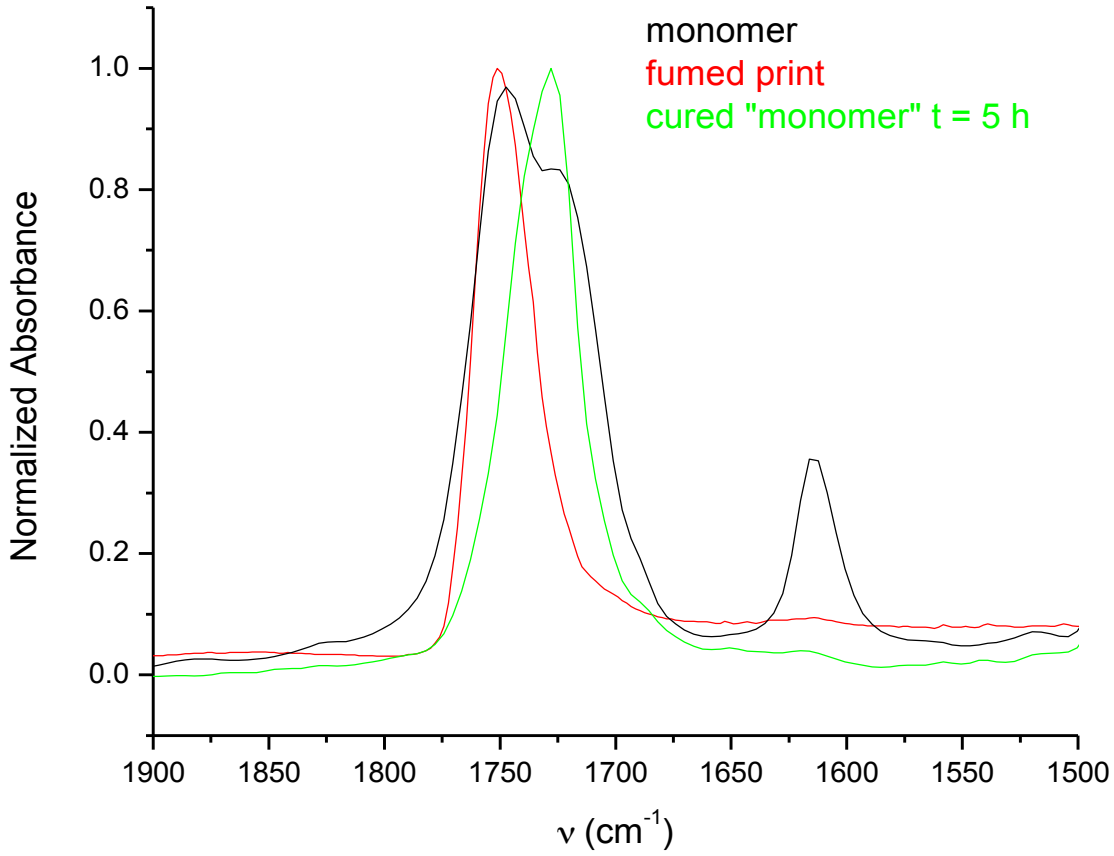

Figure 6.15 FT-IR of monomer, a fumed print, and cured monomer after five hours.

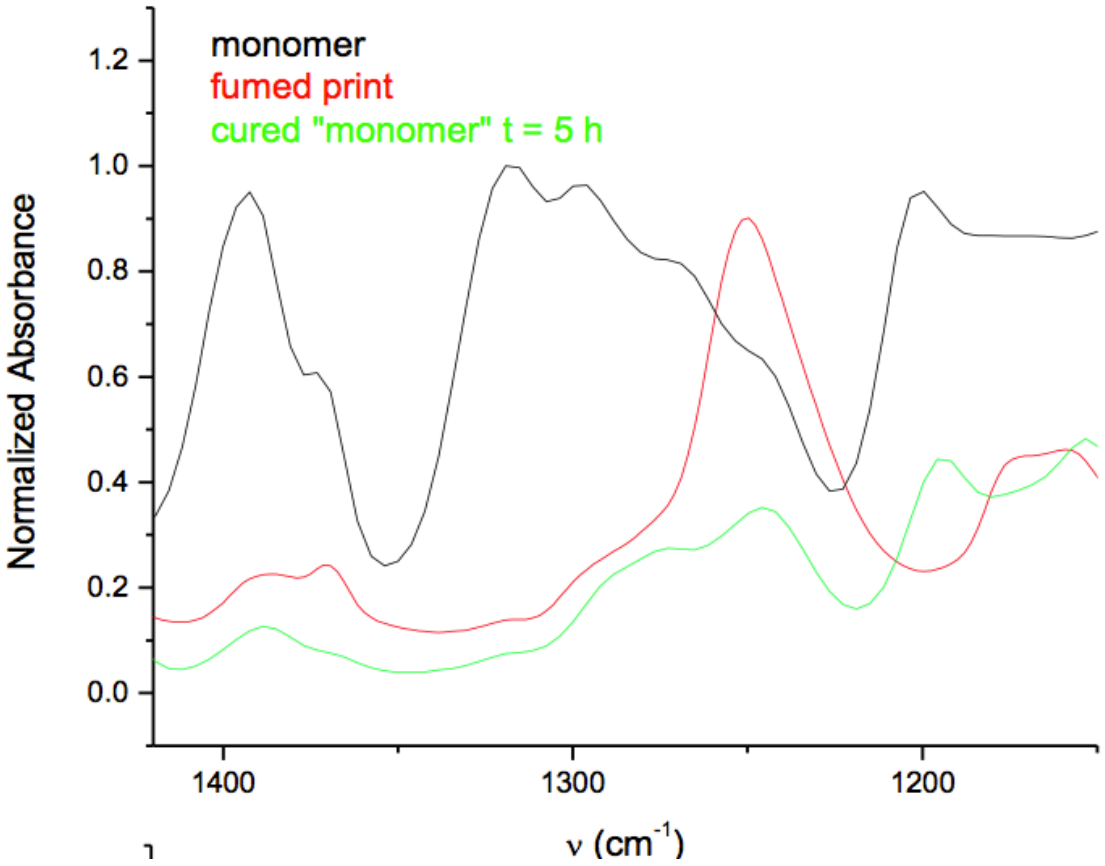

Figure 6.16 FT-IR of monomer, a fumed print, and cured monomer after five hours.

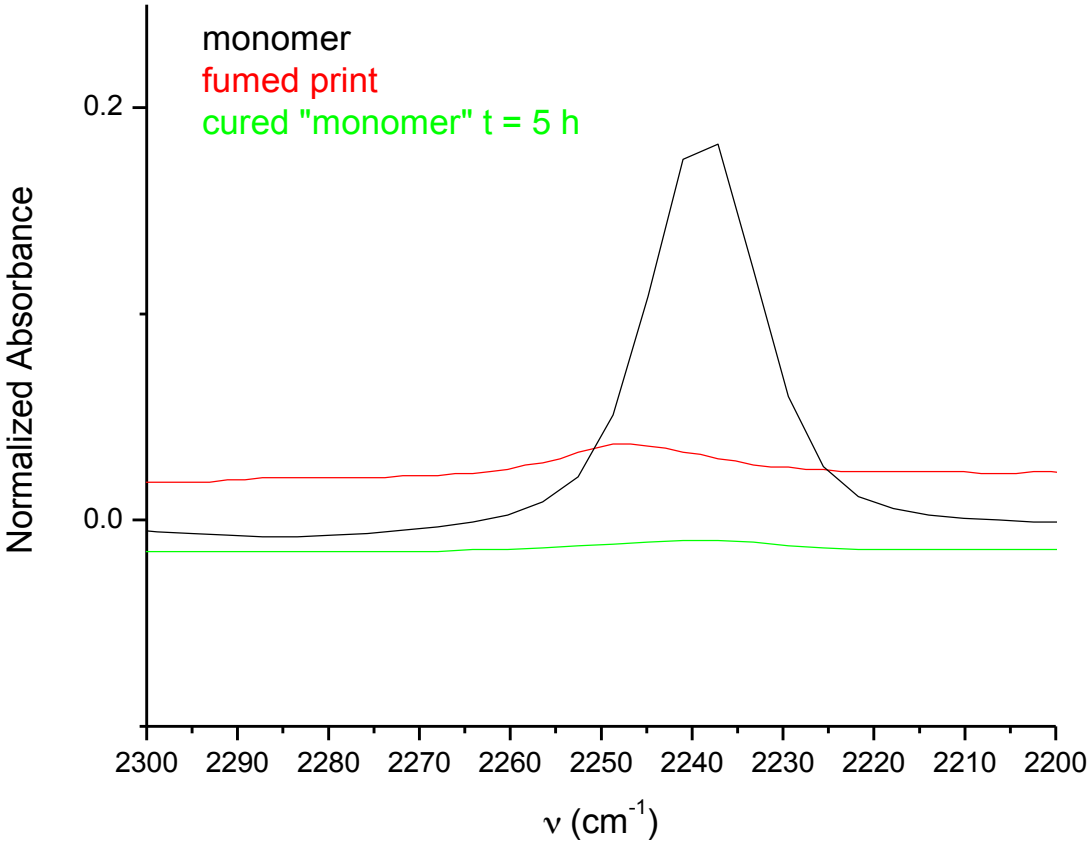

Figure 6.17 FT-IR of monomer, a fumed print, and cured monomer after five hours.

monomer decreases with curing. This peak is related to the deformation mode of the vinyl groups, an out of plain bending vibration of =C-H, which decreases with the C=C bond during polymerization [91]. Peaks at 990 cm^{-1} and 1021 cm^{-1} merge to form one peak at 1015 cm^{-1} in both the cured monomer and fumed print, which signifies a change in ν(CO) terminal group [91] showing that the monomer and fumed print have different (CO) terminal groups. The peak at 1207 cm^{-1} disappears with polymerization, while peaks at 1319 cm^{-1} and 1288 cm^{-1} shift to 1223 cm^{-1}. These peaks are both associated with the C-O stretching vibration. This shift during curing is thought to be due to the changing environment associated with the loss of the adjacent C=C bond [90].

In Figure 6.15, a shift is seen in the peak at 1690-1745 cm^{-1}, which is dependent on the polymerization process. This is the carbonyl peak, which can range from 1690-1770 cm^{-1} depending on whether it is free or hydrogen bonded, where a free carbonyl peak is 1732 -1745cm^{-1} [91]. These IR curves clearly show that the monomer contains both free and hydrogen bonded carbonyls, while the fumed print and the cured monomer appear to be dominated by a single population of the carbonyl. The fumed print appears to be dominated by carbonyls that are free, while the cured PECA is dominated by carbonyls that are hydrogen bonded. This could signify that the cured monomer initiates from moisture in the air, and as the polymer cures some water molecules remain that hydrogen bond to the carbonyls of the acrylate. The fumed print, however, does not have this signature peak, indicating that there is very little water in the PECA that forms from fuming. This is

consistent with the higher temperature of the polymerization during the fuming process, which may limit the presence of water in the final polymer.

These results further indicate that the moisture in the air does not initiate the fumed print, which reconfirms that rehydrating the aged prints with water vapor exposure is not an effective method to revive aged prints. It also appears the monomer contains tertiary C-OH groups, as denoted by the peaks at 1200 cm^{-1} and 1395 cm^{-1} as displayed in Figure 6.16. Interestingly, these peaks, and therefore functional groups, are not present in the fumed prints and seem to correlate to the shift in the C-O peaks at 1745 cm^{-1} that occurs in the monomer and the bulk cured PECA.

The results shown in Figure 6.17 verify that major changes occur in the –CN peak (~2240 cm-1) during polymerization. There is a shift from a peak at 2238 cm^{-1} for the monomer to a peak at 2248 cm^{-1} for both the fumed prints and the cured monomer. The shift in the peak as well as the change in shape is thought to be associated with the loss of conjugation between the CN, C=C, and C=O groups with the presence of the –CN groups in two distinct environments in the system [28]. Another possibility is that after nucleophilic attack (in the initiation step), the –COOR and –CN groups significantly stabilize the anion formed at the α-carbon by delocalizing the negative charge. The shift of the –CN peak could also be a consequence of intra- and intermolecular hydrogen bonding [28,90-92]

Finally, in-situ IR was also used to monitor the change in the IR spectra of the growing poly(ethyl cyanoacrylate) as a function of fuming time on a latent print during the fuming process. In this experiment, a latent print was applied to the tip

of the in-situ IR diamond tipped probe and exposed to monomer vapors as would occur in the standard fuming process. Via this method, the polymerization reaction can be monitored more closely. The result are shown in Figure 6.18, which shows the IR spectrum of the monomer, the IR spectra of the print at various fuming times, and the IR spectra of the final fumed print in the region of the –CN peak. Inspection of this figure shows that–CN peak position and shape varies throughout the polymerization process. While there are many thought processes on the reason for the shift in the –CN peak, the reason for the decrease is not understood. It could be that it is a consequence of the change in the local environment or the result of a specific chemical reaction [90] and will be further evaluated.

The differences in the chemical structure that results when the monomer is polymerized in the bulk relative to that which is formed on a fumed print are interesting and worthy of further study. Similarly, the molecular level explanation for the decrease and shift in the CN peak must be explained. The differences in polymer structure may be the result of the presence of water in the two materials. For instance, water may not be evenly distributed in the bulk monomer, yielding different local environments, intermolecular interactions, and –C=O peaks. Similarly, the PECA in the fumed print grows from surface bound initiators, which form different structures than in the bulk where interactions with H_2O appear to be important. The reactions of the –CN group must also be examined more thoroughly, as this appears to be an important process in understanding the differences in the growth of PECA via fuming and its polymerization in the bulk.

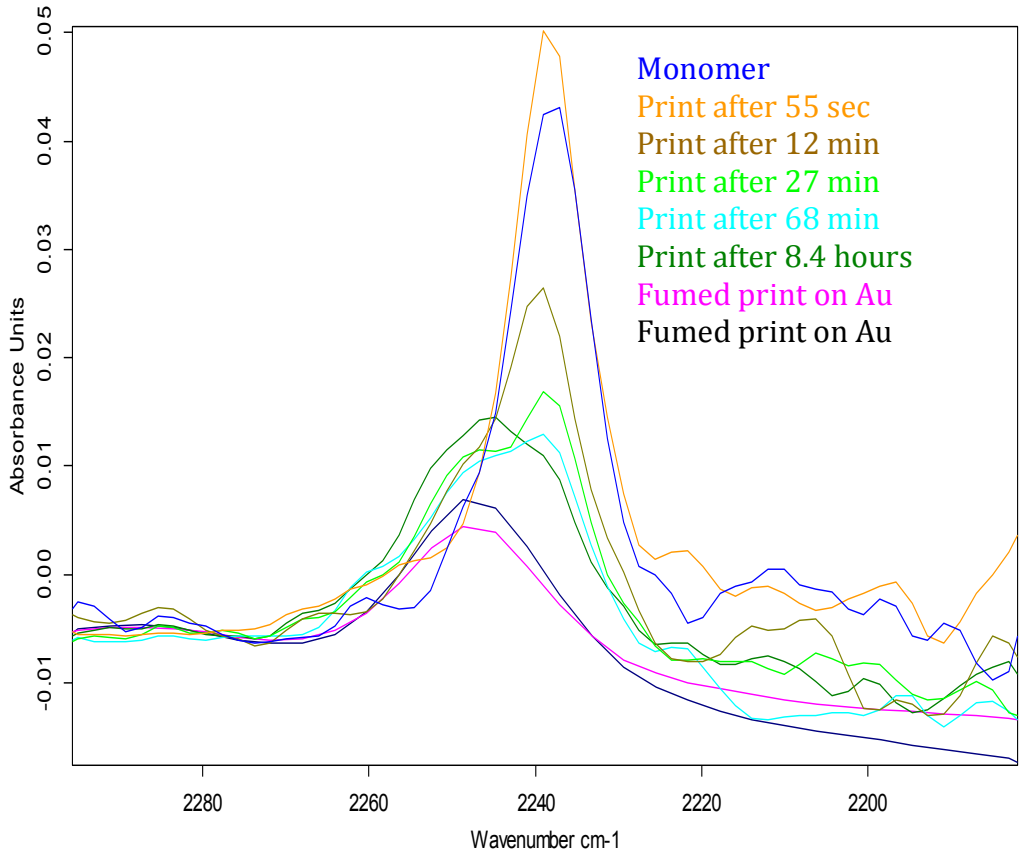

Figure 6.18 FT-IR of monomer, a fumed print on Au slides, and fuming print on diamond tipped probe.

Chapter 7

Conclusions

7.1 Role of P3HT and PCBM Interfacial Interactions on the Morphology of OPV Active Layers

The ordering of P3HT molecules as determined by x-ray diffraction and Raman spectroscopy was correlated to the efficiency of the system to dissociate an exciton by examining photoluminescence of neat P3HT and P3HT/PCBM mixtures. The introduction of PCBM into the system improves exciton dissociation relative to that of the neat polymer. This verifies that the dissociation of an exciton is dominantly controlled by the amount of interface between PCBM and P3HT; and therefore their ability to intermix and create more interfacial area is a crucial parameter that must be accurately characterized and controlled.

Exploration of the mixing behavior of PCBM and P3HT and the impact of the presence of the PCBM on the ordering of the P3HT by Raman Spectroscopy indicates that there exists a third orientation state of the P3HT that behaves as an intermediary between the fully ordered crystalline phase and the disordered amorphous phase. This third conformation state is shown to be correlated to the "aggregated" species that can be monitored by Raman spectroscopy, which is a structure that has a longer, more planar conjugation length than that of the shorter, more twisted amorphous segments. However, structurally, these segments are not quite as ordered and rigid as crystalline domains. Correlating the optical properties of the various states of P3HT from Raman spectroscopy to the structural characterization of the P3HT ordering by GIXRD, a qualitative term was developed

that estimates the surface area that exists between the crystalline and amorphous P3HT, which monitors the amount of neighboring P3HT segments that exist between the crystalline and amorphous domains.

Further investigations of miscible mixed thin films of PCBM/P3HT, indicate that PCBM can act as a plasticizer of P3HT, which results in a decrease in the overall P3HT crystallinity and an increase in the crystal size with thermal annealing, indicating that the PCBM can erode smaller P3HT crystalline domains. However, PCBM does not behave as a plasticizer in the samples that are processed as 'bilayers', where the P3HT and PCBM are deposited from orthogonal solvents. Moreover, this 'bilayer' fabrication procedure allows control of the P3HT ordering in the thin films prior to PCBM deposition. In these bilayers, PCBM appears able to nucleate the growth of small P3HT crystalline domains during deposition, and with further annealing the PCBM doesn't disrupt the P3HT structures created prior to the introduction of the PCBM. In fact, PCBM seemed to interact mostly with the amorphous P3HT domains leaving the robust crystalline domains intact.

Lastly for the P3HT/PCBM systems, neutron reflectivity and NEXAFS monitored the intermixing of P3HT and PCBM bilayers. These results show that annealing the as-cast 'bilayers' forms broader, rougher interfaces indicative of the intermixing of PCBM and P3HT. The concentration depth profiles show an even distribution of PCBM throughout the entire thin film after deposition. All of the as-cast samples show an excess of PCBM at the substrate interface, which begins to redistribute throughout the bulk of the film with thermal annealing. However, with increased crystallization of the P3HT prior to PCBM deposition, less of the PCBM is

able to migrate to the substrate during deposition due to the crystalline domains blocking the pathways of PCBM to the interface.

The NEXAFS work confirmed some of the conclusions achieved from the neutron reflectivity data. The concentration of PCBM at the air interface increases with increased P3HT crystallization. This coordinates well with the NR results, which shows that increasing P3HT crystallization prevents the migration of PCBM through the bulk and to the substrate interface, which would result in more of the PCBM residing at the air surface. Lastly, monitoring the dichroic ratio indicates that there is a modest change in orientation of the P3HT crystals at the surface with annealing. This minimal variation verifies that the changes that are observed in the crystalline peak area in GIXRD can be ascribed to changes in P3HT crystallinity and not orientation of the crystals.

7.2 Polymerization of Ethyl-Cyanoacrylate to Improve Fumed Latent Prints

Progress in understanding and developing methods to improve the quality of fumed latent prints are reported. Since aging prints lose water and the availability of initiators that are present in the print to polymerize cyanoacrylate, rehydration of the aged latent prints via exposure to water vapor prior to cyanoacrylate fuming was attempted. However, exposure of the print to the vapor of room temperature or boiling water had little or a negative effect on the ability of the print to polymerize ethyl cyanoacrylate. In fact, the boiling water vapor appeared to decrease the mass of the print, washing it away. The prints that are exposed to water vapors decreases the print ridge distinction, therefore yielding poorer quality prints.

Controlling the temperature at which the fuming, and thus ECA polymerization, occurs was examined as a method to improve the quality of fumed prints. With a decrease in fuming temperature, the ion pair at the end of the growing polymer chain loosens, improving the rate of initiation and propagation resulting in the growth of more PECA on the latent prints. As the fuming temperature is lowered further, an optimum fuming temperature ~10 °C was identified. This optimum is ascribed to a balance of the increased propagation rate due to the looser ion pair and the decreased reaction rate between the chain end and approaching monomer that results from the slower collision velocities at lower temperatures.

Even with the improvement of the polymerization of ethyl cyanoacrylate during the fuming of latent prints by decreasing the fuming temperature, forensic scientists still have to wait 24 hours for a "hardening" process to occur to prevent smearing of the prints. Exploration of this "hardening" process as a product of crosslinking of the PECA with time indicates that crosslinking is not the cause of this hardening. Further studies investigated possible mechanisms that might be responsible for this "hardening" process, including monitoring the reaction with FT-IR. These preliminary studies indicate that the reactions that occur in the curing of ethyl cyanoacrylate in the bulk differs from those that occur in the growth of PECA during fuming, and that further studies are needed to more accurately define the reactions that differentiate these two polymerizations.

References

1 Swanson, R. A Vision for Crystalline Silicon Photovoltaics. *Prog. Photovolt: Res. Appl* **14** (2006).
2 Composto, R. J. & Oslanec, R. in *Polymer Surfaces, Interfaces and Thin Films* 181-228.
3 Green, M. Third Generation Photovoltaics: Ultra-high Conversion Efficiency at Low Cost. *Prog. Photovolt: Res. Appl* **9**, 123 (2001).
4 Karim, A. & Kumar, S. Vol. vii (World Scientific Pub Co Inc, 2000).
5 Baschnagel, J., Binder, K. & Milchev, A. in *Polymer Surfaces, Interfaces and Thin Films* 1-33 (2000).
6 Koberstein, J. T. in *Polymer Surfaces, Interfaces and Thin Films* 115-180 (2000).
7 Ratner, B., Yoon, S. & Mateo, N. in *Polymer Surfaces and Interfaces* 231-251 (1987).
8 Eastmond, G. C. in *Polymer Surfaces and Interfaces* 119-136 (1987).
9 Gibson, E. & Hagfeldt, A. in *Energy Materials* Ch. 95-243, 95-243 (John Wiley & Sons, Ltd, 2011).
10 Uthirakumar, A. P. in *Solar Cells - Dye-Sensitized Devies* (ed L. Kosyachenko) 435-456 (InTech, 2011).
11 Armand, M., Bruce, P., Forsyth, M. & Scrosati, B. in *Energy Materials* 1-31 (John Wiley & Sons, Ltd, 2011).
12 Li, G., Zhu, R. & Yang, Y. Polymer solar cells. *Nature Photonics* **6**, 153-161, doi:10.1038/nphoton.2012.11 (2012).
13 Salaneck, W. R., Stafström, S. & Brédas, J. L. Conjugated Polymer Surfaces and Interfaces *Molecular Crystals and Liquid Crystals Science and Technology. Section A. Molecular Crystals and Liquid Crystals* **308**, 157, doi:10.1080/10587259708045103 (1996).
14 Chidichimo, G. & Filippelli, L. Organic Solar Cells: Problems and Perspectives. *International Journal of Photoenergy* **2010**, 1-11, doi:10.1155/2010/123534 (2010).
15 Akamatsu, H., Inokuchi, H. & Matsunaga, Y. Electrical Conductivity of the Perylene-Bromine Complex. *Nature* **173** (1954).
16 Shirakawa, H., McDiarmid, A. & Heeger, A. Focus Article: Twenty-five years of conducting polymers. *Chemical Communications*, doi:10.1039/b210718j (2003).
17 Deibel, C. & Dyakonov, V. Polymer-Fullerene Bulk Heterojunction Solar Cells. *Rep. Prog. Phys.* **73**, 68 (2010).
18 Chidichimo, G. & Filippelli, L. Organic Solar Cells: Problems and Perspectives. *International Journal of Photoenergy* **2010**, doi:10.1155/2010/123534 (2010).
19 Thompson, B. C. & Frechet, J. M. Polymer-Fullerene Composite Solar Cells. *Angewandte Chemie International Edition* **47**, 58-77 (2008).
20 Spano, F. C. Absorption in Regio-regular Poly(3-hexyl) Thiophene Thin Films: Femi Resonances, interband coupling and disorder. *Chemical Physics* **325**, 22-35, doi:10.1016/j.chemphys.2005.08.019 (2006).
21 Salamandra, L. *Organic Photo-Voltaic Cells and Photo-Dectors based on Polymer Bulk-Heterojunctions* Ph.D. thesis, University of Rome, (2009).

22 Huang, W. Y., Lee, C. C. & Hsieh, T. L. The role of conformational transitions on the performance of poly(3-hexylthiophene)/fullerene solar cells. *Solar Energy Materials and Solar Cells* **93**, 382-386, doi:10.1016/j.solmat.2008.11.016 (2009).
23 Osterbacka, R., An, C. P., Jiang, X. M. & Vardeny, Z. V. Two-Dimensional Electronic Excitations in Self-Assembled Conjugated Polymer Nanocrystals. *Science* **287**, 839-842, doi:10.1126/science.287.5454.839 (2000).
24 Pearson, A. The Role of Dynamic Measurements in Correlating Structure with Optoelectronic Properties in Polymer:Fullerene Bulk-Heterojunctions. *Reports on Progress in Physics* **76** (2013).
25 Falke, S., Eravuchira, P., Materny, A. & Lienau, C. Raman Spectroscopic Identification of Fullerene Inclusions in Polymer/Fullerene Blends. *J. Raman Spectrosc.* (2011).
26 Gao, Y., Martin, T. & Grey, J. K. Understanding Morphology Dependent Polymer Aggregation Properties and Photocurrent Generation in Poly(Thiophene/Fullerene) Solar Cells of Variable Compositions. *J. Phys. Chem.* **2010** (2010).
27 Daeid, N. 16th International Forensic Science Symposium Interpol. 222-319 (Forensic Science Service, IFSS, 2010).
28 Edwards, H. & Day, J. S. Anomalies in Polycyanoacrylate Formation Studied by Raman Spectroscopy: Implications for the Forensic Enhancement of Latent Fingerprints for Spectral Analysis. *Vibrational Spectroscopy* (2006).
29 Wallman, J., Roux, C. & Lennard, C. *Forensic Science, Medicine, and Pathology*. Vol. 7 (Springer, 2011).
30 Bleay, S. M. *et al.* (ed Steeve Barber) 500 (Home Office, http://www.gov.uk, 2012).
31 Jones, N., Mansour, D. & Roux, C. The Influence of Polymer Type, Print Donor, and Age on the Quality of Fingerprints Developed on Plastic Substrates Using Vacuum Metal Deposition. *Forensic Science International*, 167 (2001).
32 Jones, N., Stoilovic, M., Lennard, C. & Roux, C. Vacuum metal deposition: factors affecting normal and reverse development of latent fingerprints on polyethylene substrates. *Forensic science international* **115**, 73-88, doi:10.1016/S0379-0738(00)00310-8 (2001).
33 Jones, N., Stoilovic, M. & Roux, C. Vacuum Metal Deposition; Developing Latent Fingerprints on Polyethylene Substrates After the Deposition of Excess Gold. *Forensic Science International* (2001).
34 Sodhi, G. S. & Kaur, J. *Methods For Fixing Constituents of Human Sweat For Developing Latent Fingerprints*, <http://www.bhj.org.in/journal/2000_4201_jan00/original_119.htm> (2000).
35 Lennard, C. *The Detection and Enhancement of Latent Fingerprints*, <http://latent-prints.com/images/SpecialPresentation.pdf> (2001).
36 Sodhi, G. S. & Kaur, J. Power Method for Detecting Latent Fingerprints; A Review. *Forensic Science International* (2001).

37 Migron, Y., Hocherman, G. & Mandler, D. Visualization of Sebaceous Fingerprints on Fired Cartridge Cases: A Laboratory Study. *Journal of Forensic Science* (1997).
38 Yamashita, B. & French, M. Latent Print Development.
39 Grubwieser, P., Thaler, A. & Parson, W. Systematic Study of STR Profiling on Blood and Saliva Traces After Visualization of Fingerprint Masks. *Journal of Forensic Science*, 733-741 (2003).
40 von Wurmb, N., Meissner, D. & Wegener, R. Influence of cyanoacrylate on the efficiency of forensic PCRs. *Forensic science international* **124**, 11-16 (2001).
41 Balogh, M. K., Burger, J. & Alt, K. W. STR Genotyping and mtDNA sequencing of Latent Fingerprints on Paper. *Forensic Science International* (2003).
42 Wargacki, S. P., Lewis, L. A. & Dadmun, M. D. Enhancing the Quality of Aged Latent Fingerprints Developed by Superglue Fuming: Loss and Replenishment of Initiator. *Journal of Forensic Science* (2008).
43 Day, J., Edwards, H., Dobrowski, S. & Voice, A. The detection of drugs of abuse in fingerprints using Raman spectroscopy I: latent fingerprints. *Spectrochimica acta. Part A, Molecular and biomolecular spectroscopy* **60**, 563-568 (2004).
44 Kong, H. & Segre, J. Skin microbiome: looking back to move forward. *The Journal of investigative dermatology* **132**, 933-939, doi:10.1038/jid.2011.417 (2012).
45 Wargacki, S., Lewis, L. & Dadmun, M. D. Understanding the chemistry of the development of latent fingerprints by superglue fuming. *Journal of forensic sciences* **52**, 1057-1062, doi:10.1111/j.1556-4029.2007.00527.x (2007).
46 Algaier, D., Baskaran, D. & Dadmun, M. D. The Influence of Temperature on the Polymerization of Ethyl Cyanoacrylate From the Vapor Phase. *Reactive & Functional Polymers* (2011).
47 Ayzner, A. L., Tassone, C. J., Tolbert, S. H. & Schwartz, B. J. Reappraising the Need for Bulk Heterojunctions in Polymer–Fullerene Photovoltaics: The Role of Carrier Transport in All-Solution-Processed P3HT/PCBM Bilayer Solar Cells. *The Journal of Physical Chemistry C* **113**, doi:10.1021/jp9050897 (2009).
48 Mao‐Yuan, C., U‐Ser, J., Chiu‐Hun, S., Keng, S. L. & Kung‐Hwa, W. Simultaneous Use of Small‐ and Wide‐Angle X‐ray Techniques to Analyze Nanometerscale Phase Separation in Polymer Heterojunction Solar Cells. *Advanced Materials* **20**, doi:10.1002/adma.200703097 (2008).
49 Erb, T. *et al.* Correlation Between Structural and Optical Properties of Composite Polymer/Fullerene Films for Organic Solar Cells. *Advanced Functional Materials* **15**, doi:10.1002/adfm.200400521 (2005).
50 Treat, N. D. *et al.* Correction: Interdiffusion of PCBM and P3HT Reveals Miscibility in a Photovoltaically Active Blend. *Advanced Energy Materials* **1**, doi:10.1002/aenm.201190008 (2011).
51 Chen, H., Hegde, R., Browning, J. & Dadmun, M. D. The miscibility and depth profile of PCBM in P3HT: thermodynamic information to improve organic

photovoltaics. *Physical chemistry chemical physics : PCCP* **14**, 5635-5641, doi:10.1039/c2cp40466d (2012).
52 Lee, K. *et al.* Morphology of all-solution-processed "bilayer" organic solar cells. *Advanced materials (Deerfield Beach, Fla.)* **23**, 766-770, doi:10.1002/adma.201003545 (2011).
53 Minze, T. R. *et al.* Influence of the solvent on the crystal structure of PCBMPCBM: Phenyl-C61-Butyric acid Methyl ester. IUPAC: methyl 5-(3?H-cyclopropa[1,9](C60-Ih)[5,6]fullerenyl)-5-phenylpentanoate. and the efficiency of MDMO-PPV:PCBM ?plastic? solar cells. *Chemical Communications*, doi:10.1039/b305988j (2003).
54 Munter, A. (NIST, NIST Center for Neutron Research, 2012).
55 Chen, H., Hegde, R., Browning, J. & Dadmun, M. D. The miscibility and depth profile of PCBM in P3HT: thermodynamic information to improve organic photovoltaics. *Physical chemistry chemical physics : PCCP* **14**, 5635-5641, doi:10.1039/C2CP40466D (2012).
56 Wargacki, S. P., Lewis, L. A. & Dadmun, M. D. Understanding the chemistry of the development of latent fingerprints by superglue fuming. *J Forensic Sci* **52**, 1057-1062, doi:10.1111/j.1556-4029.2007.00527.x (2007).
57 Gao, Y. & Grey, J. Resonance chemical imaging of polythiophene/fullerene photovoltaic thin films: mapping morphology-dependent aggregated and unaggregated C=C Species. *Journal of the American Chemical Society* **131**, 9654-9662, doi:10.1021/ja900636z (2009).
58 Tsoi, W. C. *et al.* Effect of Crystallization on the Electronic Energy Levels and Thin Film Morphology of P3HT:PCBM Blends. *Macromolecules* **44**, doi:10.1021/ma102841e (2011).
59 Korovyanko, O., Österbacka, R., Jiang, X., Vardeny, Z. & Janssen, R. Photoexcitation dynamics in regioregular and regiorandom polythiophene films. *Physical Review B* **64**, doi:10.1103/PhysRevB.64.235122 (2001).
60 Tsoi, W. *et al.* The nature of in-plane skeleton Raman modes of P3HT and their correlation to the degree of molecular order in P3HT:PCBM blend thin films. *Journal of the American Chemical Society* **133**, 9834-9843, doi:10.1021/ja2013104 (2011).
61 Jo, S. B., Lee, W. H., Qiu, L. & Cho, K. Polymer blends with semiconducting nanowires for organic electronics. *Journal of Materials Chemistry* **22**, doi:10.1039/c2jm16059e (2012).
62 Kim, Y. *et al.* A strong regioregularity effect in self-organizing conjugated polymer films and high-efficiency polythiophene:fullerene solar cells. *Nature Materials* **5**, 197-203, doi:10.1038/nmat1574 (2006).
63 Ma, W., Yang, C., Gong, X., Lee, K. & Heeger, A. J. Thermally Stable, Efficient Polymer Solar Cells with Nanoscale Control of the Interpenetrating Network Morphology. *Advanced Functional Materials* **15**, doi:10.1002/adfm.200500211 (2005).
64 Collins, B., A. , Tumbleston, J. R. & Ade, H. Miscibility, Crystallinity, and Phase Development in P3HT/PCBM Solar Cells: Toward an Enlightened Understanding of Device Morphology and Stability. *The Journal of Physical Chemistry Letters* **2**, doi:10.1021/jz2014902 (2011).

65 Moulé, A. J. & Meerholz, K. Controlling Morphology in Polymer–Fullerene Mixtures. *Advanced Materials* **20**, doi:10.1002/adma.200701519 (2008).
66 Sudip, M. & Arun, K. N. Crystallization mechanism of regioregular poly(3-alkyl thiophene)s. *Journal of Polymer Science Part B: Polymer Physics* **40**, doi:10.1002/polb.10272 (2002).
67 Mariano, C.-Q., Yoshihiro, K., Ahmed, E.-B., Heisuke, S. & Hideyuki, M. Ternary mixing: A simple method to tailor the morphology of organic solar cells. *Organic Electronics* **10**, doi:10.1016/j.orgel.2009.05.028 (2009).
68 Youngkyoo, K. *et al.* A strong regioregularity effect in self-organizing conjugated polymer films and high-efficiency polythiophene:fullerene solar cells. *Nature Materials* **5**, doi:10.1038/nmat1574 (2006).
69 Samuele, L. *et al.* Dynamics of Crystallization and Disorder during Annealing of P3HT/PCBM Bulk Heterojunctions. *Macromolecules* **44**, doi:10.1021/ma102817z (2011).
70 Wunderlich, B. & Wiedemann, H. Condis Crystals of Small Molecules I. The Concept and Limitations. *Molecular Crystals and Liquid Crystals* **140** (1986).
71 Yin, W. & Dadmun, M. D. A new model for the morphology of P3HT/PCBM organic photovoltaics from small-angle neutron scattering: rivers and streams. *ACS nano* **5**, 4756-4768, doi:10.1021/nn200744q (2011).
72 Pradhan, D., Choudhary, R., B, S., Karan, N. & Katiyar, R. Effect of Plasticizer on Structural and Electrical Properties of Polymer Nanocomposite Electrolytes. *International Journal of Electrochemical Science* **2**, 861-871 (2007).
73 Parnell, A. *et al.* Depletion of PCBM at the cathode interface in P3HT/PCBM thin films as quantified via neutron reflectivity measurements. *Advanced materials (Deerfield Beach, Fla.)* **22**, 2444-2447, doi:10.1002/adma.200903971 (2010).
74 Salleo, A. Charge transport in polymeric transistors. *Materials Today* **10**, doi:10.1016/S1369-7021(07)70018-4 (2007).
75 Treat, N. D., Mates, T. E., Hawker, C. J., Kramer, E. J. & Chabinyc, M. L. Temperature Dependence of the Diffusion Coefficient of PCBM in Poly(3-hexylthiophene). *Macromolecules* **46**, doi:10.1021/ma302337p (2013).
76 Lu, H., Akgun, B. & Russell, T. P. Morphological Characterization of a Low-Bandgap Crystalline Polymer:PCBM Bulk Heterojunction Solar Cells. *Advanced Energy Materials* **1**, doi:10.1002/aenm.201100128 (2011).
77 Moram, M. A. & Vickers, M. E. X-ray diffraction of III-nitrides. *Reports on Progress in Physics* **72**, 036502, doi:10.1088/0034-4885/72/3/036502 (2009).
78 Padmanabhan, V., Frischknecht, A. L. & Mackay, M. E. Effect of Chain Stiffness on Nanoparticle Segregation in Polymer/Nanoparticle Blends Near a Substrate. *Macromolecular Theory and Simulations* **21**, doi:10.1002/mats.201100048 (2012).
79 Russell, T. P. X-ray and Neutron Reflectivity for the Investigation of Polymers. *Materials Science Reports* **5** (1990).
80 Chen, D., Nakahara, A., Wei, D., Nordlund, D. & Russell, T. P3HT/PCBM bulk heterojunction organic photovoltaics: correlating efficiency and morphology. *Nano letters* **11**, 561-567, doi:10.1021/nl103482n (2011).

81 Das, C., Tallarida, M. & Schmeiber, D. Linear dichroism in ALD layers of TiO2. *Environmental Earth Sciences*, doi:10.1007/s12665-013-2836-7 (2013).
82 Stöhr & Outka. Determination of molecular orientations on surfaces from the angular dependence of near-edge x-ray-absorption fine-structure spectra. *Physical review. B, Condensed matter* **36**, 7891-7905 (1987).
83 Hahner, G. Near edge X-ray absorption fine structure spectroscopy as a tool to probe electronic and structural properties of thin organic films and liquids. *Chemical Society reviews* **35**, 1244-1255, doi:10.1039/b509853j (2006).
84 Collins, B., A. *et al.* Molecular Miscibility of Polymer−Fullerene Blends. *The Journal of Physical Chemistry Letters* **1**, doi:10.1021/jz101276h (2010).
85 Park, J. *et al.* Structural Characterization of Conjugated Polyelectrolyte Electron Transport Layers by NEXAFS Spectroscopy. *Advanced Materials* **20**, doi:10.1002/adma.200702995 (2008).
86 DeLongchamp, D. M. *et al.* Variations in Semiconducting Polymer Microstructure and Hole Mobility with Spin-Coating Speed. *Chemistry of Materials* **17**, doi:10.1021/cm0513637 (2005).
87 Day, J. S., Edwards, H. G. M., Dobrowski, S. A. & Voice, A. M. The detection of drugs of abuse in fingerprints using Raman spectroscopy I: latent fingerprints. *Spectrochimica Acta Part A: Molecular and Biomolecular Spectroscopy* **60**, 563-568, doi:10.1016/s1386-1425(03)00263-4 (2004).
88 Eisenberg, A. Clustering of Ions in Organic Polymers. A Theoretical Approach. *Macromolecules* **3**, doi:10.1021/ma60014a006 (1970).
89 Hogen- Esch, T. E. & Smid, J. Studies of Contact and Solvent-Separated Ion Pairs of Carbanions. I. Effect of Temperature, Counterion, and Solvent. *Journal of the American Chemical Society* **88**, doi:10.1021/ja00954a024 (1966).
90 Tomlinson, S. K., Ghita, O. R., Hooper, R. M. & Evans, K. E. The use of near-infrared spectroscopy for the cure monitoring of an ethyl cyanoacrylate adhesive. *Vibrational Spectroscopy* **40**, doi:10.1016/j.vibspec.2005.07.009 (2006).
91 Edwards, H., G. M. & Day, J. S. Fourier transform Raman spectroscopic studies of the curing of cyanoacrylate glue. *Journal of Raman Spectroscopy* **35**, doi:10.1002/jrs.1184 (2004).
92 Tahtouh, M., Kalman, J. R., Roux, C. & Lennard, C. The Detection and Enhancement of Latent Finermarks Using Infrared Chemical Imaging. *Journal of Forensic Science* **50**, 1-9 (2005).

Appendix 1

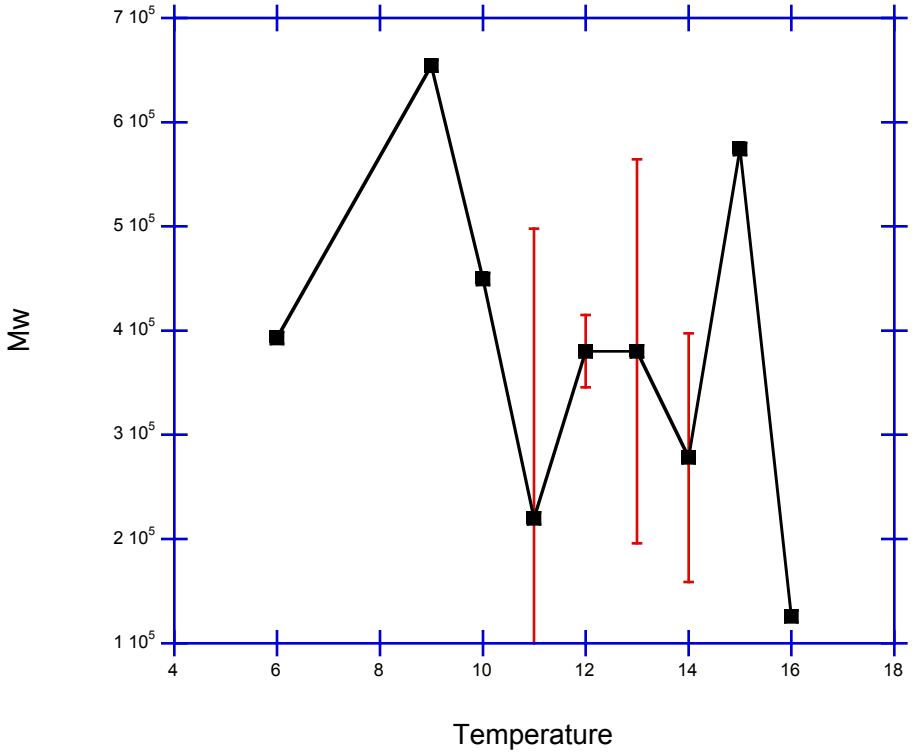

Appendix 1. Plot of the Molecular weight of PECA that is formed on fumed fingerprints as a function of fuming temperature.

Vita

Lesley Danielle Thompson was born in Greenville, Mississippi. After completing high school at Drew Central High School in Monticello, Arkansas in 2002, Lesley went to Baylor University in Waco, Texas. She received a Bachelor of Science degree with a major in Biology and a minor in Chemistry in 2006. She then moved to Knoxville, Tennessee to attend graduate school at the University of Tennessee for Chemistry. There she was employed as a Research Assistant until receiving her Ph.D. in Polymer Chemistry.